Structural investigation of the impact of magnetostriction on GaMnAs thin film lattices and the thermal expansion of (In,Ga)As/GaAs quantum dots

Dissertation
zur Erlangung des Doktorgrades der
Naturwissenschaften

vorgelegt von
Holger Göhring
geboren in Castrop-Rauxel

Lehrstuhl für Experimentelle Physik I
Fakultät Physik
Technische Universität Dortmund
Mai 2017

1. Gutachter : Prof. Dr. Metin Tolan

2. Gutachter : Prof. Dr. Manfred Bayer

Contents

List of Figures

Chapter 1

Introduction

The tailoring of semiconductors in order to enhance various properties has been done in several fields. For example, the injection of confined charge carriers, so called quantum dots, enables a wide range of applications such as quantum dot lasers, photonic devices for the 1.3 μm telecommunication band, or spin-based qubits for quantum information processing.
Another alteration is the doping of non-magnetic semiconductors with magnetic atoms leading to so called diluted magnetic semiconductors. The combination of semiconductor based materials with magnetic properties could revolutionize the field of spintronics utilizing not only the charge of carriers but also their spins for the storage of data. The approach of increasing the efficiency of integrated electrical circuits by the miniaturization of microprocessors will most likely reach a dead end in the future, since the structures like field-effect transistors or magnetic storage devices already posses layer thicknesses of only a few nanometer. Here, the advantages of possible spin transistors may lead the way. First, they could be operated without the application of an electric current, which is more efficient. Additionally, spin transistors could reduce the necessary components of circuits. In a nutshell, spin transistors could lead to devices, which can store more data in less space, are more efficient and probably cheaper compared to conventional electronic devices.
In order to realize such spin transistors, contact materials that are ferromagnetic at room temperature are needed. A promising candidate is the diluted magnetic semiconductor GaMnAs, which has been extensively studied over the years. GaMnAs is grown epitaxially on GaAs substrates with manganese content of a few percent. Starting at around 60 K, Curie temperatures of up to 250 K have been realized in special hybrid systems. Here, the continuous rise of the Curie temperature can be correlated with changes of the sample structure and composition. Although, the hole-mediated ferromagnetism has been studied extensively by a whole range of optical spectroscopy techniques, detailed knowledge about the interrelation to the structural properties is still scarce for these systems.
This work focuses on the investigation of structural changes in GaMnAs thin films in order to determine changes in the crystal lattice during the phase transition from a

paramagnetic state to a ferromagnetic one. The first step towards overcoming this lack of knowledge was the development and construction of an experimental setup sensitive to the small changes of the crystal lattice in the sub-angstrom regime. The requirements of such a setup are a mechanically stable sample position, a highly reproducible sample alignment, and well-defined sample temperature. In a second step thin GaMnAs layers were investigated by the means of x-ray diffraction since, it is a powerful, well-established tool for the investigation of the structure of a wide range of materials on an atomic scale. In another step, the effect of heating on the lattice structure of self-assembled (In,Ga)As/GaAs quantum dots was investigated utilizing the experimental x-ray diffraction setup developed within this thesis. This was done to preclude the thermal heating as the origin of the observed tetragonal lattice distortion in [Tiemeyer12].
The outline of this work is as follows. Chapter 2 introduces the x-ray diffraction technique starting with the basic principles and concluding with the concept of crystal truncation rods that occur for cleaved crystals.
An overview of the diluted magnetic semiconductor GaMnAs is given in chapter 3. Here, the growth process and resulting crystal structure, the hole mediated ferromagnetism and other properties are addressed.
The development of an x-ray diffraction setup is presented in chapter 4. Different experimental approaches are discussed leading to a continuous-flow cryostat setup, which ensures a stable, reproducible investigation in a temperature range of $80\,\mathrm{K}-500\,\mathrm{K}$.
The conducted x-ray diffraction experiments on the impact of spontaneous and induced magnetostriction in GaMnAs thin films are discussed in chapter 5.
Chapter 6 presents the investigation of the thermal expansion of (In,Ga)As/GaAs quantum dots and GaAs, which was also done with the developed x-ray diffraction setup. These measurements confirmed the tetragonal lattice distortion of optically active quantum dots induced by polarons found by Tiemeyer et al. [Tiemeyer12].
The results of this work are summarized in chapter 7. Finally, an outlook to improvements and possible experiments in the future is given.

Chapter 2

The x-ray diffraction technique

Diluted magnetic semiconductors have been under investigation for more than 20 years. Optical spectroscopy is the technique of choice to characterize the optical and magnetic properties of such samples. In order to receive information about structural changes due to magnetostriction x-ray diffraction is the most promising option. With a wavelength in the angstrom regime x-rays yield a sufficient resolution to investigate relative changes on the crystal lattice constant of an order of magnitude of 10^{-4} to 10^{-5}. Since the first determination of the structure of crystalline materials [Bragg13, Debye16], x-ray diffraction became a well-established tool for the structural investigation of a wide range of materials, including semiconductors. For example, the investigation of the strain and lattice mismatch in epitaxial systems is routinely done by x-ray diffraction [Bowen98]. This chapter outlines the theoretical background of the x-ray diffraction method, which can be found in the literature, see e.g. [Pietsch04] or [Falta10]. At first the scattering process for an ideal crystal is discussed. Then, with respect to the investigated structures within this thesis, the concept of diffraction at cleaved crystals is elaborated leading to the introduction of crystal truncation rods.

2.1 Basic principles of x-ray diffraction

In analogy to the scattering of visible light at an optical grating x-ray diffraction (XRD) describes interference phenomena of scattered x-rays at the crystal lattice serving as a grating on an atomic length scale due to its periodic structure. The occurring diffraction patterns reveal information on the crystal lattice structure and interatomic distances. In order to calculate the scattering intensity $I(\mathbf{q})$ the most convenient approach is the kinematical approximation. It assumes that the amplitude $A(\mathbf{q})$ of a scattered wave in a defined spacial direction is given by the summation over the contributions of all participating atoms while taking the phase information into account and neglecting multiple scattering. The scattering amplitude is displayed in equation 2.1

$$A(\mathbf{q}) = \sum_j f_j(\mathbf{q}) \mathrm{e}^{\mathrm{i}\mathbf{q}\cdot\mathbf{r}_j}, \tag{2.1}$$

where $f_j(\mathbf{r})$ and $\mathbf{r}_j$ are the atomic form factor of atom j and its atomic positions, respectively. The atomic form factor

$$f_j(\mathbf{r}) = r_\mathrm{e} \int \rho_j(\mathbf{r}) \mathrm{e}^{\mathrm{i}\mathbf{q}\cdot\mathbf{r}} d\mathbf{r} \tag{2.2}$$

is defined as the Fourier transform of the electron density distribution $\rho_j(\mathbf{r})$ for an atom j, where r_e is the classical electron radius. The wave vector transfer $\mathbf{q} = \mathbf{k}' - \mathbf{k}$ is defined as the difference between the scattered and incoming wave vector. The wave vector $\mathbf{k}$ points in the wave's direction of propagation per definition and its absolute value is given as

$$|\mathbf{k}| = \frac{2\pi}{\lambda}, \tag{2.3}$$

λ being the wavelength. In the case of elastic scattering this magnitude is conserved, i.e. $|\mathbf{k}| = |\mathbf{k}'|$. The wave vector transfer is dependent on the scattering angle 2θ and given as

$$|\mathbf{q}| = \frac{4\pi}{\lambda} \sin\theta. \tag{2.4}$$

Due to its generic nature $|\mathbf{q}|$ is independent of the choice of wavelength and therefore, is the ideal property to describe the scattering process.
Equation 2.1 can be used to calculate scattering processes for both orderless and crystalline samples for it expects no symmetric order of the atoms. Here, the focus lies on the investigation of ordered, crystalline samples. The obtainable measurement parameter at a scattering experiment is not the scattering amplitude $A(\mathbf{q})$ but the intensity $I(\mathbf{q})$ which is the square of the absolute value of the amplitude

$$I(\mathbf{q}) = |A(\mathbf{q})|^2. \tag{2.5}$$

Unfortunately, $A(\mathbf{q})$ cannot be obtained directly from $I(\mathbf{q})$ because of the missing phase information due to the squaring. In order to receive information on the crystal structure one has to exploit the highly symmetric properties of crystals. The crystal structure can be described by summation over the basis and the lattice. The basis dictates the positions $\boldsymbol{\delta}_j$ of the atoms in the unit cell while the lattice translation vector $\mathbf{r}_i = a\mathbf{n}_1 + b\mathbf{n}_2 + c\mathbf{n}_3$ locates the unit cells i in the crystal lattice. a, b and c are a set of integers. The position of every atom is consequently given by

$$\mathbf{r}_{ij} = \boldsymbol{\delta}_j + \mathbf{r}_i. \tag{2.6}$$

Utilizing the kinematical theory and neglecting the absorption of the primary beam equation 2.1 can be approximated as

$$A(\mathbf{q}) \sim S(\mathbf{q}) \cdot F(\mathbf{q}). \tag{2.7}$$

The structure factor

$$S(\mathbf{q}) = \sum_j^{\mathrm{cell}} f_j(\mathbf{q}) \mathrm{e}^{\mathrm{i}\mathbf{q}\cdot\boldsymbol{\delta}_j} \tag{2.8}$$

carries information on the crystal's unit cell and its scattering strength. The translation invariancy, i.e. the lattice periodicity is described by the lattice sum

$$F(\mathbf{q}) = \sum_i \mathrm{e}^{\mathrm{i}\mathbf{q}\cdot\mathbf{r}_i} = \sum_{abc} \mathrm{e}^{\mathrm{i}\mathbf{q}\cdot(a\mathbf{n}_1+b\mathbf{n}_2+c\mathbf{n}_3)}. \tag{2.9}$$

The lattice sum only provides a contribution different from zero for

$$\mathbf{q}\cdot\mathbf{r}_i = 2\pi\cdot m, \tag{2.10}$$

where m belongs to $\mathbb{Z}$. Introducing a reciprocal lattice $\mathbf{G}_{hkl} = h\mathbf{g}_1 + k\mathbf{g}_2 + l\mathbf{g}_3$ with the so called Miller indices h,k, and l and the reciprocal lattice vectors $\mathbf{g}_j$ leads to the Laue equation

$$\mathbf{q} = \mathbf{G}_{hkl}. \tag{2.11}$$

On the analogy of $\mathbf{r}_i$, $\mathbf{G}_{hkl}$ spans the reciprocal space, which is an orthonormal system to the real space. The reciprocal lattice is distinctly allocated to the crystal lattice. The connection of the real and reciprocal space is the Fourier transform. Each point of the reciprocal lattice is clearly linked to a family of lattice planes via

$$d_{hkl} = 2\pi/|\mathbf{G}_{hkl}|, \tag{2.12}$$

defined by the Miller indices, where d_{hkl} is the interplanar spacing of the lattice planes. The crystal structure corresponding to a measured intensity profile can be determined by matching those to calculated intensity profiles based on assumed structures. For details see [Warren90].
All diffraction experiments within this thesis were conducted in the coplanar scattering geometry, which is sketched in figure 2.1. This implies that both wave vectors $\mathbf{k}$ and $\mathbf{k}'$ lie in the same scattering plane. The components of the wave vector transfer in coplanar diffraction geometry are given by

$$q_\mathrm{x} = \frac{2\pi}{\lambda}(\cos\omega_\mathrm{f} - \cos\omega_\mathrm{i}) \tag{2.13}$$

and

$$q_\mathrm{z} = \frac{2\pi}{\lambda}(\sin\omega_\mathrm{f} + \sin\omega_\mathrm{i}). \tag{2.14}$$

Additionally, all experiments fulfilled the specular condition, where $\omega_\mathrm{i} = \omega_\mathrm{f} = 2\theta/2$ holds. Therefore, the wave vector transfer only contains the q_z-component.

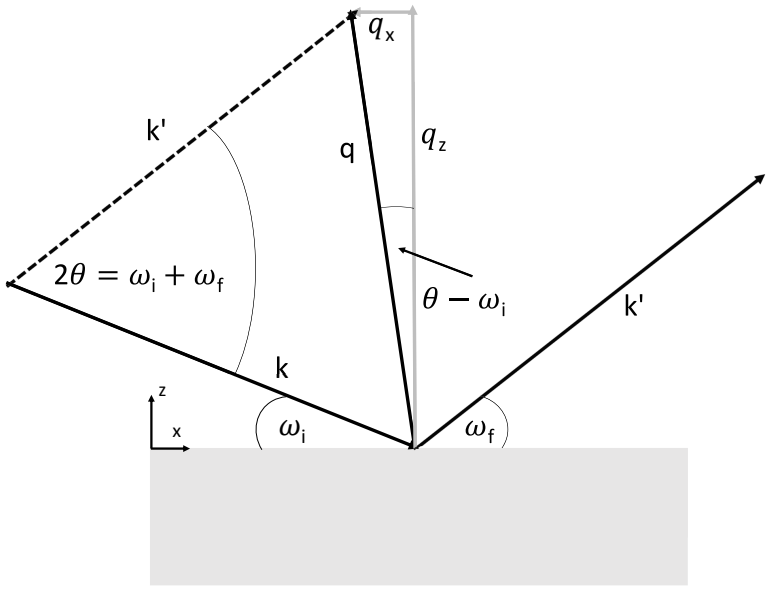

Figure 2.1: Sketch of the coplanar scattering geometry for a diffraction experiment. The incoming x-ray beam with wave vector **k** is scattered at the sample's surface. The scattered beam is then represented by the wave vector $\mathbf{k}'$.

2.2 Crystal truncation rods

The concept of crystal truncation rods (CTRs) arises if the crystal is not considered infinite but cleaved along a crystallographic axis. The cleaving of the crystal can be described as a multiplication of the infinite crystal structure with a step function. As discussed above, the real and reciprocal space are connected via the Fourier transform. Therefore, the multiplication becomes a convolution of the scattering amplitude, which shows δ-peaks due to the lattice sum (Bragg reflections) and the Fourier transform of the step function, which is proportional to $1/|q_z|^2$. This leads to a broadening of the sharp δ-peak structure resulting in streaks of scattering along the direction perpendicular to the crystal's surface referred to as CTRs. This process is depicted on the left side of figure 2.2. The analysis of CTRs delivers information on the crystal's surface structure and roughness [Robinson86, Tolan94].
In order to calculate the CTR of a crystal the kinematical approximation is used again. The intensity distribution for a semi-infinite crystal with a smooth surface is then given through

$$|A(q_z)|^2 = \left| \sum_{n=\ \infty}^{0} f(q_z) \mathrm{e}^{\ (\mathrm{i}q_z\ \ \mu)na} \right|^2 = |f(q_z)|^2 \left| \frac{1}{1 \quad \mathrm{e}^{(\mathrm{i}q_z\ \ \mu)a}} \right|^2, \tag{2.15}$$

where a is the lattice constant along the z-direction, μ is the absorption factor and n sums over the lattice planes. This equation is used to model the substrate of a layer

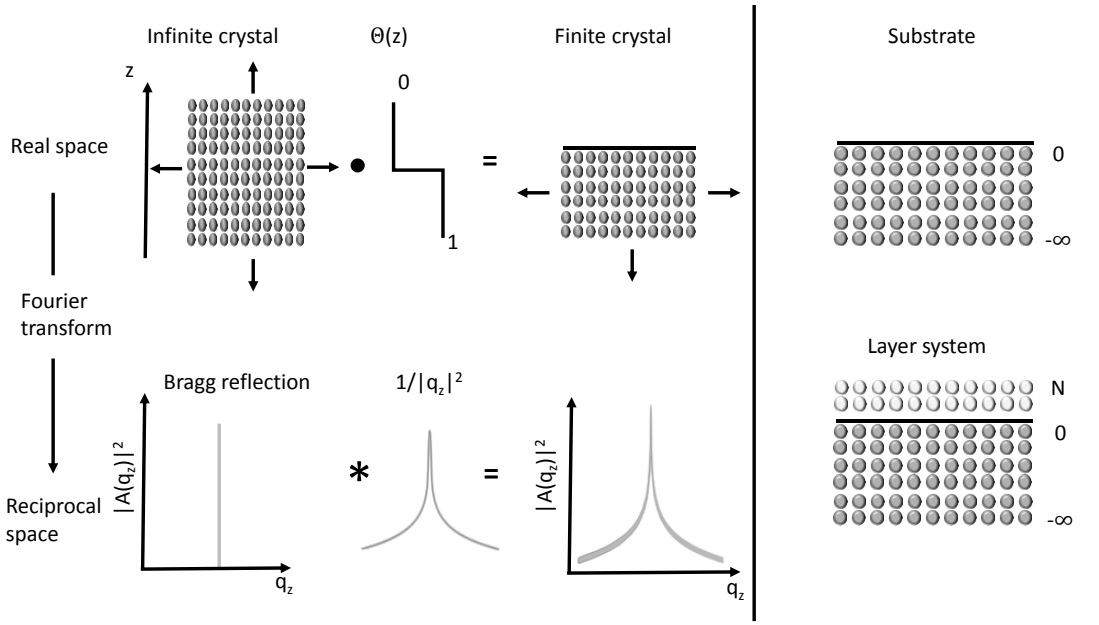

Figure 2.2: Left: The cleaving of an infinite crystal can be described as a multiplication of the infinite crystal's structure and a step function in the real space. The infinite structure generates Bragg reflections appearing as δ-peaks in the reciprocal space. The convolution of the Fourier transform of the step function and the scattered intensity leads to streaks of scattering perpendicular to the samples surface, referred to as crystal truncation rods. Right: Visualization of the summation limits of equations 2.15 and 2.16. The substrate of a layer system is modeled by an semi-infinite crystal, while the layer is treated as a finite crystal.

system. The intensity distribution of a layer, i.e. a finite crystal consisting of N lattice planes, can be written as

$$|A(q_z)|^2 = \left| \sum_{n=1}^{N} f(q_z) \mathrm{e}^{\ (\mathrm{i}q_z \ \ \mu)na} \right|^2 = |f(q_z)|^2 \left| \frac{1 \quad \mathrm{e}^{(\mathrm{i}q_z \ \ \mu)(N+1)a}}{1 \quad \mathrm{e}^{(\mathrm{i}q_z \ \ \mu)na}} \quad 1 \right|^2 \tag{2.16}$$

applying the partial sum of the geometrical series $\sum_{n=0}^{N} {}^{1} bq^n = b\frac{1}{1} \frac{q^N}{q}$. The factor 1 compensates the summation over $n = 0$, which is needed to apply the partial sum of the geometrical series. The roughness of the surface can be included by a model introduced by Robinson et al. [Robinson86]. It basically assumes an additional layer with a given probability for the occupation of every unit cell.
In order to calculate and modulate the scattered intensity in close vicinity of the Bragg reflection itself the kinematical approximation does not hold and dynamical effects e.g. multiple scattering have to be taken into account [Als-Nielsen11].
The scattered intensity for a GaAs substrate with a GaMnAs layer can be calculated by

$$|A(q_z)|^2 = |A_{\mathrm{GaAs}}(q_z) + A_{\mathrm{GaMnAs}}(q_z)|^2, \tag{2.17}$$

where $A_{\mathrm{GaAs}}(q_{\mathrm{z}})$ and $A_{\mathrm{GaMnAs}}(q_{\mathrm{z}})$ follow equations 2.15 and 2.16, respectively. For such a layer system so called thickness fringes occur along the CTR, originating from the interference of the scattered x-rays at both the layer and substrate [Wie89]. The spacing Δq_{z} between the observed interference oscillations allows the determination of the layer thickness

$$d = \frac{2\pi}{\Delta q_{\mathrm{z}}} \tag{2.18}$$

for a bilayer system.

Chapter 3

Structural and magnetic properties of GaMnAs

3.1 Ferromagnetism

The ferromagnetism in any solid is introduced via exchange interaction between adjacent spins which is again caused by the Pauli principle [Lèvy00]. The dipole-dipole interaction between spins on the other hand is much too weak to create ferromagnetic order on a long range [Lèvy00]. The Heisenberg Hamiltonian $\hat{H}$ [Heisenberg26, Dirac26] describes this coupling between adjacent spins and is given as

$$\hat{H} = -J \sum_{<i,j>} \mathbf{s_i} \cdot \mathbf{s_j}, \tag{3.1}$$

where $\mathbf{s_i}$, $\mathbf{s_j}$, and J represent the two spins and their coupling constant, respectively. There are two cases to consider depending on the sign of J. For $J > 0$ a parallel orientation of the spins is favored leading to a ferromagnetic order. The antiferromagnetic case for $J < 0$ favors an antiparallel orientation of the involved spins [Lèvy00].

The direct coupling only leads to a ferromagnetic order if the wave functions of the corresponding atoms overlap, which is the case for only a few materials, for example iron. The antiparallel orientation is reached via indirect coupling in most cases. For example, the so called superexchange [Kramers34, Anderson50]. This mechanism is observed in insulators like MnO, where the transition metal cations are separated by oxygen anions. Here, the spin of the manganese electrons couple antiferromagnetically via the oxygen spins. Both exchanges are sketched in figure 3.1. According to the Goodenough-Kanamori rules [Goodenough55, Kanamori59] a ferromagnetic orientation can also be achieved via superexchange, if the angle between the Mn-O-Mn group is not 180 ° but 90 °. Considering the spin-orbit coupling with superexchange an antisymmetric exchange is introduced, which results in weak antisymmetric coupling [Dzyaloshinsky58, Moriya60]. The ferromagnetic properties of all ferromagnetic materials emerge below the magnetic transition or Curie temperature T_C due to a second-order phase transition.

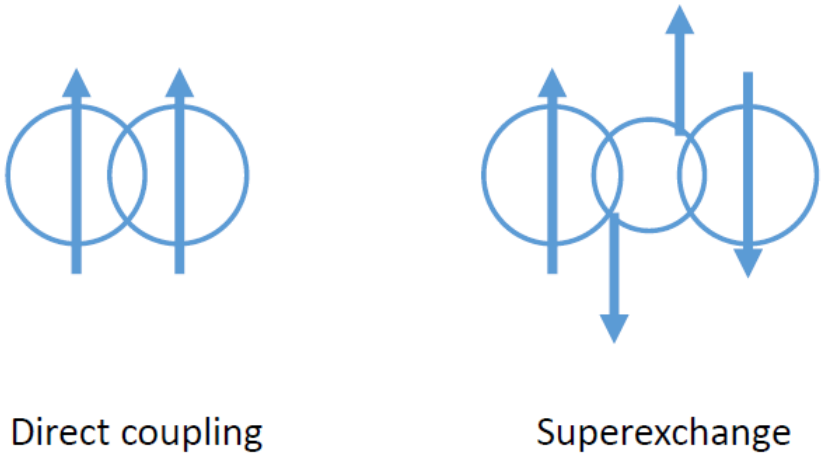

Figure 3.1: Left: The direct coupling between two adjacent spins via overlapping wave functions. Right: Antiferromagnetic coupling via superexchange.

3.2 The diluted magnetic semiconductor GaMnAs

In today's information technology, the processing and storage of information is strictly separated [Ohno98]. Utilizing the spin of electrons the storage of information is realized by ferromagnetic materials, while devices made of semiconductors are used to process data by taking advantage of the charge of electrons. Therefore, materials combining both semiconducting and magnetic properties could revolutionize the field of spintronics [IOPScience02, Tanaka05, Maekawa06]. In fact, there are already some ferromagnetic semiconductors like manganites or europium chalcogenides with Curie temperatures T_C around 350 K and 100 K, respectively [Coey99, Schlipf13]. The natural ferromagnetic materials are no candidates for mass production due to difficult growing conditions and, most importantly, comparably low mobility of free carriers [Ohno98].
One possible way can be the doping of non-magnetic semiconductors with magnetic atoms. There a several potential doping atoms like chromium or iron [Dietl02]. Manganese is the most common variant due to it's half filled $3d$-shell resulting in a maximum magnetic moment of $5/2\,\mu_B$. These kind of semiconductors are called diluted magnetic semiconductors (DMS) because of the low concentration of magnetic atoms incorporated into the host lattice.
Alongside, GaMnN which seemed to be a promising candidate [Dietl00] GaMnAs was intensively studied [Liu06, Dietl10] since its realization by Ohno et al. [Ohno96]. However, optical absorption and photoconductivity measurements have shown that the Mn acceptor level lies approximately 1 eV above the the valance-band edge of GaN [Graf02, Korotkov02]. Therefore, the realization of carrier induced ferromagnetism in GaMnN is highly unlikely [Graf03].

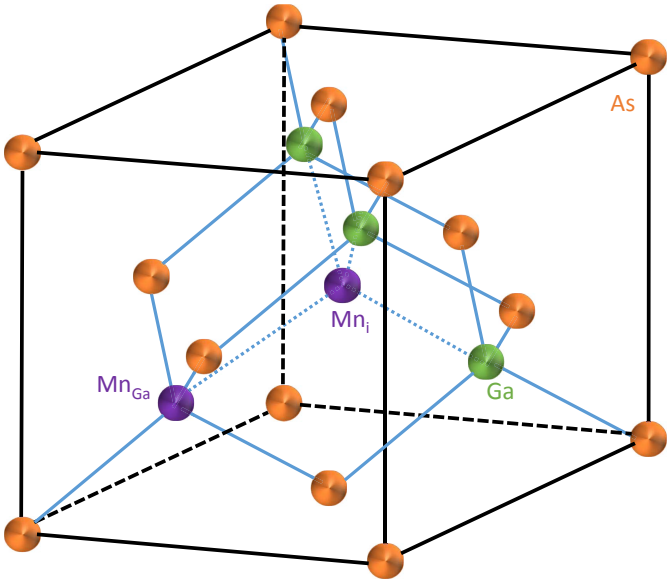

Figure 3.2: The zinc blende structure of GaAs including possible positions of the Mn atoms. The favorable option is Mn replacing a Ga atom (Mn_{Ga}). The manganese atoms then couple ferromagnetically and serve as a shallow acceptor. The second option is Mn occupies interstitial positions (Mn_i) acting as a deep donor and coupling antiferromagnetically.

3.2.1 Low temperature fabrication and resulting crystal structure of GaMnAs

GaAs structures are usually fabricated utilizing molecular beam epitaxy (MBE) at substrate temperatures of about 600 °C resulting in a zinc blende structure. GaAs grown at low substrate temperatures of typically 200 °C 300 °C is called low-temperature GaAs (LT-GaAs). The lattice constant of LT-GaAs is about 0.08 % larger than GaAs due to impurities in the zinc blende structure in the form of arsenic antisites [Liu95]. First attempts of fabricating ferromagnetic GaMnAs have revealed that the solubility of Mn is not sufficient to reach a magnetic order. However, using the low substrate temperatures during the growth process, sufficient Mn doping concentrations are realized [Ohno96]. GaMnAs grown under these conditions is referred to as low temperature GaMnAs (LT-GaMnAs).
Unlike GaAs, MnAs grows in an hexagonal NiAs structure [Wilson64] and is antiferromagnetic. Due to the cold substrate temperatures during the LT-MBE the formation of MnAs clusters is suppressed. The Mn atoms are therefore included into the zinc blende structure of the GaAs, where two common positions of the Mn atoms are observed as can be seen in figure 3.2 [Blinowski03]. The ideal case is the substitution of Ga sites (Mn_{Ga}). The second common position though less favorable are manganese interstitials Mn_i. In the former case Mn acts as an acceptor due to its electronic configuration; one $4p$ electron less than Ga. The latter leads to Mn serving as a double donor. These interstitials play an important role with respect to the hole concentration and therefore

the Curie temperature [Maca02, Yu02] and magnetic properties, which are discussed in 3.2.2. The Curie temperature is connected to the hole density p via

$$T_{\mathrm{C}} \propto x \cdot p^{1/3}, \tag{3.2}$$

where x is the manganese content [Dietl00, Wang04]. Improvements to the growth process have given rise to higher magnetic transition temperatures up to 190 K in heavily Mn-doped (20%) thin films [Chen09] and even 250 K for Mn delta-doped GaAs with AlGaAs layers [Nazmul05].
Manganese interstitials also have an impact on the crystal structure and lattice parameters [Masek03]. It has been widely discussed if Vegard's law [Vegard21], predicting a linear correlation between the lattice constant and the crystals composition, could be applied to GaMnAs due to the influence of arsenic antisites on the lattice constant. On the one, hand Schott et al. and Ohno have shown the linear proportionality between lattice constant and manganese concentration [Schott01, Ohno99]. On the other hand, Schott et al. fabricated structures identical in composition but varying in lattice constant [Schott03]. Thus, the lattice constant strongly depends on the growth conditions such as substrate or Mn cell temperature. A determination of the manganese concentration via XRD is therefore unrewarding. Nevertheless, XRD provides information on the quality of the material. The closer the lattice constant is compared to LT-GaAs, the less impurities exist in the grown crystal structure.
The growth parameters do also affect the electric properties of GaMnAs films as presented in figure 3.3 [Ohno99]. Substrate temperatures below 175 °C lead to polycrystalline films, while higher temperatures enable the formation of MnAs clusters. Only in the range of about 200 °C−300 °C metallic monocrystalline films can be grown. However, even in this range too low or high Mn compositions do not provide a sufficient charge carrier density leading to non-ferromagnetic, insulating GaMnAs.
The growth of monocrystalline, metallic, and ferromagnetic GaMnAs with LT-MBE depends heavily on the growth parameters. The same parameters also dictate the magnetic properties of GaMnAs which are discussed in the following section.

3.2.2 Magnetic properties of GaMnAs

Manganese atoms hold a maximum magnetic moment of $5/2\,\mu_{\mathrm{B}}$ [Dietl02], which is no guarantee for a long-range ferromagnetic order. Due to the small Mn content in GaMnAs the distances between the atoms are too large for two adjacent atoms to couple directly, as indicated in figure 3.4 a). As mentioned in section 3.2.1, Mn acts as an acceptor effectively increasing the hole density when it substitutes a Ga atom in the zinc blende structure. Alternatively, Mn can occupy interstitials in the crystal structure. These $\mathrm{Mn_i}$ are ionized doubly decreasing the effective hole density by three in contrast to the $\mathrm{Mn_{Ga}}$. Moreover, the exchange of two adjacent Mn spins is antiferromagnetic [vonMolnar91]. Consequently, the ferromagnetism is induced by indirect coupling of free carriers. The spins of a non-localized hole and a localized Mn ion are aligned oppositely. Due to the kinematic exchange between two Mn ions via the hole, every Mn ion within the hole's reach is aligned as illustrated in figure 3.4 b) [MacDonald05]. Since Mn itself acts as

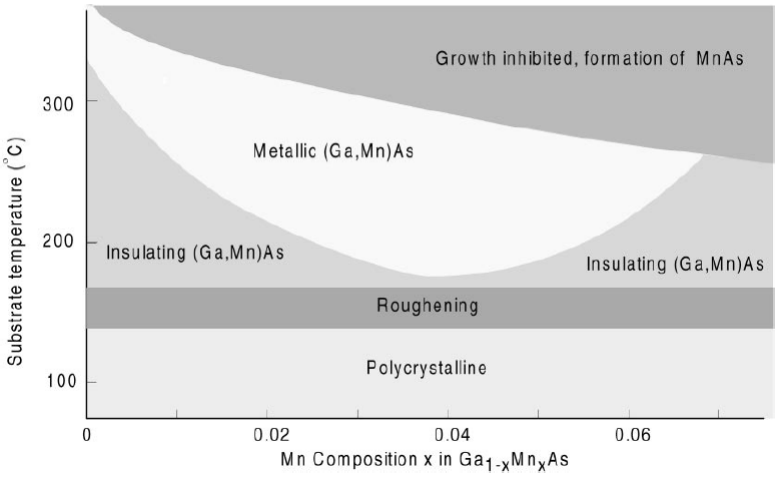

Figure 3.3: The parameter space displays the impact of Mn concentration and substrate temperature on the electric properties of LT-MBE grown GaMnAs. Reprinted from Journal of Magnetism and Magnetic Materials, 200, Ohno, H., Properties of ferromagnetic III-V semiconductors, 110-129, Copyright (1999), with permission from Elsevier.

an acceptor, the hole density is sufficient to form a far-reaching ferromagnetic order as depicted in figure 3.4 c). As the hole density is essential for the ferromagnetism, a great amount of Mn_i can not only hinder the conductivity but inhibit a ferromagnetic order. The reduction of these interstitials depends heavily on the Mn content, growth conditions, and post growth treatment, typically resulting in hole densities of about $10^{20}\,\mathrm{cm}^{-3}$ [Glunk09]. The lack of a ferromagnetic order at low Mn concentrations of about 1 % can also be explained by an insufficient hole density.
An in-depth theoretical description is given by Krstajic et al. [Krstajic04] or Dietl et al. [Dietl01]. Although, the theoretical understanding is not completed so far, the mean-field approach by Dietl et al. [Dietl01] taking into account the hole mediated ferromagnetism, yields results in good agreement to experimental observations.
The ferromagnetism in most materials shows a directional dependence, which is called magnetic anisotropy. This means that the magnetic moment tends to align along a so called easy axis. This is also the case for GaMnAs. Apart from the shape and strain of the material the spin-orbit interaction plays an important role in the formation of magnetic anisotropy. The local Mn ions themselves have no influence on the anisotropy due to their vanishing angular momentum [Jungwirth06]. For unstrained GaMnAs a cubic anisotropy with easy axes along the <100> and <110> directions has been theoretically predicted by Dietl et al. [Dietl01]. Again the hole concentration is of crucial importance dictating direction of the easy axis in this mean field model. In most cases GaMnAs layers grow pseudomorphic, which means that the parallel component of the lattice constant follows the substrate, whereas the perpendicular component is strained resulting in a tetragonal distortion. The introduced strain breaks the cubic symmetry of the crystal, resulting in an uniaxial magnetic anisotropy [Glunk09]. The easy axis

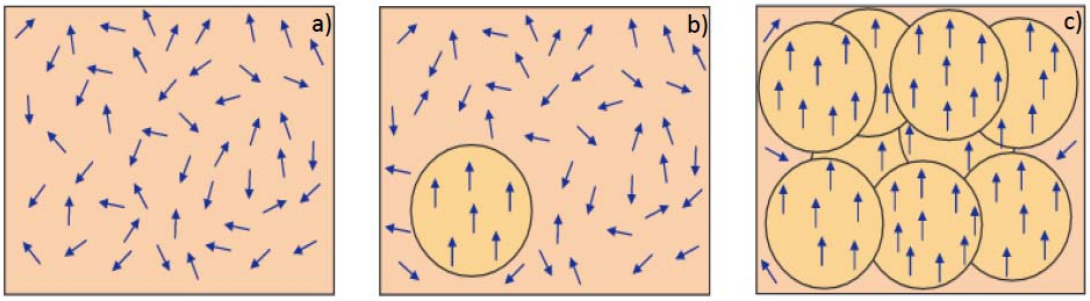

Figure 3.4: Concept of carrier induced ferromagnetism in GaMnAs. a) Random spin orientations due to the negligible next neighbor interaction. b) Free hole mediates interactions between adjacent spins in the carrier's range. c) Long range order caused by the overlap of holes resulting in a ferromagnetic phase. Reprinted and adapted by permission from Macmillan Publishers LTD: NATURE MATERIALS, 4, MacDonald, A. H., Schiffer, P. and Samarth, N, Ferromagnetic semiconductors: moving beyond (Ga,Mn)As, 195-202, Copyright (2005).

lies either in-plane or out-of-plane for either compressive or tensile strain. Furthermore, experiments have revealed an easy axis along the [110] direction, which cannot be explained by the underlying symmetry [Liu03, Welp04, Sawicki05]. Welp et al. also observed a change of the easy axis with temperature occurring at around $T_C/2$ [Welp03]. Another important property is the so called magnetostriction identified by Joule in 1847 [Joule47] for iron and steel bars. It describes the change in dimension that ferromagnetic materials undergo during the magnetization process. This magnetization process can occur spontaneous due to the ferromagnetic phase transition or induced by an external magnetic field [Chikazumi64]. The reason for this change is again the magnetic anisotropy. The material tends to rearrange its structure to align its easy axis to an applied magnetic field resulting in a strain in the range of 10^{-4} - 10^{-5} [James98], which translates to magnetostriction coefficients λ of 10^{-6} - 10^{-8} [Klokholm76, Tam88]. The magnetostriction coefficients $\lambda = \Delta l/l$ describe the strain's saturation value. The spontaneous magnetostriction or volume magnetostriction has been measured for rare-earth based permanent-magnetic materials such as Ce_2Fe_{17} [Andreev00] and the diluted magnetic semiconductor $Cd_{1-x}Mn_xGeAs_2$ [Mollaev11] by means of XRD and strain measurements under high pressures up to 7 GPa, respectively.
The magnetostriction constants of GaMnAs were experimentally determined via nanomechanical measurements, where magnetic fields were applied to the sample introducing magnetoelastical stretching and compression, to be on the order of $1 \cdot 10^{-5}$ at 4.2 K, which resulted in a strain of $-0.4\,\%$ along the [110] direction [Masmanidis05]. In this work, they observed a similar temperature dependence of both magnetostriction and magnetic anisotropy and conclude that their and related observations [Sawicki03, Sawicki05] have their origin in an increase in carrier density with temperature. Moreover, thermal lattice expansion may have an impact, as it changes sign in the same temperature range as the magnetostriction and magnetic anisotropy [Novikova61, Sparks67]. The investigation of the impact of spontaneous magnetostriction, with and without an in-plane magnetic

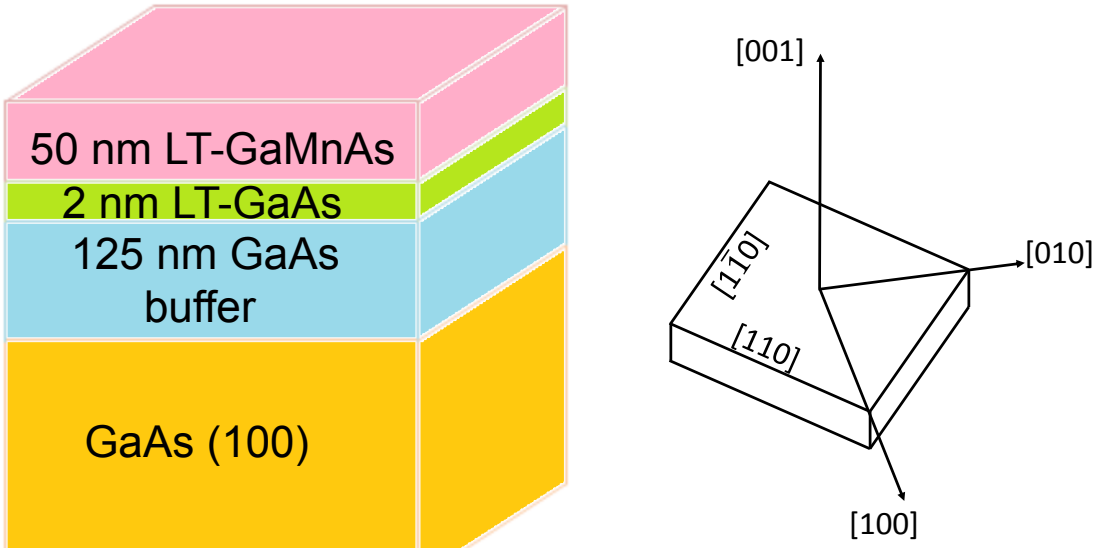

Figure 3.5: Left: Sample 90127A. A 50 nm-thick LT-GaMnAs layer is epitaxially grown on a (100) GaAs substrate, which is capped by a 125 nm buffer layer. Right: Coordinate system used within this thesis.

field applied, on the lattice parameters of two GaMnAs samples, introduced in the next section, is one of the goals of this thesis.

3.2.3 The investigated GaMnAs samples

During this thesis a series of XRD experiments were conducted on two GaMnAs samples 61212A and 90127A with T_C of 50 K and 110 K, respectively. Both samples were grown, prepared, and provided by the group of Jacek Furdyna at the University of Notre Dame, Indiana. Figure 3.5 depicts a sketch of sample 90127A. For sample 90127A a GaAs buffer layer of 125 nm was epitaxially grown on a semi-insulating (100) GaAs substrate. The buffer layer is followed by a 2 nm LT-GaAs layer grown at a reduced substrate temperature. The GaMnAs film was also grown at the low substrate temperature resulting in a 50 nm thick LT-GaMnAs layer with a Mn concentration of about five percent. Afterwards the sample was annealed at 270 °C in nitrogen gas flow for one hour. The easy axis was found to be in the plane of the sample and the corresponding saturation magnetization was measured to be about 2 mT at 10 K by the group of Manfred Bayer at Technische Univeristät Dortmund utilizing Kerr rotation. Typically, fields of about 100 mT - 200 mT are needed for out-of-plane magnetization [Lang05] for the whole ferromagnetic temperature range.
The growth process of sample 61212A was quite similar, which therefore resulted in a similar layer structure. The buffer, LT-GaAs, and LT-GaMnAs layer thicknesses are 150 nm, 2 nm, and 50 nm, respectively. The Mn concentration of the LT-GaMnAs

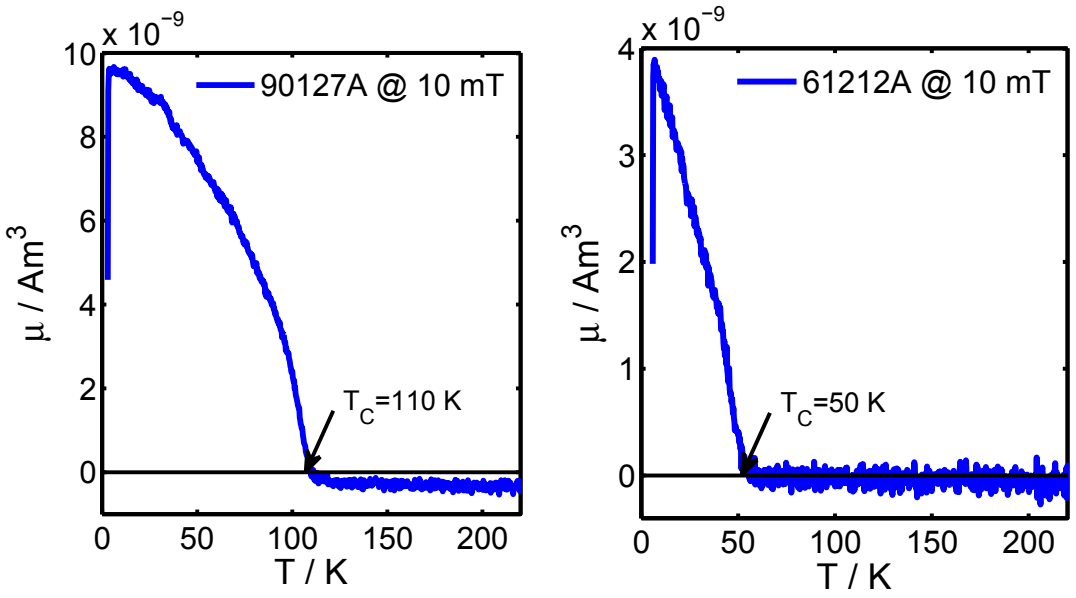

Figure 3.6: Left: Measured magnetic moment of sample 90127A in dependency on the temperature in order to determine T_C. A magnetic field of 10 mT was applied. T_C was determined to 110 K. Right: Magnetic moment measured for sample 61212A with an applied magnetic field of 10 mT. T_C was determined to 50 K. The measurements were conducted by the group of Michael Farle at Universität Duisburg-Essen utilizing a VSM.

layer is about 5 %. T_C of both samples was determined utilizing a vibrating sample magnetometer (VSM) [Foner59] by Ulf Wiedwald in the group of Michael Farle at Universität Duisburg-Essen. The VSM consists of an electromagnet, which supplies a homogeneous magnetic field. A piezoelectric material is used to cause vibrations of the sample holder and therefore the sample. Here, it is crucial that the sample oscillates perpendicular to the applied magnetic field. The induced voltage can be detected in special oriented coils and is proportional to the magnetic moment of the sample. Therefore, the VSM can be used to determine T_C of any given sample by measuring the magnetic moment in dependency of the temperature. Figure 3.6 shows these measurements conducted on samples 90127A and 61212A on the left and right side, respectively. T_C was determined to 110 K (90127A) and 50 K (61212A). The significant difference in T_C results from the post-growth annealing, which was not performed on sample 61212A.

X-ray reflectivity (XRR) measurements were conducted on sample 90127A in order to characterize the sample with focus on layer thickness and quality. The XRR technique is sensitive to changes in electron density perpendicular to the sample's surface and additionally supplies information on the surface and interface characteristics like layer thickness and roughness and is described in the literature, for instance in [Tolan99] and [Als-Nielsen11].

Figure 3.7 shows the reflectivity curve measured at BL9 at DELTA, which is described

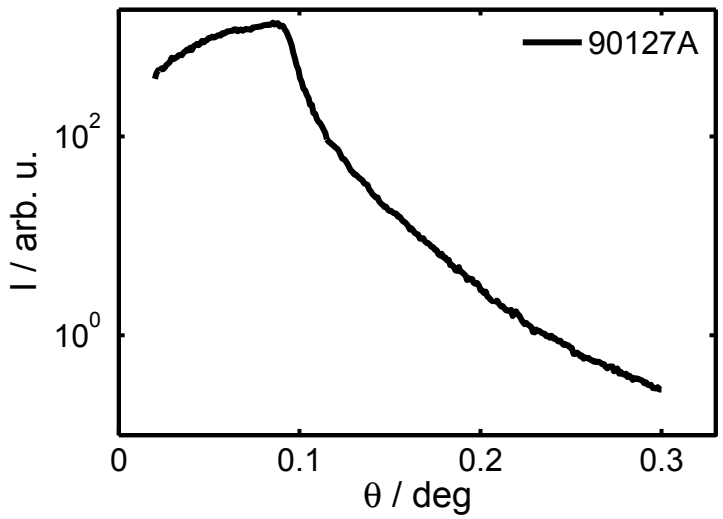

Figure 3.7: Measured reflectivity of sample 90127A. No oscillations can be observed due to the low electron density contrast between the GaAs substrate and GaMnAs layer.

in chapter 4.1. Because of the relatively low Mn concentration the electron density contrast ($\Delta\rho = 1 \cdot 10^{-3}\,\mathrm{e}^-/\mathrm{\AA}^3$) is not sufficient to determine the layer thickness from the measured reflectivity. The XRR measurements were also used to verify the suitability of the samples, i.e. plane, for the conducted XRD experiments within this thesis. Another sample (100413A) was sorted out during this process due to it's crooked surface.

Due to the wide scanning range of the XRD experiments conducted at the ESRF a variety of oscillations was observed. A typical truncation rod is shown in figure 3.8. The position of these oscillations were used to determine the layer thickness of both samples for each temperature. The positions were determined analogous to the positions of the Bragg reflections by fitting a Gaussian function to each oscillation, which is further elaborated in chapter 5. These fits are depicted in red in figure 3.8. The separation of the oscillations on the wave vector transfer scale Δq_{osc} has been determined accordingly. Utilizing equation 2.18 the layer thicknesses d_{layer} were determined and are plotted in figure 3.9. d_{layer} can be estimated to $(49.5 \pm 1)\,\mathrm{nm}$ and $(47.5 \pm 1)\,\mathrm{nm}$ for the samples 90127A and 61212A, respectively concurring to the 50 nm thickness stated above. The effect of thermal heating on the layer thickness, which can be estimated to $8 \cdot 10^{-2}\,\mathrm{nm}$ for 100 K could not be observed, since the accuracy of the determination of d_{layer} is only approximately 1 nm.

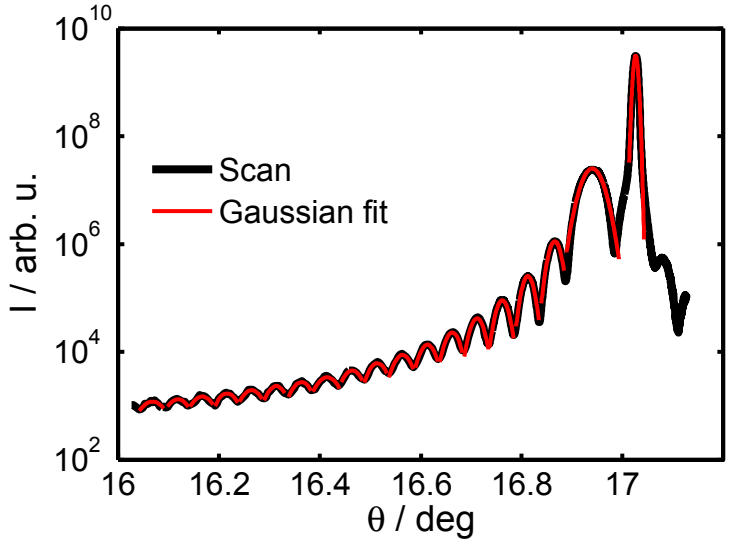

Figure 3.8: Generic truncation rod detected at the XMaS beamline at ESRF. Gaussian fits were utilized to determine the positions of the oscillations (red).

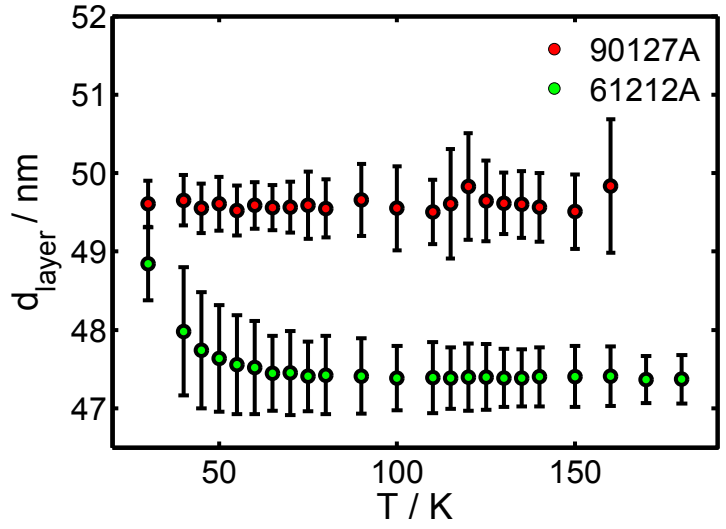

Figure 3.9: The layer thicknesses d_{layer} of both samples in dependency of the temperature.

Chapter 4

Development and construction of a cyrogenic setup at DELTA

For the investigation of structural changes due to magnetostriction in diluted magnetic semiconductors a resolution of $\Delta q \leq 10^{-4}\,\text{Å}^{-1}$ is needed. In order to reach Bragg angles of interest a variable photon energy is helpful. Table 4.1 displays the Bragg and scattering angles of the GaAs (004) Bragg reflection for different photon energies assuming a lattice constant of $a = 5.65325$ at 300 K [Blakemore82]. A synchrotron radiation facility fulfills both conditions. Therefore, the XRD experiments were conducted at beamline BL9 of DELTA the synchrotron radiation facility at TU Dortmund and beamline BM28 at ESRF. First, beamline BL9 is introduced. In a second step the development of a cyrogenic setup at BL9 is discussed. Here, the focus lay on a stable sample alignment, position and temperature. Different sample environments are introduced including two continuous flow cyrostats and a cryostream system. The beamline BM28 and the experimental setup on site is described in the last part of this chapter.

θ / °	2θ / °	E / keV
33.024	66.048	8
19.719	39.438	13
17.003	34.006	15
12.669	25.338	20

Table 4.1: Bragg and scattering angles of the GaAs (004) Bragg reflection for different photon energies at 300 K.

For the investigation of GaMnAs samples with T_C of 50 K and 110 K liquid helium and nitrogen as cooling agents are mandatory, respectively. The handling of this liquefied gases, especially helium, requires specific attention. In order to cool the sample most effectively with liquid helium, it should be evaporated as close as possible to the position of the sample. This is maintained by transporting the liquid helium, which is stored in a Dewar vessel thermally isolating it from the room temperature environment, through double-walled helium transfer tubes, where the outer tube is evacuated. These

transfer tubes are available in so called L- and U-shapes with different variations in length an flexibility reaching from completely stiff to semi-flexible. Additionally, the sample cell or cryostat is evacuated continuously by a turbomolecular pump in order to prevent the freezing of any molecules and to avoid contamination of the sample.
The first step to an cryogenic setup is the choice of cryostat. One can distinguish the cryostats used within this thesis in two categories; closed-cycle and continuous-flow cryostats. In a continuous-flow cryostat the liquid helium enters the cryostat through the transfer tube, which is firmly fixed at the entrance arm. It is then pumped through the cryostat and either leaves it through an extra exit or the transfer tube into the recovery. Mounting such an cryostat onto the diffractometer of beamline BL9 has the disadvantage of limiting the accessible range of scattering angles due to the firmly fixed transfer tubes to about $14\,^{\circ}$.
The closed-cycle cryostat on the other hand contains an own helium reservoir. The cold gas is liquefied within a close cycle by an integrated pump. In [Tiemeyer12] such an closed-cycle cryostat was used to carry out experiments at BL9. They found that there is a loss of angular resolution due to the vibrations caused by the integrated pump which made a detailed investigation at a stable sample position impossible. Therefore, a continuous flow cryostat was used for both their experiments and the experiments conducted within this thesis.

4.1 The beamline BL9 @ DELTA

The beamline BL9 located at DELTA offers the opportunity to make use of a broad variety of experimental methods such as XRD, XRR or small angle x-ray scattering (SAXS) [Krywka06]. Figure 4.1 shows a schematic of beamline BL9. The synchrotron radiation for BL9 is produced by a superconducting asymetric wiggler (SAW) with a critical energy of 7.9 keV. The emitted polychromatic beam is then monochromatized and horizontally focused by a silicon (311) double crystal system. The photon energy is tunable in a range from 5 keV - 30 keV with an energy resolution of $dE/E = 10^{-4}$. The typical photon flux at 13 keV is $5 \cdot 10^9$ photons/s/mm^2. In order to protect the detector and samples from radiation damage an absorber and fast-shutter system is installed.
The beamline is equipped with a six-circle diffractometer from Huber. The degrees of freedom of the sample that are relevant for the alignment are indicated in figure 4.1. These are movement along the z- and x-direction and the angles θ and X, which describe the tilting parallel and perpendicular to the direction of the x-ray beam, respectively. Different detectors like a MAR345 image plate detector, a NaI pointdetector or a Piltaus 100K 2D array detector are available. For the experiments carried out at BL9 the Pilatus 100K [Dectris14] detector was used. The integrated sensor is a silicon diode array with a sensitive area of $83.8\,\text{mm} \cdot 33.5\,\text{mm}$. The sensor consists of 94965 pixels with a size of $172\,\mu\text{m} \cdot 172\,\mu\text{m}$. A region of interest (ROI) of typical $3 \cdot 40$ pixels was defined for each experiment utilizing the Pilatus 100K detector as a virtual point detector.

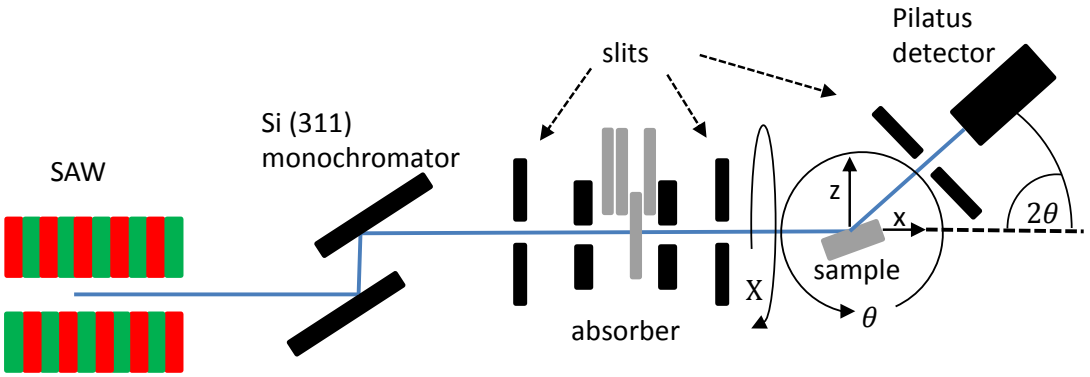

Figure 4.1: Schematic drawing of the beamline BL9 of DELTA. The Si (311) double crystal monochromatizes and horizontally focuses the polychromatic beam emitted by the SAW. The beam passes various slits and an absorber system before reaching the sample. The scattered intensity is then detected by the Pilatus 100K detector. The sample's degrees of freedom used for the sample alignment are indicated.

4.2 CryoVac continuous-flow cryostat setup

The setup described in this section is similar to the one used by [Tiemeyer12]. In order to investigate a GaMnAs wafer with T_C of 50 K (sample 61212A) described in 3.5, a CryoVac micro cryostat [CryoVac17] was mounted on the sample stage of Beamline BL9 at DELTA. In order to perform XRD measurements with the cryostat two modifications were necessary. First, the sample position more specifically the cold finger had to be elevated or extended by a cylindrical brass sample holder, because the heating shield of the cryostat surrounds the cold finger making it impossible to access the sample with the x-ray beam. Secondly, a cylindrical cover plate with Kapton windows was mounted on the cryostat to ensure x-ray accessibility.
Temperature control of the cold finger was maintained by a controller measuring the temperature inside the heating shield. An additional Cernox low temperature sensor [Courts03] was placed with silver conductive paint nearby the sample position measuring the sample temperature more precisely.
The liquid helium was supplied via a semi-flexible U-shaped transfer tube to the cryostat. Since the sample cell has an horizontal entry arm an additional rigid L-shaped transfer tube was used. The inflexibility of the combination of two rigid transfer tubes and the cryostat limited the feasibility of the experiment to small θ-angles of about 14 °.

Sample alignment

The goal of the conducted experiments was to determine lattice distortions in a GaMnAs thin film due to magnetostriction. Using the GaAs substrate reflection as an internal reference the relative changes between the GaAs and GaMnAs layer (004) Bragg reflections were investigated in order to separate the thermal effect on the lattice

distortion from changes due to magnetostriction.
Choosing an electron energy of 20 keV resulted in manageable Bragg angles of θ = 12.669 ° - 12.673 ° in a temperature range from 100 K - 300 K for the (004) GaAs reflection and still provided sufficient resolution. The beamsize was set to 1 mm in height and 1.5 mm in width. The sample was placed on the extended cold finger of the cryostat via silver conductive paint for an excellent thermal transfer. Because of the small expected changes ($5 \cdot 10^{-5}$Å) on the lattice the sample alignment was a great issue. In a first step the Pilatus 100K detector was placed vis-*à*-vis the direction of the incident beam identifying its ROI on the detector. In the next step the sample was moved into the x-ray. By conducting z- and θ-scans alternately while reducing the scanning range each step the sample position was adjusted in height, i.e. placed till it shades half of the incident beam's intensity. The θ-scans allowed to align the sample surface parallel to the direction of the incident beam. For the second part of the alignment θ and 2θ were set to the (004) Bragg GaAs reflection. At this point, the transfer tubes were put into the cryostat and Dewar vessel and the cooling process was initiated. Then, the first step was to find the reflection on the detector with θ-scans. The challenge here was to find an adequate combination of scan-range and -increment. If the scanning range was too narrow the reflection might not hit the detector, but if it was too vast one might miss the reflection if the increment was not small enough, since the reflection is only about 0.01 ° wide. Subsequently the objective was to get the reflex into the ROI on the detector with the maximum intensity. This could be achieved by scanning the angles 2θ and X where X is the angle the sample is tilted perpendicular to the x-ray beam. The 2θ and X motors move the reflection vertically and horizontally on the detector, respectively. All three scans were repeated several times decreasing scanning ranges each iteration until all values did not change anymore. In a last step θ was set to the value of $2\theta/2$. A typical θ - 2θ scan of the GaAs Bragg reflection is displayed in figure 4.2.

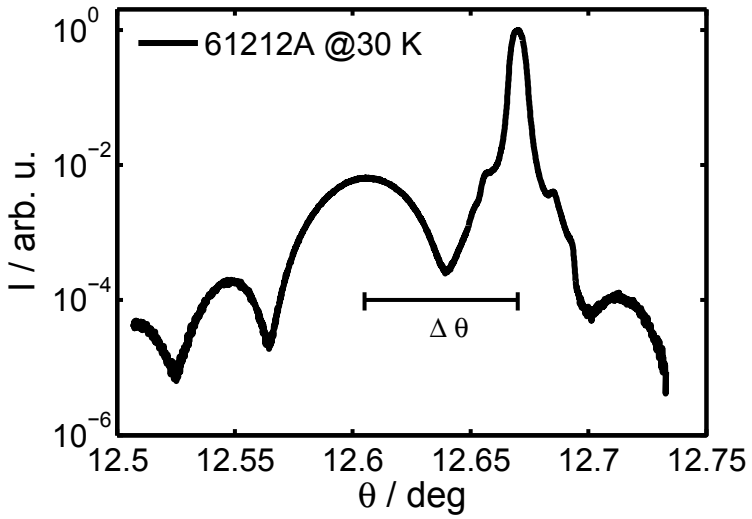

Figure 4.2: A generic measured (004) GaMnAs Bragg reflection at 30 K.

It consists of 2500 steps and took approximately one hour. After each scan the temperature was altered. Since the change in temperature has direct impact on the sample position due to the thermal expansion of both the sample holder and the sample itself, the sample had to be re-aligned. Due to the stiffness of the setup it was not possible to move the θ motor more than 2 ° without bending or breaking the firmly fixed helium transfer tube. Also, the transfer tube could not be removed from either the Dewar nor cryostat, which would interrupt the cooling process. Therefore, it was impossible to align the height at $\theta = 2\theta = 0\,°$. Subsequently, the height had to be aligned with θ and 2θ set to the (004) Bragg reflection. After this height alignment all three angles (θ, 2θ, X) are readjusted and the next scan was started.

Results and discussion

The GaAs and GaMnAs (004) Bragg reflections of sample 61212A were measured at 14 temperatures; five below and nine above the nominal T_C. The temperatures 20 K, 40 K, 60 K, and 75 K were measured twice and the right side of figure 4.3 shows the averaged angular separation $\Delta\theta = \theta_{GaAs} - \theta_{GaMnAs}$ of the GaAs and GaMnAs (004) Bragg reflections referenced to $\Delta\theta(99\,K)$ with the corresponding errors. For the data points that were measured once, the largest error is anticipated. The data treatment will be further elaborated in chapter 5.
The sample temperature calibration with the introduced Cernox sensor at the position of the sample revealed, that T_C was not reached during the experiment, which is displayed on the left side of figure 4.3.

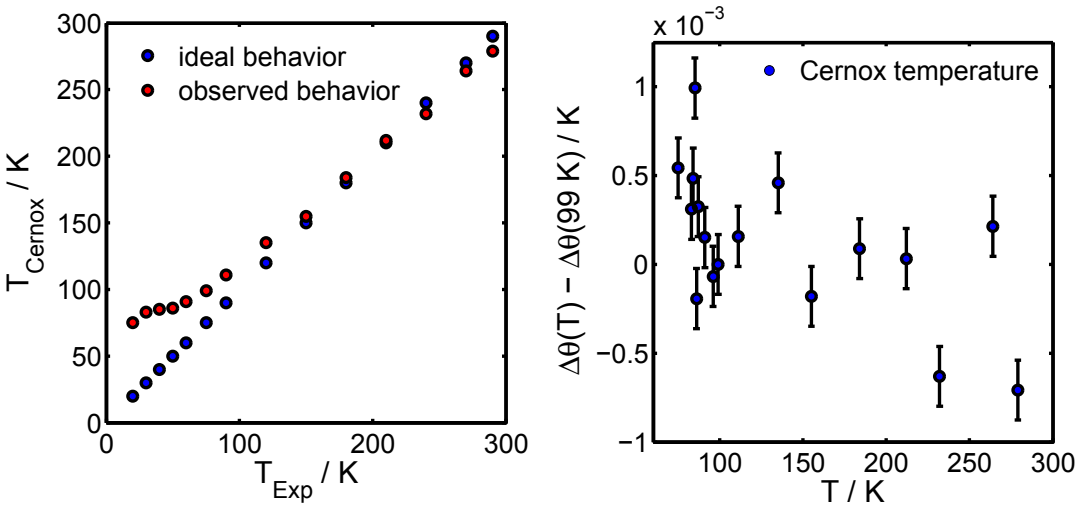

Figure 4.3: Left: Calibration of the sample temperature. The blue and red points represent an ideal temperature behavior, where the sample has the same temperature as the cold finger, and the measured temperature, respectively. The temperature displayed by the Cernox sensor differs significantly from the temperature of the cold finger. Right: Measured angular separation of GaAs and GaMnAs (004) Brag reflections of sample 61212A at BL9 at DELTA. The angular separation $\Delta\theta(99\,K)$ is used as a reference.

Although, the temperature measurement with a sensor like Cernox or Pt100 depends heavily on the quality of thermal contact to the sample, which is shown in section 4.4, it is highly unlikely that the sensor is up to 80 K off. Therefore, beside the shortcomings of the setup with respect to the sample alignment, the determination of the sample temperature was inconclusive.
All in all the CryoVac setup lacked the possibility to align the sample height in a $\theta = 2\theta = 0\,^\circ$ geometry, to cool the sample efficiently below T_C or yield a conclusive sample temperature, and limited the feasibility of the experiment to small θ-angles of about $14\,^\circ$ due to the stiff transfer tubes. Additionally, the θ-range was limited to $\pm 2\,^\circ$. The next section introduces an alternative setup eliminating these shortcomings by utilizing a cryostream cooler system.

4.3 Oxford 700 series cryostream cooler setup

To avoid the problems that occured using liquid helium as a cooling agent the GaMnAs sample 90127A with higher T_C of 110 K was investigated. Therefore, liquid nitrogen becomes an option as a refrigerant. Using the Oxford 700 Series cryostream cooler [Oxford14] entailed the advantage of decoupling the cooling unit from the sample stage eliminating the limitations in sample alignment and additional vibrations due to the stiff helium transfer tubes. The photon energy was then lowered to 15 keV resulting in a scattering angle of $2\theta = 34.006\,^\circ$ for the GaAs (004) reflection.

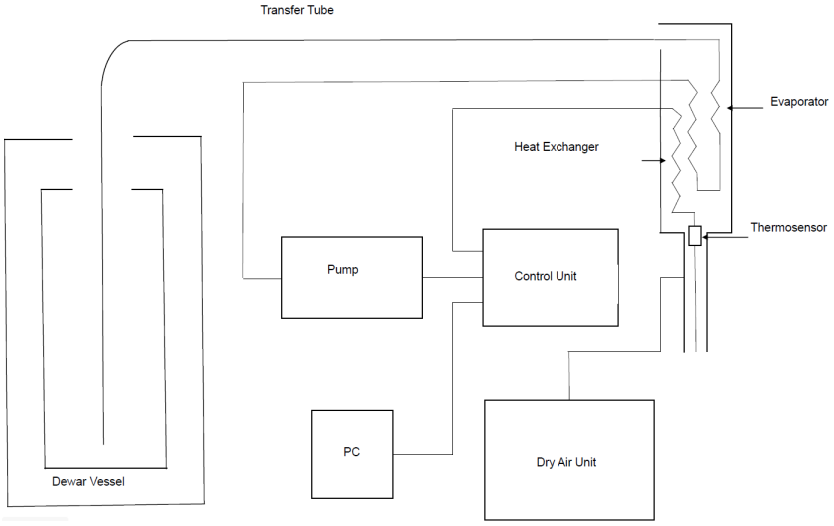

Figure 4.4: Schematic drawing of the Cryostream system. The system contains a Dewar vessel, pump, control unit, dry air unit, and the cryostream itself.

In principle the setup consists of a Dewar vessel to store the liquid nitrogen, the jet which blows the cold gas onto the sample in a laminar way and a pump to transport the cooling agent to the jet. A control unit, which can be operated by the beamline computer, monitors and regulates the temperature at the thermosensor and heat exchanger,

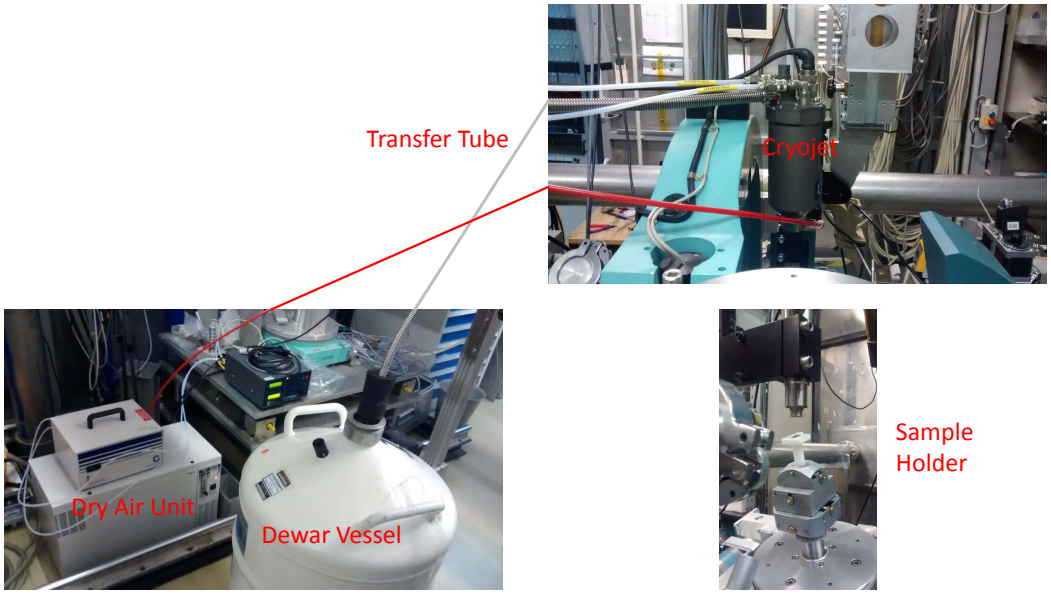

Figure 4.5: The cryojet setup at Beamline BL9 at DELTA. The Delrin sample holder is mounted on the diffractometer (bottom right). The cryojet (top right) cools the sample at a distance of about 2 cm. A small amount of ice can be seen at the sample holder. The nitrogen and dry air are delivered by the Dewar vessel and dry air unit (left), respectively.

respectively. The displayed temperature is calibrated to show the temperature at the sample position by using an interpolation on the basis of the nozzle temperature. Due to the encasing of the cold gas ray with dry air, the freezing of the jet's nozzle is prevented by shielding it from the humidity of the atmosphere. In order to prevent introducing temperatures from the atmosphere to the set temperature the evaporation of the liquid nitrogen occurs only at the jet's nozzle. A schematic overview of the cryostream system is displayed in figure 4.4. It is possible to run the cryostream cooler in a temperature range from 80 K to 500 K using variable volumetric flow rates resulting in a cool-down time to 100 K in about twenty minutes while ensuring a temperature accuracy of 0.1 K. The sample holder is made of Delrin to insulate the sample from the sample stage to avoid external heating and can be seen in figure 4.5. To ensure a good thermal conductivity without introducing additional strain, which can lead to aberrations, cryogenic high vacuum grease was used to fix the sample.

Results and discussion

The sample alignment with the cryostream setup was similar to the one described in 4.2. Without the rigid helium transfer tubes it was possible to align the sample height at $\theta = 2\theta = 0$ for each temperature.
Unfortunately, succeeding scans were not reproducible as can be seen in figure 4.6.

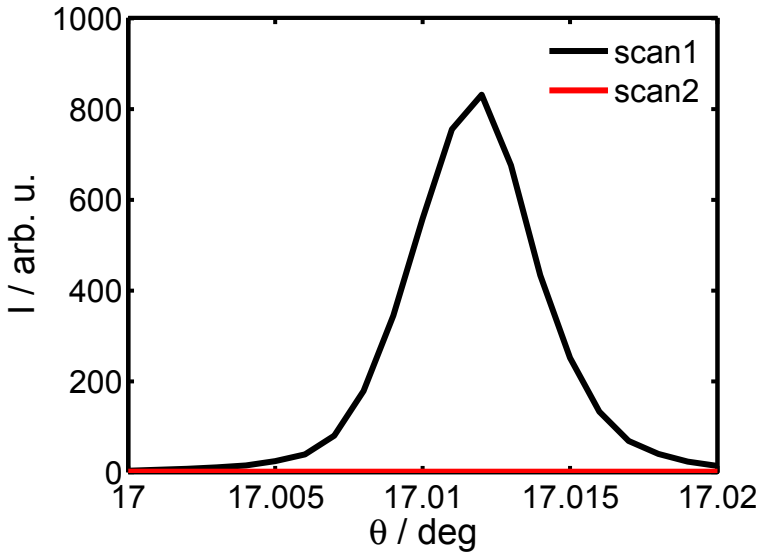

Figure 4.6: Two consecutively measured θ-scans. The first scan (black) shows the (004) Bragg reflection at the Bragg angle 17.014 °. The identical scan was then repeated (red) and no signal was detected.

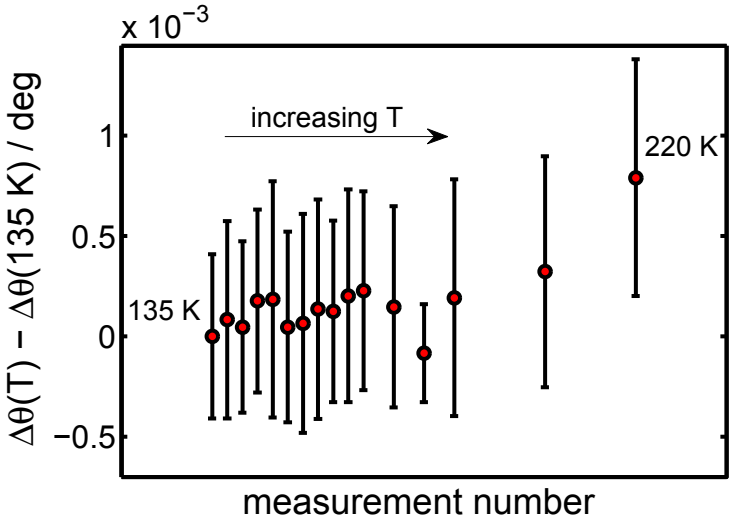

Figure 4.7: Measured angular separation of GaAs and GaMnAs (004) Bragg reflections of sample 90127A with the cryostream cooler setup. Since the sample temperature could not be measured accurately, the measurement number is displayed on the x-axis.

After changing to a sample holder made of aluminum the reproducibility was restored. While changing the sample holder a significantly lower amount of vacuum grease was used. Thus, it was not clear if the sample was not firmly fixed with the combination of dry air and vacuum grease or if the sample holder itself was the problem.

The investigated temperature range was chosen from 80 K to 220 K, where each temperature step was measured twice. The averaged angular separation is shown in figure 4.7. The displayed error bars correspond to the error of the averaged data.
The angular separation is one order of magnitude lower than the observed separation with thy CryoVac setup. This could be explained if the temperature displayed by the cryostream system did not concur with the sample temperature. This theory was further confirmed by temperature measurements utilizing a Pt100 temperature sensor and a Si wafer. The lowest temperature measured with the Delrin sample holder was about 85 K, while the distance from sample to nozzle was a few millimeters. The temperature reached with the aluminum wafer however, was about 135 K. The sample temperature measurement has the disadvantage that it cannot be performed during the diffraction experiments, because the Pt100 has to be placed directly into the cryostream on top of the sample. An additional arising difficulty is the thermal isolation of the Pt100 cables which is crucial for the determination of the exact sample temperature. In conclusion both the angular separation and the temperature measurements suggested that the sample temperature did not reach the Curie temperature and could not be measured precisely.
Although, the main goal was reached by eliminating the limitations of the CryoVac setup resulting from the transfer tubes, and therefore enabling a stable sample alignment and position, the problems with the regulation of the sample temperature still existed. The additional inability to determine the sample temperature during the experiments lead to a third setup with a continuous-flow cryostat.

4.4 The Oxford Instruments Optistat CF-2V continuous-flow setup

In a third experimental approach the continuous-flow Optistat CF-2V from Oxford Instruments [Oxford13c] was introduced to the Beamline BL9. The cryostat operates in a temperature range of 4.2 K - 500 K with a stability of 0.1 K. The cooling time from ambient conditions to 4.2 K is shorter than ten minutes when operated with liquid helium and about 20 minutes with nitrogen. Pumping the transfer tube with a turbomolecular pump accelerates this process. The helium consumption while cooling down and at 4.2 K is smaller than 1.3 l and 0.45 l, respectively.
The cryogen is supplied from the storage vessel via a flexible, L-shaped, insulated transfer tube. An additional pump is used to pull the cooling agent from the Dewar to the sample space. The flow rate can be controlled via a flow meter, which is calibrated for helium gas. The sample is mounted on a L-shaped, copper sample holder connected to the heat exchanger located in vacuum. The heat exchanger is coupled to a thermometer and a heater, which can be used in combination with the Mercury temperature controller [Oxford13b] to regulate the temperature of the sample. Additionally, two Pt100 temperature sensors are introduced directly to the sample holder, which can be used to measure the temperature in close vicinity to the sample. An additional outer vacuum chamber (OVC), pumped via a turbomolecular pump, shields the sample from

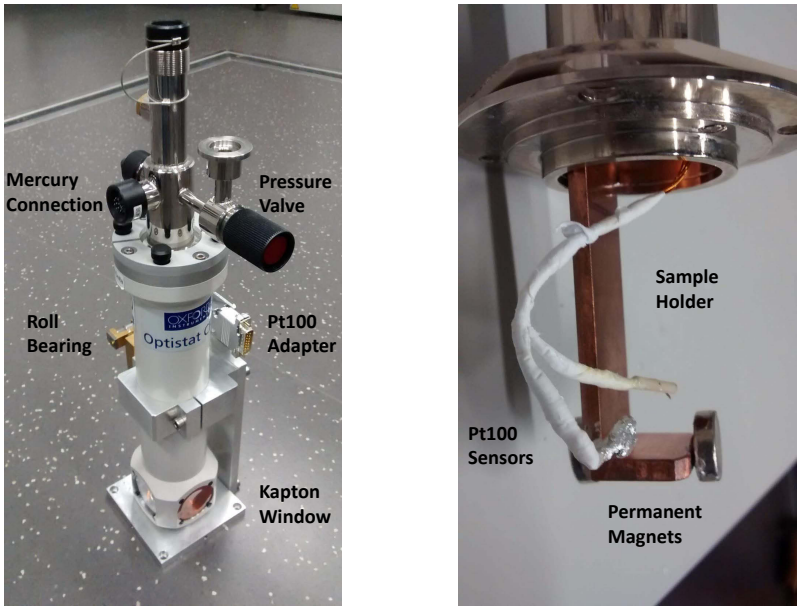

Figure 4.8: Left: The used Optistat CF-2V mounted on the adapter plate for use at the beamline BL9. The Pt100 sensors can be read out via a Lake Shore temperature controller. The roll bearing ensures an excellent steadiness on the one hand and allows to move the sample position along the z-axis of the diffractometer on the other. Right: The sample holder is made from copper to optimize the cooling of the sample. Two additional Pt100 sensors are installed in order to measure the sample temperature in close vicinity. Additionally, a magnetic field of about 170 mT is introduced at the samples position by two permanent magnets.

the ambient temperature surroundings. The sample space can be accessed by light via four windows, two of which are made of Kapton. Figure 4.8 shows the used Optistat CF-2V. To ensure a defined magnetization axis two permanent magnets were glued to the sample holder resulting in a magnetic field parallel to the $[1\bar{1}0]$ direction, if the incoming x-ray beam is scattered along the [110] direction. The field was determined to 170 mT utilizing a hall effect sensor.
While adapting the cryostat to the diffractometer of beamline BL9 several problems arose. Due to the arrangement on site it is not possible to put the helium transfer tube into the Dewar vessel and the cryostat at the same time. If nitrogen was used as a cooling agent, the transfer tube does not have to be firmly fixed into the Dewar, which leads to a manageable configuration at the beamline. Therefore, the temperature range for this setup is 80 K - 500 K. The investigated temperature range however, was 80 K - 160 K. In principal, it is possible to operate this setup with liquid helium as a cooling agent leading to a temperature range of 4 K - 500 K. In order to realize this in the future some improvements regarding the helium transfer have to be made at BL9.
First measurements also revealed an impact of the helium transfer tube on the measurements of the truncation rods, which can be seen in figure 4.9. The data presented

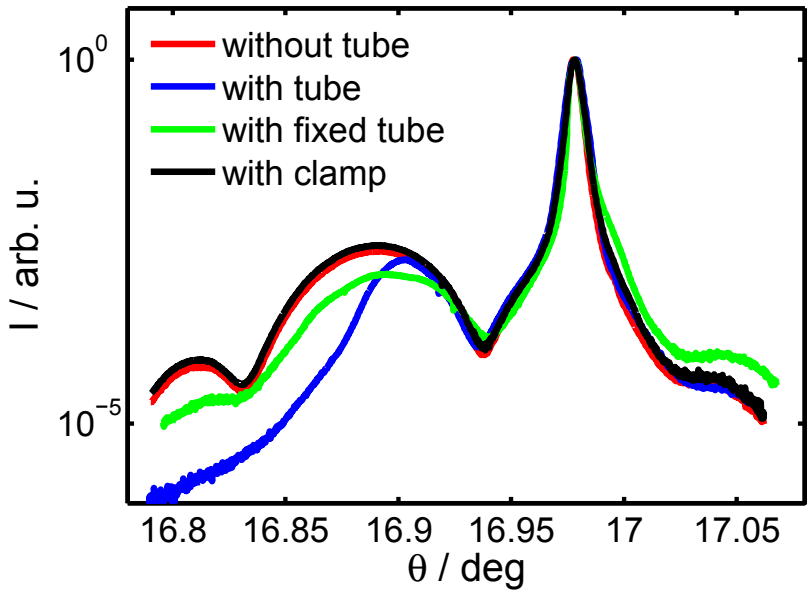

Figure 4.9: Four consecutively measured (004) Bragg reflections at 295 K. The data presented in red were measured without the helium transfer tube attached to the cryostat. Putting the helium transfer tube hanging loosely in the Dewar vessel into the cryostat leads to the blue data. The introduced vibrations of the transfer tube rattling against a construction stray at the beamline lead to a loss of resolution. In order to reduce those vibrations the transfer tube was fixed with zip ties to avoid contact with the stray. Though the resolution is improved, it is still not satisfying (green). In a last step the cryostat itself is additionally fixed with a clamp to the diffractometer, which leads to the results measured without the transfer tube (black).

in red show the (004) Bragg reflections of GaMnAs and GaAs at 295 K. The second scan shown in blue was taken after introducing the transfer tube into the cryostat. The loss of resolution can be ascribed to vibrations introduced by the contact of the tube with an constructive stray at the beamline while altering the incident angle. Though the resolution could be improved by decoupling the transfer tube from the stray with zip ties, the result did not reach the resolution of the first run (green). In a last step the cryostat was firmly fixed to the diffractometer utilizing a clamp (black), which is depicted in figure 4.10. On the one hand the reproducibility of consecutively measured scans was restored. On the other hand however, the clamp does not allow the movement of the sample along the z-direction, which is needed to adjust the sample in height. As a result the clamp was loosened at the $\theta = 2\theta = 0\,^\circ$ geometry to perform z-scans and again fixed after. Due to the high angular sensibility of the experiment the loosing and fixing of the clamp led to alignment errors that needed to be corrected.
A solution for this problem was the adaption of ball bearings to the cryostat holder in combination with a plate, which can be screwed to the diffractometer. This can be seen on the right side of figure 4.10. Hereby the cryostat is stabilized by the transfer tube pulling it against the plate while still enabling movement along the z-direction.

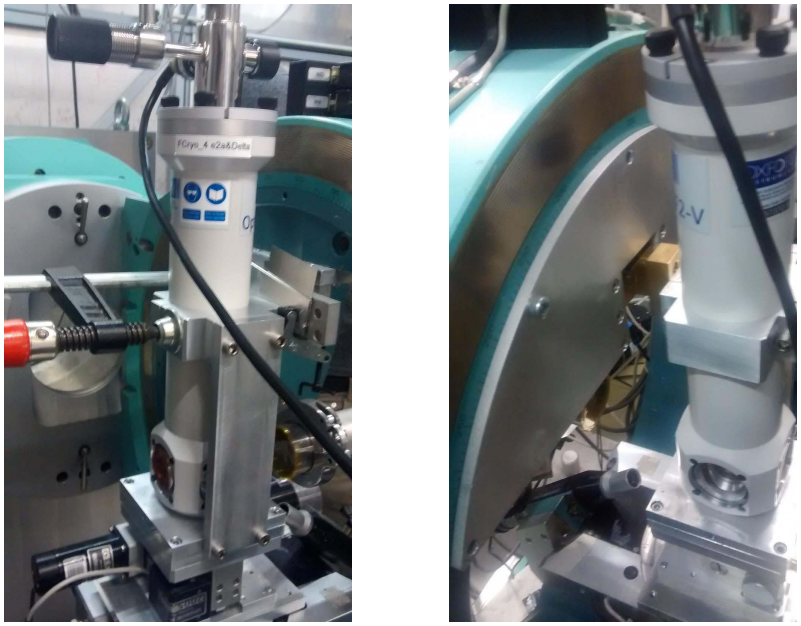

Figure 4.10: Two different ways to firmly mount the cryostat to the diffractometer at beamline BL9. On the left the cryostat is fixed with a clamp in order to protect it against vibrations. The disadvantage of this setup lies in the inability to move the cryostat along the z-direction. This issue is solved by utilizing ball bearings, which can be seen on the right side.

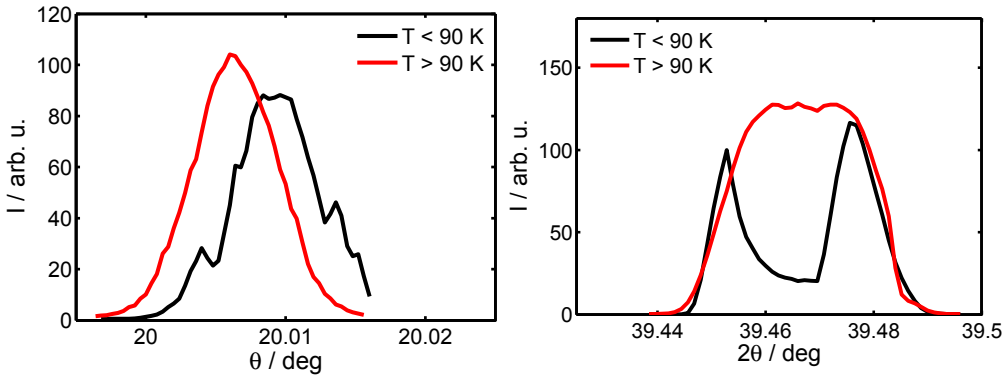

Figure 4.11: Unusual spikes and dips in the intensity during θ- and 2θ-scans in the temperature range from 80 K - 90 K illustrated in black. The red curves show ordinary scans at higher temperatures.

Another problem occurred at cold temperatures around 80 K to 90 K. Alignment scans revealed unusual spikes and dips in the intensity as can be seen in figure 4.11. These irregularities may be caused by the collected liquid in the sample space boiling irregularly, which is common for temperatures below 90 K [Oxford13a].
After the stable sample position and alignment were realized, it had to be ensured that the indicated temperature by the Mercury temperature controller corresponds to the sample temperature, which is shown in the next section.

Sample temperature calibration

As mentioned above, two additional Pt100 temperature sensors were introduced into the sample space. To determine the temperature of the sample three temperature series within the range of 80 K to 145 K in steps of 5 K and one from 80 to 270 K in 10 K steps were performed. One Pt100 was put directly on a Si wafer with low temperature vacuum grease to optimize the thermal contact. The corresponding data are presented in figure 4.12. After each temperature series the Pt100 sensor was readjusted, in order to reach an excellent thermal contact to the sample. After two minutes the temperature had reached its equilibrium and the value was noted before starting the next temperature step.
Linear fits were performed for each temperature series. The slopes were determined as follows; red: 0.78 ± 0.02, blue: 0.95 ± 0.01, green: 0.98 ± 0.01, and cyan: 0.96 ± 0.01.

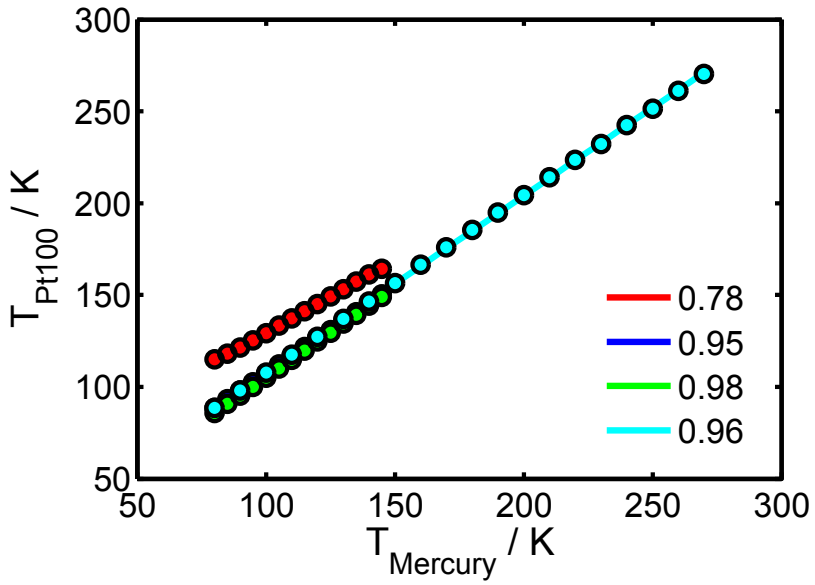

Figure 4.12: Calibration of the sample temperature for the Optistat CF-2V setup. The slopes of the four corresponding linear fits are displayed in the legend. The Pt100 thermosensor was adjusted and fixed to the sample after every temperature series. The time until the temperature reached its equilibrium was two minutes. It can be seen that the measured temperature of the Pt100 sensor correlates to the quality of the thermal contact to the sample.

The data revealed that the displayed temperature depends heavily on the quality of the thermal contact to the sample. However, with excellent thermal contact in the case of the measurement presented in green, both sensors yielded almost concurring values within the estimated errors. Therefore, the temperatures indicated by the Mercury temperature controller have been proven to be reliable and were used throughout this thesis. Since this setup combining the Optistat CF-2V with the ball bearings provides both, excellent stability and exact sample temperature determination, it was used during the conducted experiments at BL9 presented within this thesis. The measurements at BL9 at DELTA were carried out at a temperature range from 85 K - 160 K sampling in sixteen temperature steps with an increment of 5 K in the vicinity of 110 K, the Curie temperature of sample 90127A and an increment of 10 K otherwise. The scanning range was segmented in three parts varying in increment and scanning time. The complete scan including the sample alignment took about 90 minutes. Despite T_C of sample 61212A could not be reached, the sample was used as a reference. The results obtained with this setup are presented and discussed in chapter 5.

4.5 The XMaS beamline BM28 at ESRF

In order to investigate the effect of spontaneous magnatostriction when passing T_C for both samples XRD experiments were conducted at the XMaS (X-ray Magnetic Scattering) beamline at ESRF [Paul95]. The XMaS beamline located at bending magnet 28 is one of the fifty beamlines at ESRF. A wide range of experimental techniques such as single crystal diffraction, spectroscopy, small angle scattering, resonant elastic x-ray scattering or grazing incidence reflectivity are available. Additionally, it uniquely combines the instrumentation for magnetic and high-resolution single-crystal diffraction. Both polychromatic and monochromatic energies between 2.4 keV and 15 keV can be utilized, with a critical energy of the bending magnet of 9.8 keV and an energy resolution on the order of $dE/E = 10^{-4}$. The typical photon flux at 10 keV is $5 \cdot 10^{12}$ photons/s in a focal spot size of 0.8 mm $\cdot$ 0.3 mm [Brown01]. The beam can be monochromatized by a water-cooled Si (111) double crystal. Further focusing and conditioning of the beam is realized by several mirrors, phase-plates, and an in vacuum polarization analyzer. Figure 4.13 shows a schematic diagram of the XMaS beamline. An eleven-axis Huber diffractometer ensures the feasibility of both horizontal and vertical scattering geometries. Different sample environments facilitate a temperature range from 1 K to 1200 K. Magnetic fields of 0.1 T, 1 T, and 4 T can be applied by an in-vacuum electromagnet, an electromagnet, and a superconducting magnet, respectively. A variety of detectors is available e.g. scintillaton detectors, avalanche photodiodes, a MAR165 CCD or 2D pixel detectors like Pilatus3 300K or Maxipix.
A focused beam with a photon energy of 15 keV and spot size of 0.8 mm $\cdot$ 0.5 mm was utilized for the conducted experiments. The scattered intensity was detected by a 2D Maxipix detector. The sample was cooled by an ARS DE202 G closed cycle cryocooler [ARS17]. A silicon diode temperature sensor is used in combination with a

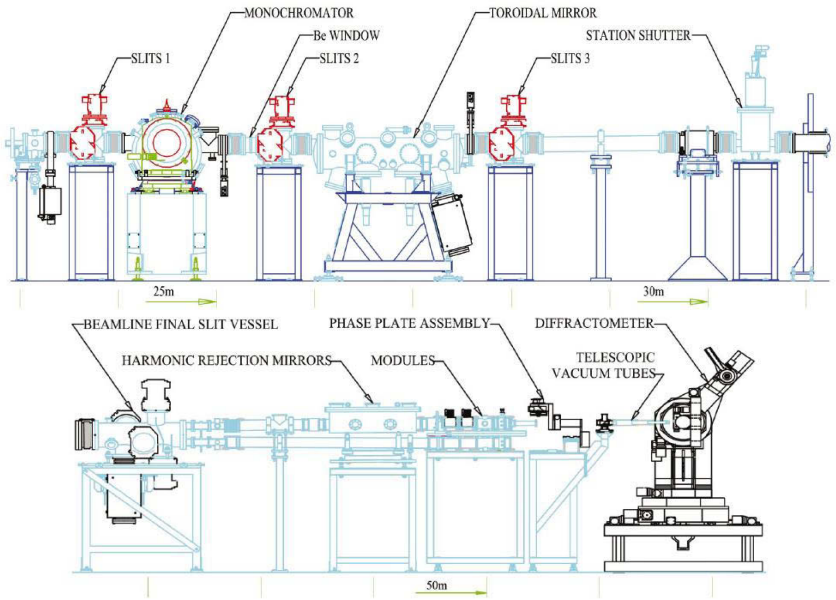

Figure 4.13: Schematic diagram of the XMaS beamline. Top: After passing a first slit the beam is monochromized by a water-cooled Si (111) double crystal. The following focusing toroidal mirror is rhodium-coated and responsible for the energy cut-off at 15 keV. Bottom: The focused and monochromized beam travels through the upper beam pipe while the lower beam pipe carries the white or unfocused monochromized beam. After passing a variety of attenuators, beam monitors, and slits the beam hits the phase plate assembly, where the polarization of the beam can be modulated. An additional telescopic vacuum tube minimizes the beams contamination to air. Reproduced with permission of the International Union of Crystallography from Brown, S. D. et al., The XMaS beamline at ESRF: instrumental developments and high resolution diffraction studies, J. Synchroton Rad., 1172-1181 Copyright (2001).

Lakeshore model 340 [LakeShore09] to measure and control the sample temperature. Here, the pump of the closed cycle cryocooler did not introduce vibrations to the sample, which would interfere with the measurement of the truncation rods. In order to investigate the impact of the ferromagnetic ordering due to the passing of T_C no magnetic field was applied. A temperature range from 30 K to 180 K was sampled in 23 steps for both samples. Each measurement scan was fragmented in three parts varying in increment and attenuator strength. One complete scan including sample alignment took approximately 50 minutes. The data attained at the ESRF are presented and discussed in chapter 5. Figure 4.14 shows a generic scan at 30 K. A scan measured at DELTA at 100 K is included. The significantly larger q range at the ESRF was possible due to the higher photon flux. Whereas the reproducibility of the scans was better at DELTA which will also be discussed in Chapter 5.

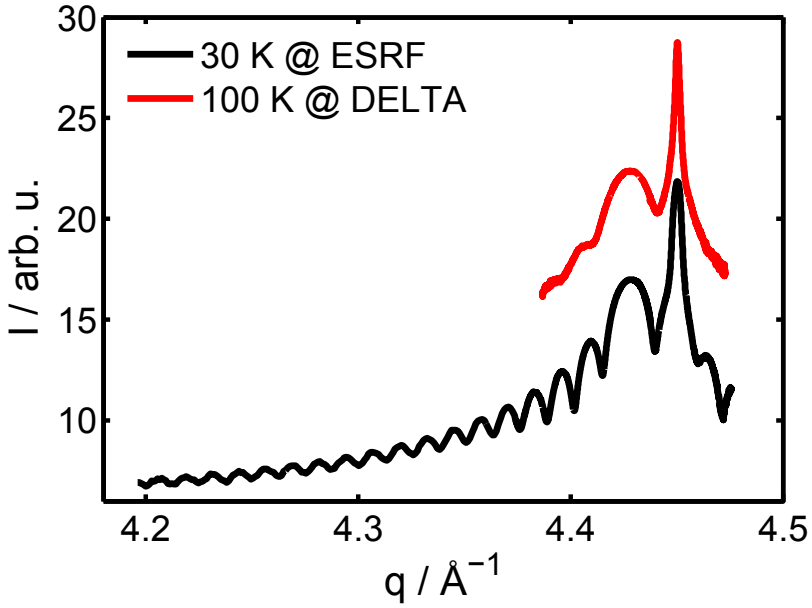

Figure 4.14: Generic measured (004) GaMnAs Bragg reflections at 30 K and 100 K taken at the XMaS beamline at ESRF and BL9 at DELTA, respectively. The measured diffraction pattern are shifted vertically.

Chapter 5

XRD study of the impact of magnetostriction on GaMnAs thin film lattices

As mentioned before, XRD is the ideal tool to investigate small structural changes of divers materials, including semiconductors, on an atomic level. In fact, XRD fulfills a wide range of applications in the semiconductor device manufacturing process, like measuring the crystal orientation of single crystals or analyzing epitaxially-grown thin films [Bowen06].
Also, a variety of XRD experiments have been performed on GaMnAs not only revealing the crystal structure but contributing to the understanding of ferromagnetism in such systems. For example, the lattice constant of GaMnAs has been investigated in dependence on Mn concentrations up to 10 % [Sadowski00, Sadowski01, Schott03]. Furthermore, the investigation of the effect of annealing on the layer growth has yielded that the concentration of interstitial Mn is reduced, while the density of randomly distributed Mn atoms in the surface layer increases [Holy06]. This has been explained by the outdiffusion of interstitial Mn to the surface layer. The densities of the Mn distribution and differences for two different interstitial sites have been determined utilizing anomalous XRD with a photon energy near the Mn K-edge [Holy95]. Gallardo-Hernandez et al. combined secondary ion mass spectroscopy (SIMS) with XRD measurements in order to detect depth profiles of the Mn composition for self-assembled, MBE grown multilayers [Gallardo-Hernandez13].
In this thesis, the impact of magnetostriction on the crystal lattice of GaMnAs thin films was investigated via XRD, which is presented in the following. At first, the data treatment and refinement is discussed. Here, the focus lies on separating the magnetostriction from the thermal effect on the lattice. Afterwards, the experimental study of two GaMnAs samples with magnetic transition temperatures of 110 K and 50 K is presented. The samples were investigated in a temperature range from 30 K to 180 K, utilizing either nitrogen or helium as a refrigerant.

5.1 Data treatment and refinement

In the following, the data handling is described. The data treatment is quite similar for the experiments conducted at different beamlines where a Pilatus 100K and a Maxipix 2D were used to detect the diffraction patterns. In contrast to image plate detectors where the whole diffraction pattern can be detected with one exposure, one diffraction image for each angular step has to be taken with 2D pixel detectors. A diffraction pattern of one scan is obtained by integrating over all pixels within the ROI for each 2θ value. Figure 5.1 shows two collected Pilatus 100K images. On the left side an image taken during a 2θ-scan is displayed. The Pilatus image is used to locate the direct x-ray beam on the detector and set the ROI. The right side shows a diffraction image obtained at the maximum of the GaAs (004) Bragg reflection. Since the x-ray beam is focused on

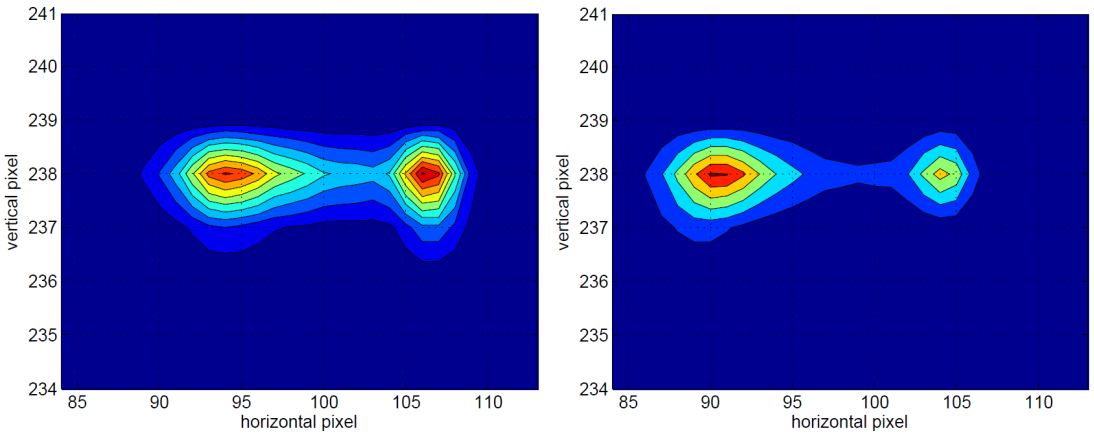

Figure 5.1: Two diffraction images taken with the Pilatus 100K at BL9. The left side shows an image taken during a 2θ-scan, which is used to determine the position of the x-ray beam on the detector and set the ROI. The right side shows an image taken at the maximum of the GaAs (004) Bragg reflection.

The differences $\Delta\theta = \theta_{\mathrm{GaAs}} - \theta_{\mathrm{GaMnAs}}$ were investigated in order to separate the magnetostriction effect on the lattice from the thermal effect. Where θ_{GaAs} and θ_{GaMnAs} are the positions of the (004) GaAs and GaMnAs reflections, respectively. The positions were determined by fitting Gaussian functions

$$g(\theta) = a \cdot \mathrm{e}^{-((\theta-b)/c)^2} \tag{5.1}$$

to both (004) Bragg reflections. In order to reduce possible error sources every diffraction pattern was shifted resulting in the same position of the GaAs reflection. The shift $\Delta\theta_{\mathrm{s}}$ was determined by minimizing the expression

$$\Psi^2 = \sum_{\theta} [I(\theta + \Delta\theta'_{\mathrm{s}}) - I_{\mathrm{ref}}(\theta)]^2, \tag{5.2}$$

where I_{ref} is an intensity pattern used as a reference and $\Delta\theta'_{\mathrm{s}}$ is the shift, which was probed on a range of $\pm 0.02\,^{\circ}$ of the reference maximum's position. The minimum of Ψ^2 was then used to shift all diffraction patterns to have the same θ-value for the (004) GaAs reflection. This process is depicted in figure 5.2. Therefore, the GaAs reflection had to be fitted only once. The converged fits deliver the diffraction peak positions $b = \theta_{\mathrm{GaAs,GaMnAs}}$. The corresponding error bars were calculated in two different ways; first, the errors estimated by the fitting routine were used to perform the propagation of uncertainties. The second variant is the error arising due to the averaging over multiple measurements. Both error bars were compared and the larger error is displayed throughout this chapter. In a last step the peak positions were converted into the wave vector transfer q, since it enables the comparison of all experiments, which were conducted at different x-ray energies.
In each figure that presents measured or fitted data in dependency on the temperature, the temperature range below the Curie temperature is indicated by a grey background.

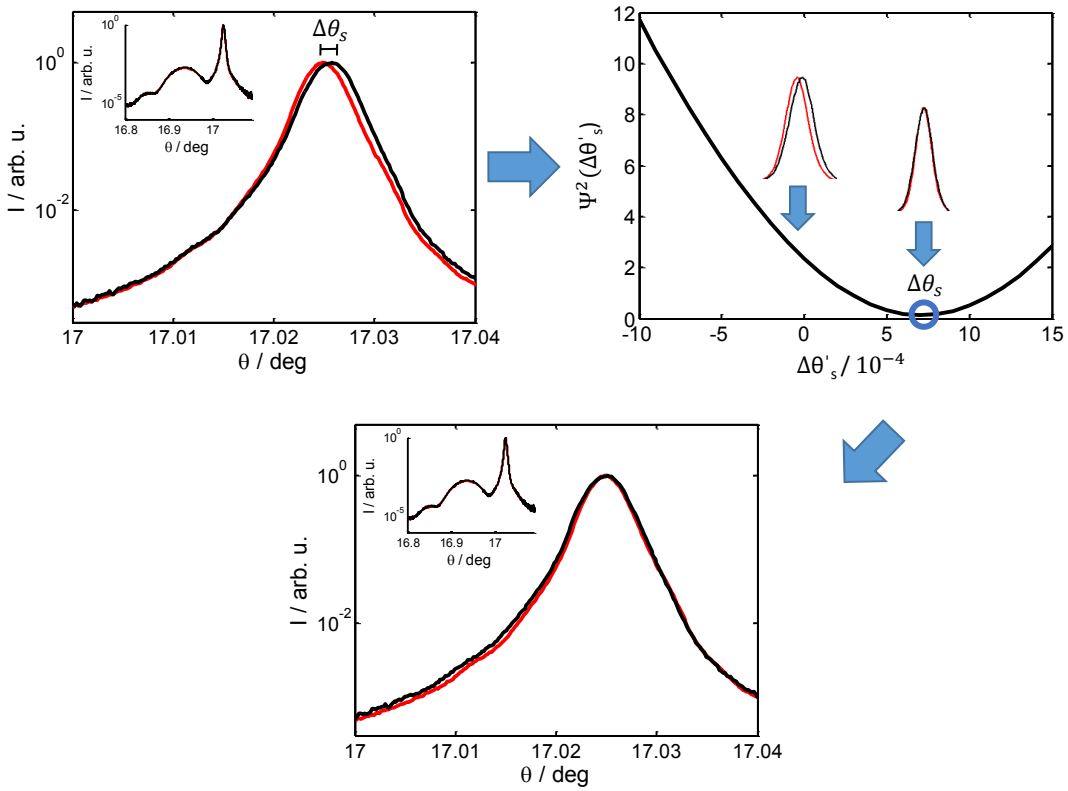

Figure 5.2: Shifting process of the diffraction patterns exemplary shown for diffraction patterns taken of sample 90127A at BL9. On the left upper side two GaAs (004) Bragg reflections with a shift $\Delta\theta_{\mathrm{s}}$ are presented. The inset shows the whole diffraction pattern. The upper right side displays the minimization of the function Ψ^2. This was done by shifting the diffraction patterns against each other in dependence of the shift $\Delta\theta'_{\mathrm{s}}$. The bottom part shows the (004) GaAs Bragg reflections after the determined shift was applied.

5.2 The separation of the (004) GaAs and GaMnAs Bragg reflections

The effect of magnetostriction on GaMnAs nanometer-thin films has been investigated by nanomechenical measurements, where a magnetic field is applied to the sample resulting in magnetoelastical stretching and compression. The corresponding mechanical resonance frequency variations provide a measure of magnetostriction. The magnetostriction constants have been found to be on the order of $1 \cdot 10^{-5}$ at 4.2 K [Masmanidis05].
In order to get further insights and observe the induced magnetostriction effect directly on the crystal lattice XRD experiments were performed at beamline BL9 at DELTA. A magnetic field of 170 mT was applied parallel to the $[1\bar{1}0]$ direction of the sample which resulted in a defined direction of saturated magnetization perpendicular to the x-ray beam. As discussed in section 4.4 the Optistat CF-2V was firmly fixed to the diffractometer via either clamp or ball bearings. The setup using the clamp for stabilization was utilized to investigate sample 90127A. Three temperature series in the range of 80 K - 295 K were conducted. The photon energy was set to 15 keV. The measured separation on the momentum transfer scale $\Delta q(T) = q_{\mathrm{GaAs}}(T) - q_{\mathrm{GaMnAs}}(T)$ referenced to the separation at 120 K is presented in figure 5.3. The displayed error bars are the statistical ones determined by the averaging of the single measurements. If only one scan was performed for a given temperature, the largest arising error estimated within the temperature series is assumed.

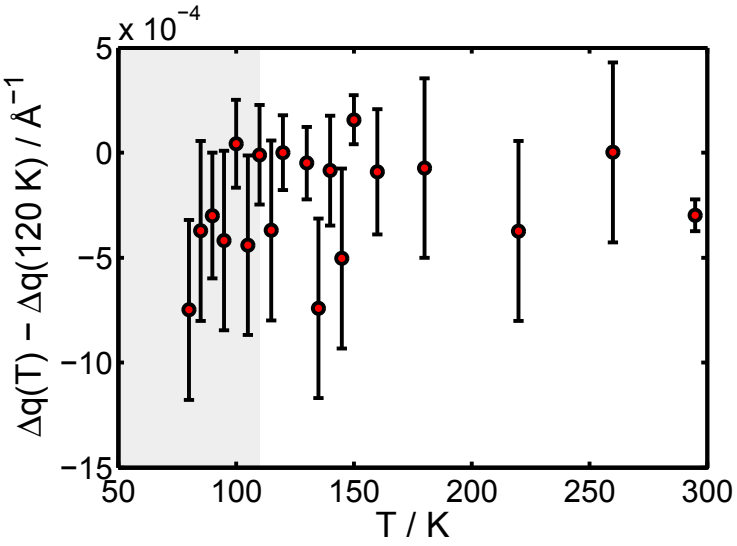

Figure 5.3: Separation of the GaAs and GaMnAs (004) Bragg reflections of the sample 90127A measured at BL9 with the Optistat setup utilizing the clamp for stabilization.

The disadvantage of the clamp setup is that the clamp has to be loosed in order to adjust the sample in height. The loosing and fixing of the clamp slightly modifies the position of the Optistat and therefore the sample. Since the XRD technique is highly

sensitive to small changes in angle and position of the sample, these small variations have to be corrected, which is error-prone. This was avoided by using the ball bearing setup.
The focus of this chapter lies on the data measured with this setup, because of the good reproducibility of the measured diffraction patterns. Two beamtimes were dedicated to the XRD measurements utilizing photon energies of 13 keV and 15 keV. The probed temperature range was 80 K - 160 K for both samples. The whole scanning range reached from $\Delta\theta_{\text{start}} = -0.5\,^\circ$ to $\Delta\theta_{\text{end}} = 0.18\,^\circ$ relative to the (004) GaAs Bragg reflection at $\theta = 19.717\,^\circ$ and $\theta = 17.002\,^\circ$ for 13 keV and 15 keV, respectively. The scan was subdivided into three scanning ranges distinguished in increment and scanning time. The q-separation for both samples at 15 keV is presented in figure 5.4. The displayed error bars in figure 5.4 were calculated according to the averaging process over all scans for each temperature for each sample.
Comparing the estimated errors resulting with the ball bearing setup to the ones given with the clamp reveals that the errors made with the clamp are nearly three times larger. This origins most likely in the fastening and loosing of the clamp for adjustment purposes as discussed above. These findings support the decision to use the Optistat setup with the ball bearing stabilization.
The q-separation data is discussed considering two different approaches; first, it is assumed that there is no effect on the lattice structure due to magnetostriction. Here, a linear behavior of $\Delta q(T) - \Delta q(120\,\text{K})$ is supposed resulting in a linear fit to the data. This approach is displayed on the top-left and bottom part of figure 5.4. The slopes for samples 90127A and 61212A were determined to $(2.5 \pm 1.3) \cdot 10^{-6}\,(\text{Å K})^{-1}$ and $(1.9 \pm 1.9) \cdot 10^{-6}\,(\text{Å K})^{-1}$, respectively. Both slopes lie on the same order of magnitude and concur within the estimated errors. However, as the thermal lattice expansion of GaAs and GaMnAs can be assumed to be almost the same [Qi10], the fit is expected to provide a constant value.
The second approach assumes a non-linear change of the lattice constant due to the second-order phase transition at T_C. For this purpose, three model functions were used to describe the separation of both (004) Bragg reflections on the momentum transfer scale.

$$t(T) = k_1 \cdot \tanh(k_2 \cdot T) + k_3 \tag{5.3}$$

is a tanh-function, which is used to model a continuous transition at T_C.

$$s(T) = \begin{cases} k_4 \cdot T + k_5 & T < T_\text{C} \\ k_6 \cdot T + k_7 & T > T_\text{C} \end{cases} \tag{5.4}$$

assumes two different linear functions above and below T_C resulting in a discontinuity.

$$l(T) = k_8 \cdot \tanh(k_9 \cdot T) + k_{10} \cdot T + k_{11} \tag{5.5}$$

is a linear combination of a tanh-function and a linear function. $l(T)$ therefore, combines the two approaches, allowing both a continuous transition at T_C and no effect of magnetostriction.

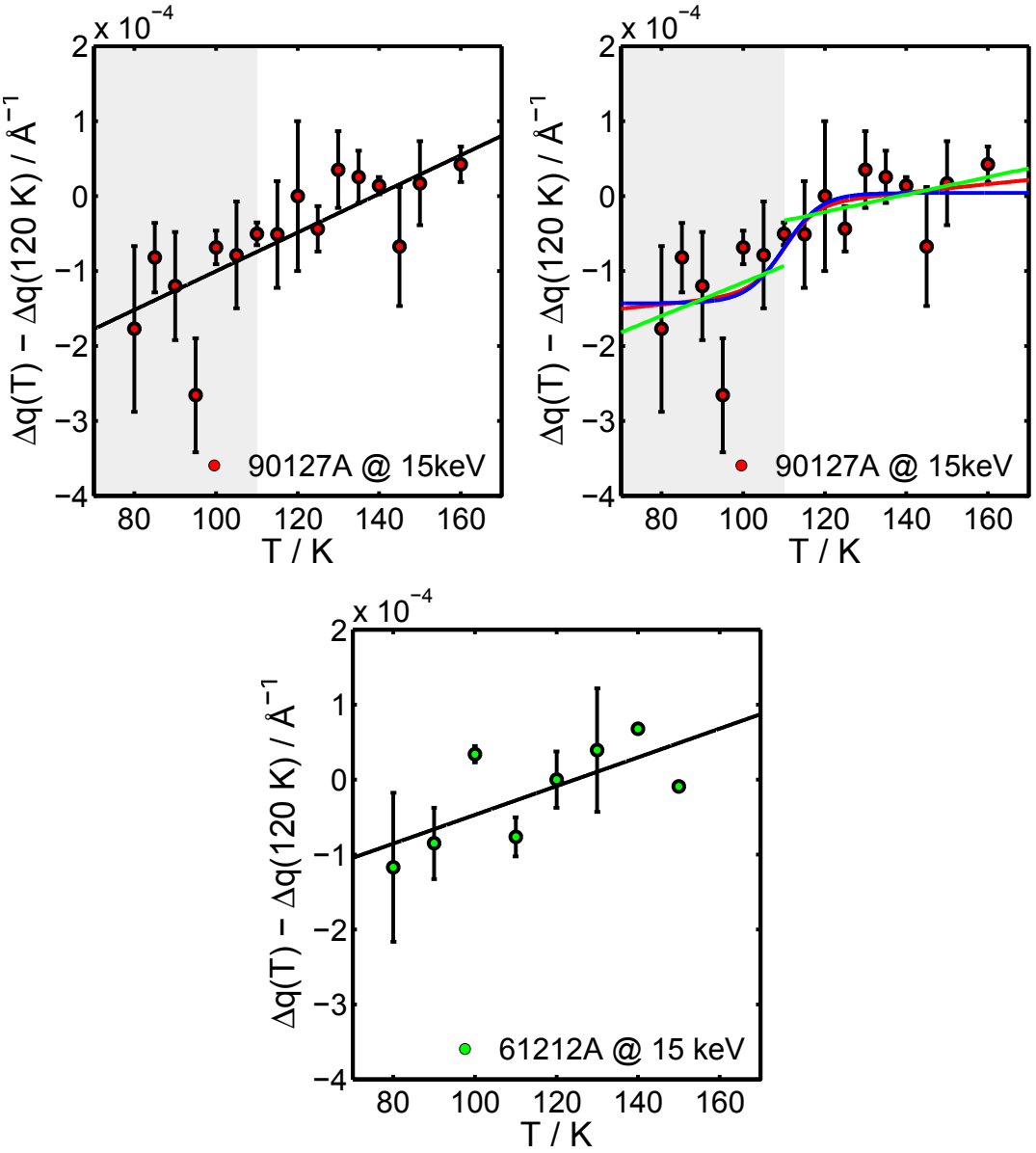

Figure 5.4: Top: q-separation of sample 90127A measured at BL9. Left: The change in $\Delta q(T) - \Delta q(120\,\mathrm{K})$ is assumed to show a linear behavior. The black line corresponds to a linear fit. Right: The change in $\Delta q(T) - \Delta q(120\,\mathrm{K})$ is assumed to show a non-linear shift due to the passing of T_C, which is set to the measured value of 110 K. The red, blue, and green lines correspond to fits to the functions $l(T)$, $t(T)$, and $s(T)$, respectively (see text). Bottom: q-separation of sample 61212A measured at BL9. The black line corresponds to a linear fit to the data.

The application of all three model functions to analyze $\Delta q(T) - \Delta q(120\,\mathrm{K})$ of sample 90127A is shown on the top-right part of figure 5.4. The red, blue, and green lines correspond to $l(T)$, $t(T)$, and $s(T)$, respectively. Both the red and blue lines show a

similar behavior with a continuous transition at T_C. The change in $\Delta q(T) - \Delta q(120\,\mathrm{K})$ at T_C lies on the order of $\Delta q(T_C) = (1.3 \pm 0.2) \cdot 10^{-4}\text{Å}^{-1}$ given by the averaging over the three changes determined by the model functions. Additionally, $s(T)$ shows a discontinuity and indicates different slopes below and above T_C. This approach was not applied to sample 61212A, since T_C was not reached in the experiments performed at DELTA.

The data of the second DELTA experiment conducted at 13 keV is presented in figure 5.5. The top-right part shows the three model functions applied to the separation data of sample 90127A. The red, blue, and green lines correspond to fits according to $l(T)$, $t(T)$, and $s(T)$, respectively. Both the red and blue lines suggest a continuous transition in the vicinity of T_C on the order of $\Delta q(T_C) = (1.5 \pm 0.3) \cdot 10^{-4}\text{Å}^{-1}$, which is in very good agreement with the results obtained at 15 keV. A different behavior above and below T_C is also indicated by the green lines.

The top-left and bottom part illustrate the linear approach to the separation data. The slopes of the solid black lines are $(0.8 \pm 2.2) \cdot 10^{-6}\,(\text{ÅK})^{-1}$ and $(2.1 \pm 1.2) \cdot 10^{-6}\,(\text{ÅK})^{-1}$ for samples 90127A and 61212A, respectively. These slopes are similar to the slopes at 15 keV within the estimated errors. Two linear fits were performed on the 61212A data; the black dashed line is a linear fit over the whole temperature range yielding a slope of $(5.0 \pm 1.8) \cdot 10^{-6}\,(\text{ÅK})^{-1}$. The black solid line corresponds to a linear fit to the data for $T > 100\,\mathrm{K}$. The strong deviation of the data below 95 K can possibly be explained by an systematic error but could not be clarified finally. In order to investigate the impact of magnetostriction on a larger temperature range, especially at lower temperatures covering the magnetic phase transition of sample 61212A, liquid helium as a cooling agent is mandatory. This kind of experiment was possible at the ESRF.

The XMaS beamline located at BM28 of the ESRF offers the possibility to investigate both samples in a temperature range of 30 K - 180 K. No additional magnetic field was applied to investigate the effect of the spontaneous magnetostriction. Three temperature series were measured for each sample. The whole temperature range was sampled in 23 steps. The photon energy was set to 15 keV. The whole scanning range reached from $\Delta\theta_{\text{start}} = -2\,^\circ$ to $\Delta\theta_{\text{end}} = 0.2\,^\circ$ relative to the (004) GaAs Bragg reflection at $\theta = 17.002\,^\circ$. It was possible to detect a much wider scanning range at the ESRF compared to DELTA, due to the excellent x-ray beam and high photon flux. The scan was subdivided into three scanning ranges distinguished in increment and attenuator.

The $\Delta q(T) - \Delta q(120\,\mathrm{K})$ data measured at BM28 is shown in figure 5.6 for both samples. The left side illustrates the linear approach to the data for samples 90127A and 61212A on the top and bottom, respectively. The black lines correspond to linear fits yielding slopes of $(1.3 \pm 1.0) \cdot 10^{-6}\,(\text{ÅK})^{-1}$ (90127A) and $(1.5 \pm 0.5) \cdot 10^{-6}\,(\text{ÅK})^{-1}$ (61212A), which concur within the estimated errors with the results of the DELTA experiment.

The top-right side shows the separation of both (004) Bragg reflections of sample 90127A including fits in red, blue, and green corresponding to the model functions $l(T)$, $t(T)$, and $s(T)$, respectively. All three model functions indicate a discontinuity at T_C. The change in $\Delta q(T) - \Delta q(120\,\mathrm{K})$ lies on the order of $\Delta q(T_C) = (0.9 \pm 0.4) \cdot 10^{-4}\text{Å}^{-1}$. $\Delta q(T) - \Delta q(120\,\mathrm{K})$ of sample 61212A is depicted on the bottom-right part of figure 5.6 displaying the same fits as discussed for sample 90127A. The red and green lines suggest

linear behavior below and above T_C with a discontinuity. The blue line indicates a broad continuous transition in the vicinity of T_C, but does not seem to model the data well.

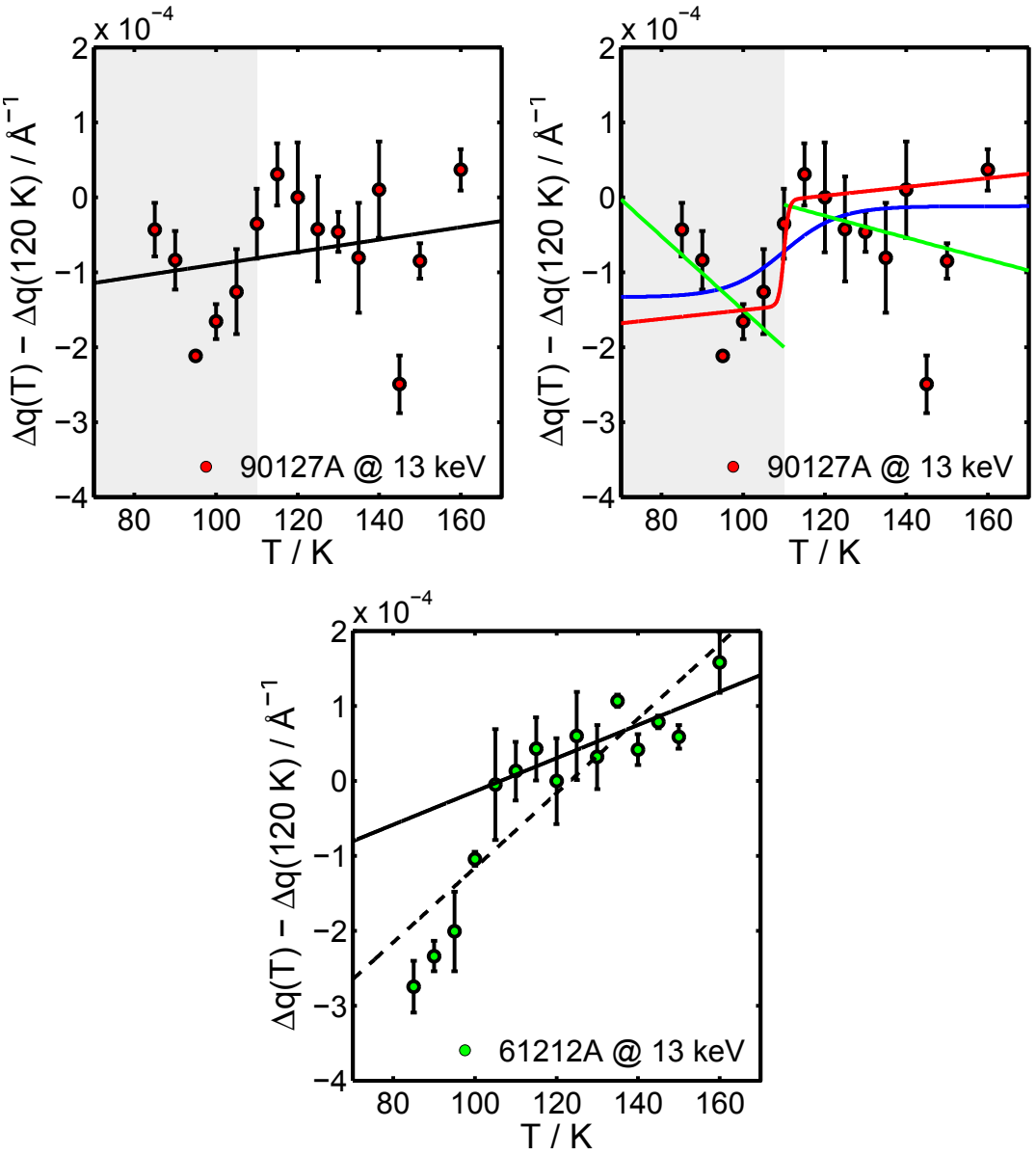

Figure 5.5: Top: q-separation of sample 90127A measured at BL9. Left: The change in $\Delta q(T) - \Delta q(120\,\mathrm{K})$ is assumed to show a linear behavior. The black line corresponds to a linear fit. Right: The change in $\Delta q(T) - \Delta q(120\,\mathrm{K})$ is assumed to show a non-linear shift due to the passing of T_C, which is set to the measured value of 110 K. The red, blue, and green lines correspond to fits to the functions $l(T)$, $t(T)$, and $s(T)$, respectively. Bottom: Separation data of sample 61212A measured at BL9. The black lines correspond to linear fits to the data.

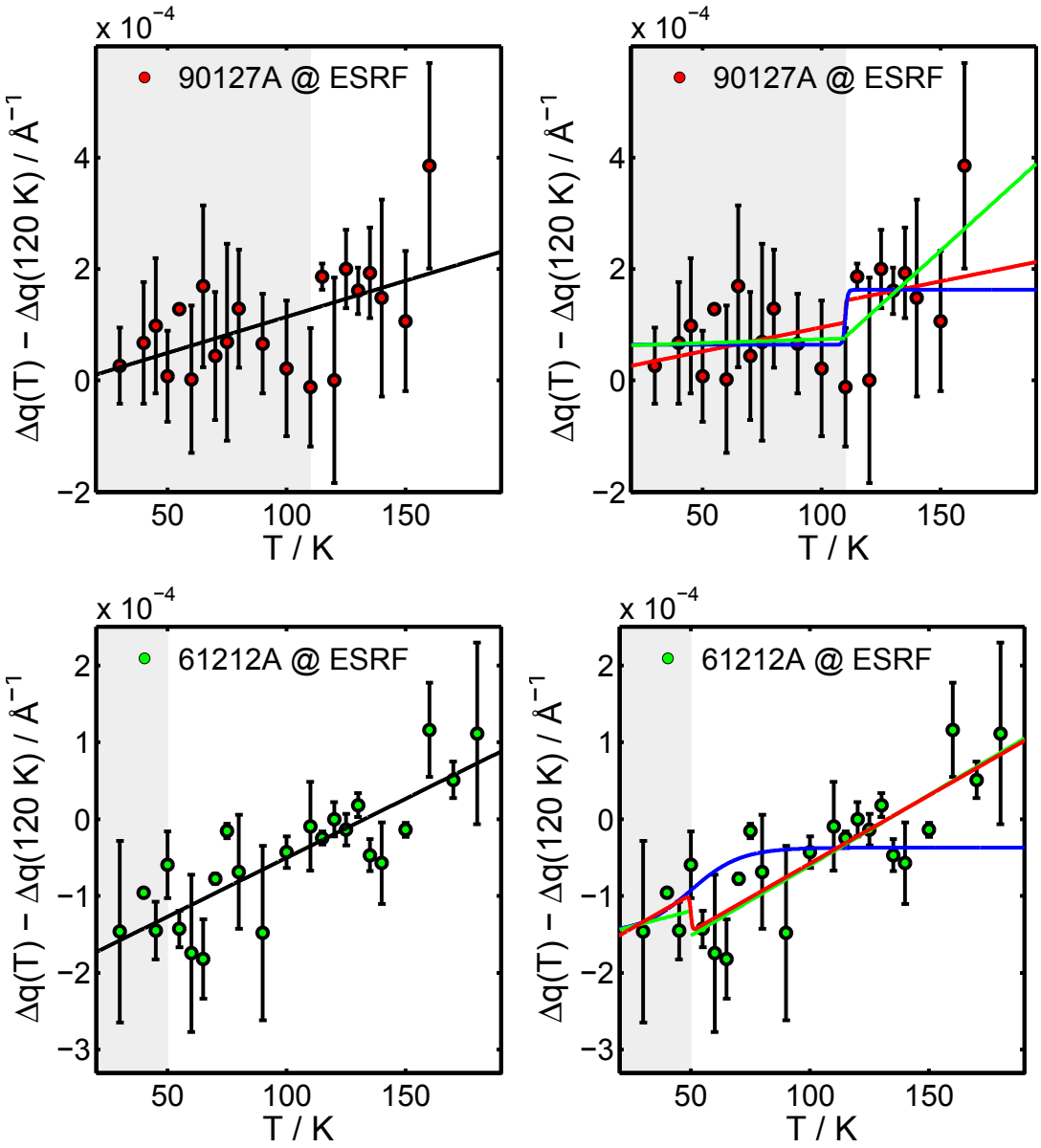

Figure 5.6: Top and bottom show the q-separation measured at BM28 of sample 90127A and 61212A, respectively. Left: The change in $\Delta q(T) - \Delta q(120\,\mathrm{K})$ is assumed to show a linear behavior. The black lines correspond to linear fits. Right: The change in $\Delta q(T) - \Delta q(120\,\mathrm{K})$ is assumed to show a non-linear shift due to the passing of T_C, which is set to the measured values of 110 K and 50 K. The red, blue, and green lines correspond to fits to the functions $l(T)$, $t(T)$, and $s(T)$, respectively.

	90127A		61212A	
	slope	$\Delta q(T_C)$	slope	$\Delta q(T_C)$
DELTA 15 keV	2.6 ± 1.3	1.3 ± 0.2	1.9 ± 2.0	-
DELTA 13 keV	0.8 ± 2.2	1.5 ± 0.3	2.2 ± 1.2	-
ESRF 15 keV	1.3 ± 1.0	0.9 ± 0.4	1.5 ± 0.5	1^*

Table 5.1: The slopes determined via linear fits to the q-separation data for both samples and the estimated shifts $\Delta q(T_C)$ according to the non-linear approach. The dimensions of the slopes and shifts are $10^{-6}\,(\text{ÅK})^{-1}$ and $10^{-4}\,\text{Å}^{-1}$, respectively. * Only the value of the shift determined with function $t(T)$ is displayed here.

Comparing the quality of the acquired data at DELTA and ESRF it becomes clear that the estimated errors at the ESRF are twice as large as the errors at DELTA indicating a better reproducibility of the measurements at DELTA. Both the linear and non-linear approach are summarized in table 5.1. The linear approach yields concurring slopes within the estimated errors for both samples, considering the slope of the black solid line in figure 5.5 bottom. Due to the same effect of thermal heating on both the substrate and the layer, the linear fit should provide a constant value. Therefore, the concurring, non-zero slopes indicate a non-linear change in the q-separation data. However, a slightly different thermal expansion of GaMnAs and GaAs on the order of the averaged slope of $(1.7 \pm 1.5) \cdot 10^{-6}\,(\text{ÅK})^{-1}$ cannot be excluded. On the same note, the fitting models expecting a transition yield an averaged shift on the order of $\Delta q(T_C) = (1.2 \pm 0.3) \cdot 10^{-4}\,\text{Å}^{-1}$ for sample 90127A. Particularly $l(T)$, which is a linear combination of a linear function and a tanh-function, shows a tanh-like behavior for each performed experiment strongly suggesting a continuous transition at T_C rather than a linear behavior across the whole temperature range. The fact that the Δq shifts do not differ significantly between the experiments at DELTA and ESRF indicates, that the direction of the in-plane magnetization shows no effect on the out-of-plane response of the lattice. However, the shift of $\Delta q(T_C) = (1.2 \pm 0.3) \cdot 10^{-4}\,\text{Å}^{-1}$ lies on the same order of magnitude as the estimated errors of the measurements coinciding with the experiments' resolution. For sample 61212A the non-linear approach did not yield consistent results and therefore, no statements can be made at this point. In order to draw conclusions for sample 61212A more measurements below T_C at deeper temperatures are needed.
The estimated shift $\Delta q(T_C)$ can be translated to changes in the lattice constant of GaMnAs, if the assumption holds that the magnetic ordering does not impact the lattice of the GaAs substrate. This implies, that the origin of the shift lies in the GaMnAs layer and that the lattice constant a_{GaAs} remains constant at the phase transition, meaning for $T = [T_C - \Delta T : T_C + \Delta T]$. As a consequence, $\Delta q^{\text{pt}}(T_C) = q_{\text{GaMnAs}}(T_C + \Delta T) - q_{\text{GaMnAs}}(T_C - \Delta T)$ is defined as the shift occurring at the phase transition. Then $\Delta a^{\text{pt}}(T_C) = a_{\text{GaMnAs}}(T_C + \Delta T) - a_{\text{GaMnAs}}(T_C - \Delta T)$ can be estimated to

$$\Delta a^{\text{pt}}(T_C) = -\frac{a^2_{\text{GaMnAs}} \Delta q^{\text{pt}}(T_C)}{8\pi} = (-1.5 \pm 0.4) \cdot 10^{-4}\,\text{Å} \tag{5.6}$$

with a GaMnAs lattice constant on the order of 5.6 Å. This change in lattice constant is investigated directly in the following section.

5.3 Determination of the GaMnAs lattice constant

For the purpose of investigating the magnetostriction effect directly on the GaMnAs lattice, the lattice constant a_{GaMnAs} was determined in dependency of the temperature. Because of the lack of calibration of the θ-axis, the position of the Bragg reflections were not absolute. Therefore, the lattice constant could not be obtained via

$$\lambda = 2d \cdot \sin(\theta) \tag{5.7}$$

and

$$d = \frac{a_{\mathrm{GaMnAs}}}{\sqrt{h^2 + k^2 + l^2}}, \tag{5.8}$$

with the Miller indices h, k, and l. Instead, equation 2.17 was modified and used as a model function

$$I_{\mathrm{mod}}(q) = K \cdot |A_{\mathrm{GaAs}} + A_{\mathrm{GaMnAs}} \cdot G \cdot L(q) \cdot E(q)|^2 + P(q), \tag{5.9}$$

where G is a weighting factor and K is a constant. Since the application of a Laue function as a model did not suffice, the three functions $L(q)$,$E(q)$ and $P(q)$ are used to model the decay of the intensity over several orders of magnitude. Here,

$$L(q) = \frac{a_1}{(q - 4.5)^2 + (a_2/2)^2} \tag{5.10}$$

is the Lorentz distribution,

$$E(q) = e^{(-a_3^2 \cdot (4.45 - q))^2} \tag{5.11}$$

is an exponential function and

$$P(q) = a_4 \cdot (q - a_5)^2 + a_6 \tag{5.12}$$

is a polynomial of degree two. A_{GaAs} and A_{GaMnAs} are scattering factors for the substrate and the GaMnAs layer, respectively and are given through

$$A_{\mathrm{GaAs}}(q) = S_{\mathrm{GaAs}}(q) \cdot \frac{1}{1 - e^{(iq - \mu_{\mathrm{GaAs}}) a_{\mathrm{GaAs}}}} \tag{5.13}$$

and

$$A_{\mathrm{GaMnAs}}(q) = S_{\mathrm{GaMnAs}}(q) \left[\frac{1 - e^{(\mathrm{i}q - \mu_{\mathrm{GaMnAs}}) n \cdot a_{\mathrm{GaMnAs}}}}{1 - e^{(\mathrm{i}q - \mu_{\mathrm{GaMnAs}}) a_{\mathrm{GaMnAs}}}} - 1 \right] \tag{5.14}$$

according to equations 2.15 and 2.16, respectively. $S_{\mathrm{GaAs}}(q)$ and $S_{\mathrm{GaMnAs}}(q)$ represent the structure factors calculated with equation 2.8. The atomic scattering factors were taken from the literature [Wang93]. The absorption coefficients $\mu_{\mathrm{GaAs}} = 3.267 \cdot 10^{-7}$ Å and $\mu_{\mathrm{GaMnAs}} = 3.244 \cdot 10^{-7}$ Å for 15 keV and $\mu_{\mathrm{GaAs}} = 5.501 \cdot 10^{-7}$ Å and $\mu_{\mathrm{GaMnAs}} = 5.463 \cdot 10^{-7}$ Å for 13 keV were taken from [Henke93].
In the case of the data acquired at the ESRF the focus of the fitting process lay on the oscillations. For this purpose $I(q)$ was fitted to the diffraction patterns and a_{GaAs} was held constant at 5.6475 Å. The number of layers n was set to 89. With the lattice constant of GaAs, which is close to the GaMnAs lattice constant, and n the layer thickness is calculated to 50.2 nm, which is in good agreement with the layer thicknesses determined in section 3.2.3. Figure 5.7 illustrates a generic diffraction pattern of sample 90127A and its corresponding model function in black and red, respectively. The oscillations below $q = 4.3\,\text{Å}^{-1}$ are almost damped completely, but the first ten were modeled well. The inset shows the fitted function for the q-range, which was not used for the modeling process. It can be seen, that the position of the modeled (004) Bragg reflections agrees with the measured one.

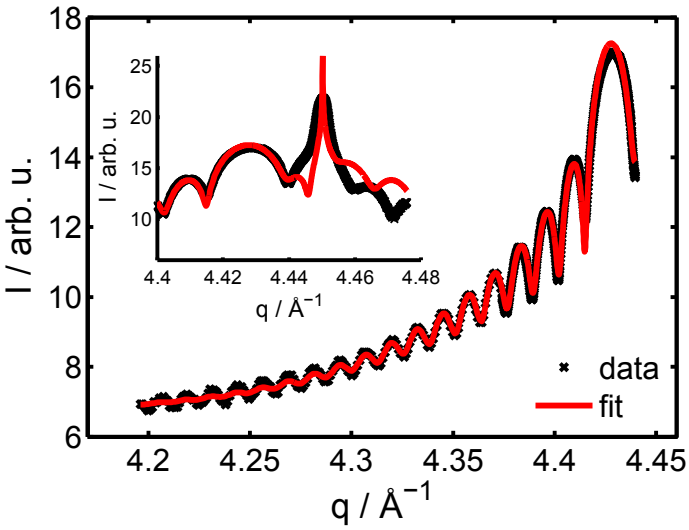

Figure 5.7: The model function I_{mod} is fitted to a generic truncation rod of sample 90127A at the ESRF focusing on the oscillations in a q-range of 4.3 - 4.44 Å^{-1}. The inset shows the fitted model for the q-range, which was not used for the modeling process. The (004) GaAs Bragg peak position was set to 5.6475 Å for the modeling process and concurs with the measured one.

The modeling of the oscillations of sample 61212A required an increased damping rate, which resulted in an acceptable modeling range of the first six oscillations. Nonetheless, the intensity decay over several orders of magnitude is modeled well. The fitting parameters a_i of the model functions were varied to model the decay of the intensity over several orders of magnitude. The GaMnAs lattice constant a_{GaMnAs}, which mainly determines the position of the oscillations was the fit parameter of interest. Figure 5.8 shows the obtained GaMnAs lattice constant referenced to the lattice constants in

the vicinity of the Curie temperature for both samples. The lattice constants for both samples were determined by averaging over the lattice constants measured and modeled for each independent temperature series. The displayed error bars correspond to the error due to the averaging process. Taking into account, that the fitted value of a_{GaMnAs} did not vary significantly, while varying the damping parameters, this approach seems reasonable.

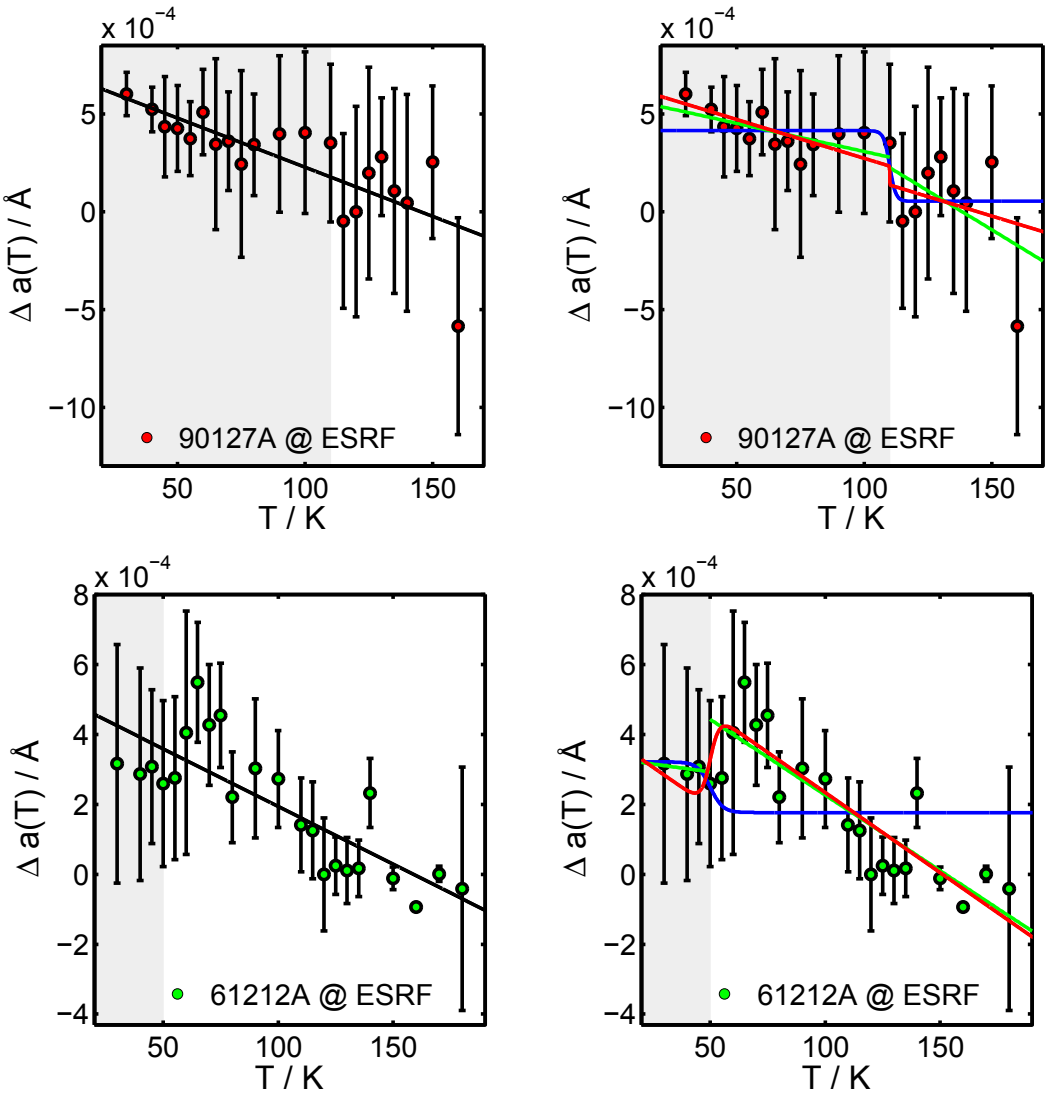

Figure 5.8: Top and bottom show the GaMnAs lattice constant referenced to the constant measured at 120 K of both samples for the experiments conducted at the ESRF. Left: The change in Δa is assumed to show a linear behavior. The black lines correspond to linear fit. Right: The change in Δa is assumed to show a non-linear effect due to the passing of T_{C}, which is set to the measured values of 110 K and 50 K. The red, blue, and green lines correspond to fits to the functions $l(T)$, $t(T)$, and $s(T)$, respectively.

The impact of thermal heating on the lattice was excluded by not including the GaAs lattice parameter a_{GaAs} to the pool of free fitting parameters. The obtained a_{GaMnAs} are therefore, again no absolute values. In order to compare the data to the q-separation it is displayed in reference to the lattice constants determined at 120 K. The sample alignment was not optimized during the first two temperature series for sample 90127A, which may explain the slightly larger error bars. $\Delta a(T) = a_{\mathrm{GaMnAs}}(120\,\mathrm{K}) - a_{\mathrm{GaMnAs}}(T)$ is introduced for convenience. The data were treated analogous to the q-separation data. Assuming a linear behavior across the whole temperature range, linear fits were performed for both samples and are displayed through black solid lines on the left side of figure 5.8. The slopes were determined to $(-5.0 \pm 2.0) \cdot 10^{-6}$ Å/K and $(-3.3 \pm 1.1) \cdot 10^{-6}$ Å/K for samples 90127A and 61212A, respectively. The slopes concur within the estimated errors.
The red, blue, and green lines on the right side correspond to the model functions $l(T)$, $t(T)$, and $s(T)$, respectively. The red and green lines suggest a linear behavior across the whole temperature range, while the fit according to $t(T)$ indicates a continuous transition at T_{C} for sample 90127A. The averaged shift $\Delta a^{\mathrm{pt}}(T_{\mathrm{C}})$ lies on the order of $(-1.7 \pm 1.0) \cdot 10^{-4}$. The red and green fits to the data of sample 61212A suggest linear behavior with a discontinuity in the vicinity of T_{C}. The fit according to $t(T)$ again shows a continuous transition, but does not seem to model the data well. Hence, no final conclusion can be drawn without more data in the lower temperature regime.

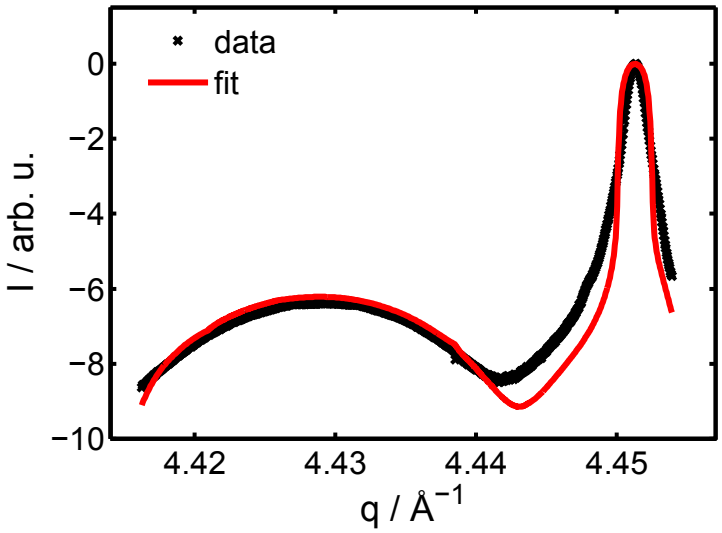

Figure 5.9: The convolution of the model function I_{new} and $m(Q)$ is fitted to a generic truncation rod of sample 90127A at the DELTA focusing on the (004) GaAs and GaMnAs Bragg reflections.

In order to analyze the data measured at BL9 I_{mod} had to be altered, because of the narrow q-range. Since the diffraction patterns show only one or two oscillations, the emphasis lay on the (004) Bragg reflections of GaAs and GaMnAs. Therefore, the

functions modeling the decay of the intensity were not needed.

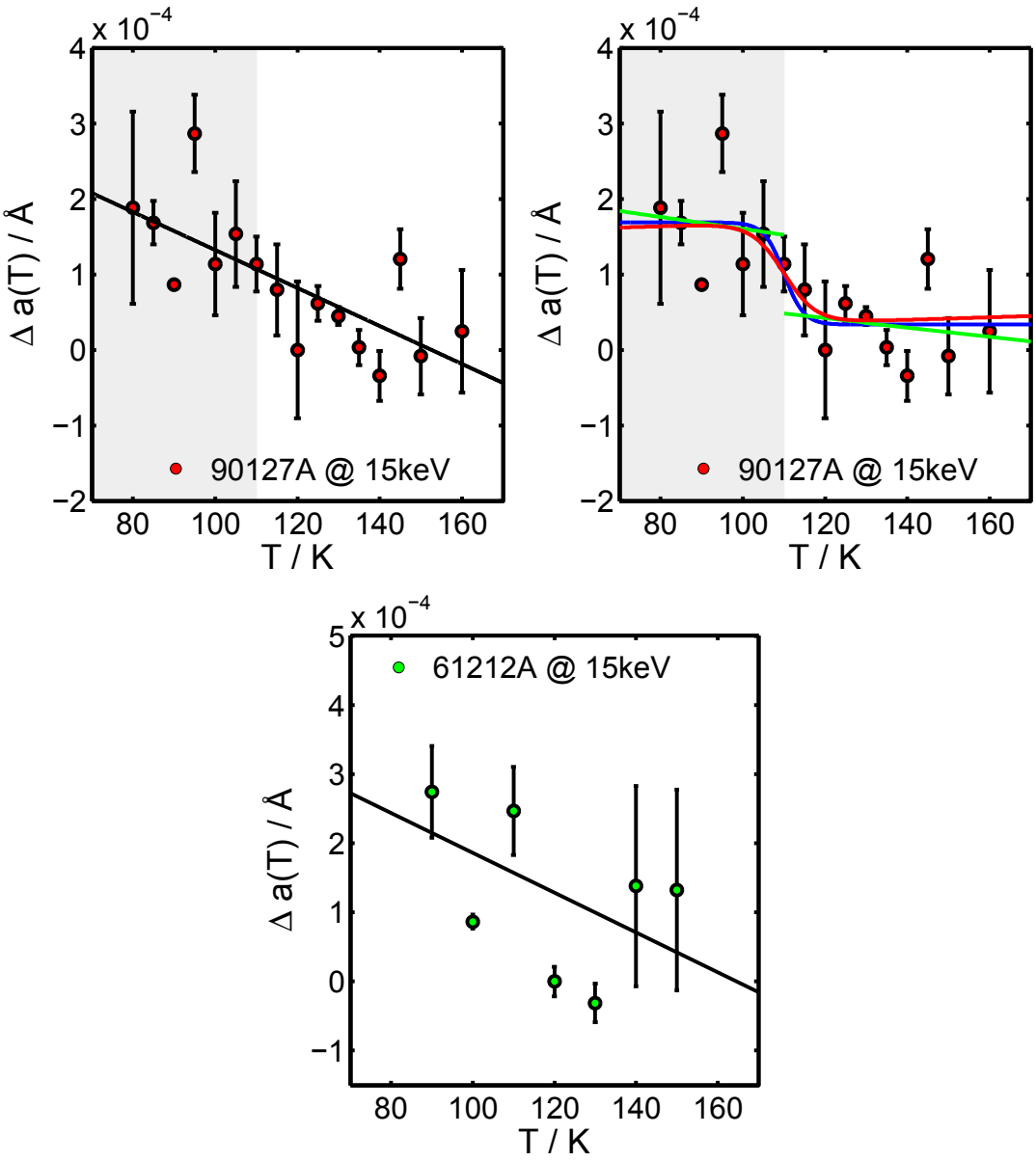

Figure 5.10: Top: GaMnAs lattice constant of sample 90127A measured at BL9. Left: The change in Δa is assumed to show a linear behavior. The black line corresponds to a linear fit. Right: The change in Δa is assumed to show a non-linear effect due to the passing of T_C, which is set to the measured value of 110 K. The red, blue, and green lines correspond to fits to the functions $l(T)$, $t(T)$, and $s(T)$, respectively. Bottom: GaMnAs lattice constant of sample 61212A measured at BL9. The black line corresponds to a linear fit to the data.

The simplified model function

$$I_{\text{new}} = |A_{\text{GaAs}} + A_{\text{GaMnAs}} \cdot G|^2 \tag{5.15}$$

was then convolved with a mollifier

$$m(Q) = \frac{1}{E} \cdot \mathrm{e}^{\frac{-1}{1-Q^2}}, \tag{5.16}$$

where E is a constant that belongs to (0,1]. Further, $m(0) = 0$ for $|Q| > E$ applies. The convolution was used to smooth the sharp (004) GaAs Bragg reflection, while remaining as close as possible to I_{new}. A typical fit to a generic truncation rod is displayed in figure 5.9. In this model a different number of layers had to be assumed for the samples; $n = 70$ and $n = 88$ for samples 90127A and 61212A, respectively. This leads to layer thicknesses of 39.5 nm and 49.7 nm, which also concurs with $d_{\text{layer}} = 50\,\text{nm}$ determined in chapter 3.2.3. Figure 5.10 displays the change in lattice constant $\Delta a(T)$ measured at BL9 utilizing a photon energy of 15 keV. The data of sample 90127A is shown on the top, while the bottom part illustrates the data corresponding to sample 61212A. Linear fits to both data sets shown in black yield concurring slopes within the estimated errors of $(-2.5 \pm 1.4) \cdot 10^{-6}$ Å/K and $(-2.9 \pm 4.1) \cdot 10^{-6}$ Å/K, for samples 90127A and 61212A, respectively.
The top right part of figure 5.10 depicts corresponding fits to the model functions $l(T)$ in red, $t(T)$ in blue, and $s(T)$ in green. Both the red and blue lines indicate a continuous transition at T_{C} on the order of $\Delta a^{\text{pt}}(T_{\text{C}}) = (-1.3 \pm 0.2) \cdot 10^{-4}$ Å. This behavior is further supported by the green line showing a discontinuity on the same order of magnitude at T_{C}.
The lattice constants determined for the experiments performed at BL9 utilizing a photon energy of 13 keV are displayed in figure 5.11. The top-left and bottom parts show the linear approach to the data for samples 90127A and 61212A, respectively. The linear regression yield slopes of $(-4.6 \pm 1.5) \cdot 10^{-6}$ Å/K (90127A) and $(-2.8 \pm 1.0) \cdot 10^{-6}$ Å/K (61212A).
The non-linear approach for sample 90127A is depicted on the top-right part. The red, blue, and green lines correspond to fits according to $l(T)$, $t(T)$, and $s(T)$, respectively. The red and blue lines suggest a continuous transition at T_{C} on the order of $\Delta a^{\text{pt}}(T_{\text{C}}) = (-1.9 \pm 0.2) \cdot 10^{-4}$ Å. This behavior is additionally implied by the green line showing a discontinuity and significantly different slopes below and above T_{C}.

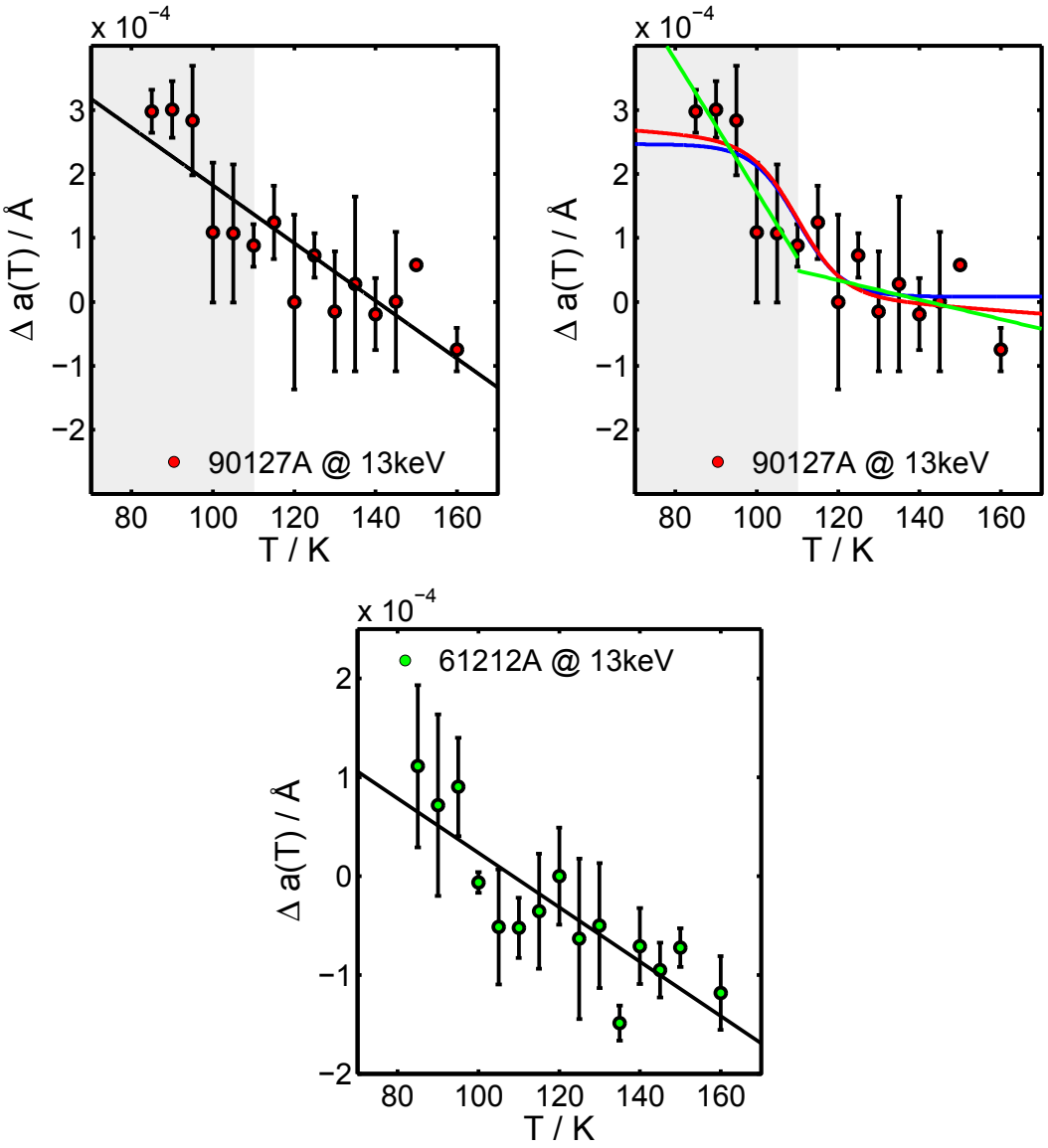

Figure 5.11: Top: GaMnAs lattice constant of sample 90127A measured at BL9. Left: The change in Δa is assumed to show a linear behavior. The black line corresponds to a linear fit. Right: The change in Δa is assumed to show a non-linear effect due to the passing of T_C, which is set to the measured value of 110 K. The red, blue, and green lines correspond to fits to the functions $l(T)$, $t(T)$, and $s(T)$, respectively. Bottom: GaMnAs lattice constant of sample 61212A measured at BL9. The black line corresponds to a linear fit to the data.

	90127A		61212A	
	slope	$\Delta a^{\mathrm{pt}}(T_{\mathrm{C}})$	slope	$\Delta a^{\mathrm{pt}}(T_{\mathrm{C}})$
DELTA 15 keV	-2.5 ± 1.4	-1.3 ± 0.2	-2.9 ± 4.1	-
DELTA 13 keV	-4.6 ± 1.5	-1.9 ± 0.2	-2.8 ± 1.0	-
ESRF 15 keV	-5.0 ± 2.0	-1.7 ± 1.0	-3.3 ± 1.1	-1.5^{*}

Table 5.2: The slopes determined via linear fits to the change in lattice constant for both samples and the estimated shifts $\Delta a(T_{\mathrm{C}})$ according to the non-linear approach. The dimensions of the slopes and shifts are 10^{-6} Å/K and 10^{-4} Å, respectively. * Only the value of the shift determined with function $t(T)$ is displayed here.

Table 5.2 lists the determined slopes for both samples and all three experiments. The slopes determined through the linear approach agree within the estimated errors for both samples. Indicating a difference in thermal expansion on the order of the averaged slope of $(-3.5 \pm 2.1) \cdot 10^{-6}$ Å/K. However, the non-linear approach suggests a continuous transition at T_{C} on the order of $\Delta a^{\mathrm{pt}}(T_{\mathrm{C}}) = (-1.6 \pm 0.6) \cdot 10^{-4}$ Å for sample 90127A and therefore on the same order of magnitude estimated from the $\Delta q^{\mathrm{pt}}(T_{\mathrm{C}})$ values in section 5.2. Especially the experiments performed at DELTA indicate a different behavior below and above T_{C}. Here, the fits corresponding to the linear combination of a linear function and a tanh-function show tanh-like behavior supporting a continuous transition. However, the observed transition lies on the same order of magnitude as the estimated errors. The data for sample 61212A gives evidence of a linear behavior across the whole temperature range. To draw further conclusions, more data points below T_{C} are needed.

5.4 Comparison of the changes in the q-separation and the GaMnAs lattice constant

In order to draw final conclusions, the findings of both the q-separation and the change in lattice constant are compared and discussed. Two approaches were taken to analyze the observed changes in $\Delta q(T) - \Delta q(120\,\mathrm{K})$ and Δa. The first one assumes a linear behavior across the whole sampled temperature range, which means that no effect due to magnetostriction was observed. Here, all determined slopes of the applied linear fits concur within the estimated errors for both samples and each data set. The linear fits were expected to yield a constant value due to the similar thermal lattice expansion of GaAs and GaMnAs. Therefore, a non-linear effect due to magnetostriction seems far more likely. However, small differences in the thermal lattice expansion of GaMnAs and GaAs cannot be excluded.
This was investigated by the second approach assuming a non-linear shift due to magnetostriction induced by the magnetic phase transition. Here, three model functions were used to model the data. The best indicator is $l(T)$; a linear combination of a linear function and a tanh-function combining both approaches. Considering that $l(T)$ invariably shows a tanh-like behavior for both the q-separation and $\Delta a(T)$ for all conducted experiments with sample 90127A, a non-linear shift is strongly suggested. The

determined continuous transition around T_C for both data sets $\Delta q(T) - \Delta q(120\,\mathrm{k})$ and Δa lie on an order of magnitude of $\Delta q^{pt}(T_C) = (1.2 \pm 0.3) \cdot 10^{-4}\,\text{Å}^{-1}$ and $\Delta a^{pt}(T_C) = (-1.6 \pm 0.6) \cdot 10^{-4}\,\text{Å}$, respectively. Strikingly, the determined shift $\Delta a^{pt}(T_C)$ is in very good agreement with the estimated changes $\Delta a^{pt}(\Delta q^{pt})$ from the shift $\Delta q^{pt}(T_C)$, which is summarized in table 5.3. In conclusion, both the investigation of the q-separation determined via the positions of the GaAs and GaMnAs (004) Bragg reflections and the change in lattice constant provided by two modeling functions yield concurring shifts. Hence, the effect of magnetostriction on the lattice constant of sample 90127A can be estimated to be on the order of $\Delta a^{pt} = (-1.6 \pm 0.6) \cdot 10^{-4}$ Å. It has to be noted, that the observed shifts lie on the same order as the experiments' resolution. The relative change in lattice constant $\Delta a^{pt}(T_C)/a$ was determined to $(-2.8 \pm 1.1) \cdot 10^{-5}$, which is in good agreement with the magnetostriction constants on the order of $1 \cdot 10^{-5}$ determined by Masmanidis et al. [Masmanidis05]. Compared to the thermal expansion of GaAs on an order of $1 \cdot 10^{-4}$ the effect of magnetostriction on the crystal lattice is negligible.

	$\Delta q^{pt}(T_C)$	$\Delta a^{pt}(\Delta q^{pt})$	$\Delta a^{pt}(T_C)$
90127A	1.2 ± 0.3	-1.5 ± 0.4	-1.6 ± 0.6

Table 5.3: The determined shifts $\Delta q^{pt}(T_C)$, $\Delta a^{pt}(T_C)$, and the estimated shift $\Delta a^{pt}(\Delta q^{pt})$ according to the non-linear approach. The dimension of the shifts are $10^{-4}\,\text{Å}^{-1}$ in q and 10^{-4} Å in the real space. The determined shifts are in very good agreement with the estimation.

The data for sample 61212A gathered at the ESRF indicate a discontinuity on the order of $\Delta q^{pt}(T_C) = 1 \cdot 10^{-4}\,\text{Å}^{-1}$ and $\Delta a^{pt}(T_C) = -1.5 \cdot 10^{-4}$ Å. However, the model function $t(T)$ does not seem to follow the measured data well, which may result from the few data points measured below T_C. Hence, no final conclusion can be drawn for sample 61212A without more data taken below T_C.

Chapter 6

Thermal induced lattice expansion of (In,Ga)As/GaAs quantum dots

The experiments and results discussed in this chapter were published in Nanotechnology volume **27**, page 425702 under the title 'Polaron-induced lattice distortion of (In,Ga)As/GaAs quantum dots by optically excited carriers' in 2016 [Tiemeyer16].

Quantum dots (QDs) are nanoscale semiconductor structures included in a surrounding semiconductor matrix. Carriers in QDs are confined in all three spacial directions resulting in atom like, discrete energy levels, even though, a QD can consist of several thousand atoms. This gives rise to a broad range of experiments that study such atomic structures on a macroscopic scale.
The formation of QDs can be achieved by lithography, chemical etching or spontaneous formation [Kubena87, Sotomayor Torres94]. However, the fabrication of self-assembled QDs by epitaxial growth allows the tailoring of properties such as shape, size or composition [Michler03]. In the past, self-assembled QDs have been grown on large variety of III-V, II-VI, and IV semiconductor structures. The diverse and unique properties of QDs led the way for a diversity of QD devices such as lasers [Ledentsov98, Deppe00] and infrared detector devices [Stiff-Roberts02]. Additionally, non-classical light sources such as single-electron or -photon devices can be realized with single QDs, which play a key role in the field of quantum information technology [Reithmaier04, Greilich09]. One example is an exciton storage device utilizing the carrier localization in QDs realized by Lundstrom et al. in 1999 [Lundstrom99]. The fabrication of QDs, their properties, and applications are reviewed in [Ledentsov98, Michler03].
The following chapter addresses the investigation of carrier-phonon interactions in (In,Ga)As/GaAs self-assembled QDs. (In,Ga)As/GaAs self-assembled QDs result from heteroepitaxial Stranski-Krastanov growth [Bauer58, Goldstein85]. The critical layer thickness for the formation of islands of InAs on GaAs has been found to be 1.5 to 1.7 monolayers [Leonard94, Daruka97]. These islands are in fact the QDs, which

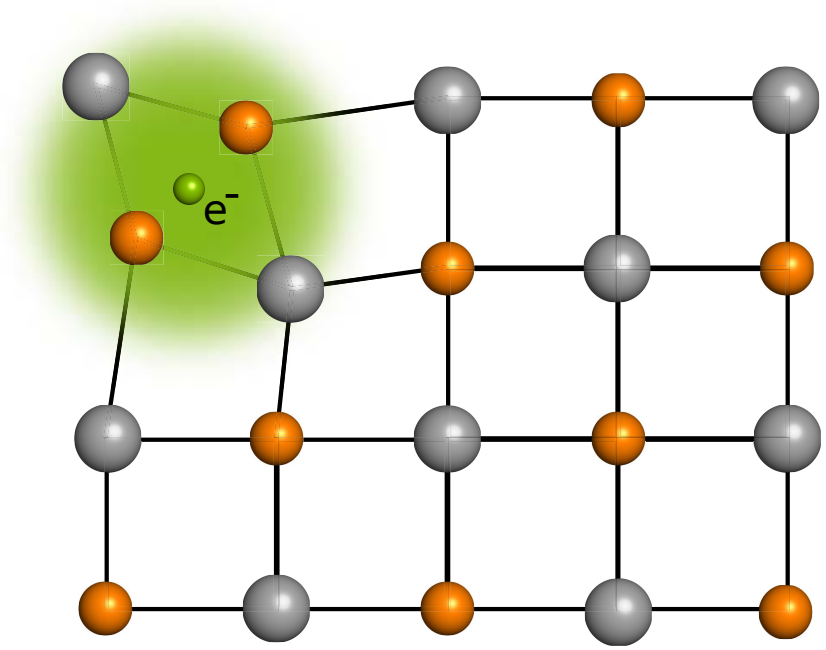

Figure 6.1: Sketched crystal lattice distortion due to a polaron. An electron accompanied by a phonon cloud distorts the crystal lattice of positively and negatively charged atoms represented in orange and grey, respectively. Adapted and edited from [Tiemeyer12]. Copyright TU Dortmund (2012). Permission granted by S. Tiemeyer.

typically have a narrow size distribution [Leonard93, Grundmann95a] and densities on the order of 10^{10} to 10^{11} dots per cm^2 [Stangl04]. The crystal structure of the QDs is heavily affected by the considerable strain fields introduced by the growth process [Benabbas99]. Since the crystal structure has a great influence on the electronic properties [Grundmann95b], the tailoring of exactly these becomes possible by strain engineering [Guffarth01, Seravalli07].
Theoretical considerations of carrier-phonon interactions predict the formation of a stable polaron distorting the crystal lattice [Vagov02] as sketched in figure 6.1. A polaron is the quasi-particle describing the carrier-phonon coupling. An electron accompanied by a phonon cloud travels through the crystal lattice and attracts and repels the positively and negatively charged atoms, respectively. This interaction ultimately leads to a shift of the equilibrium lattice constant. Although the polaronic effects are rather weak in the covalent bound crystals GaAs and InAs they become important in the case of QDs [Verzelen02]. Several experiments [Besombes01, Borri01] revealed a spectral broadening under optical excitation, which was ascribed to the proposed shift of lattice constant induced by the formation of a stable polaron. However, direct evidence of the lattice distortion was still missing giving rise to the investigation by Tiemeyer et al. [Tiemeyer16].

6.1 Optically induced lattice distortion of (In,Ga)As/GaAs QDs

S. Tiemeyer et al. investigated the effect of polarons on the crystal lattice of (In,Ga)As/GaAs QDs [Tiemeyer12, Tiemeyer16]. These polarons are introduced by optically exciting carriers with a laser. The investigated sample QD13776 consists of a (In,Ga)As/GaAs quantum dot multilayer structure grown on a (001) oriented 500 nm thick GaAs substrate. The multilayer counts five layers each consisting of a 1.9 monolayer thick InAs layer capped with 30 nm of GaAs resulting in the formation of the QDs.

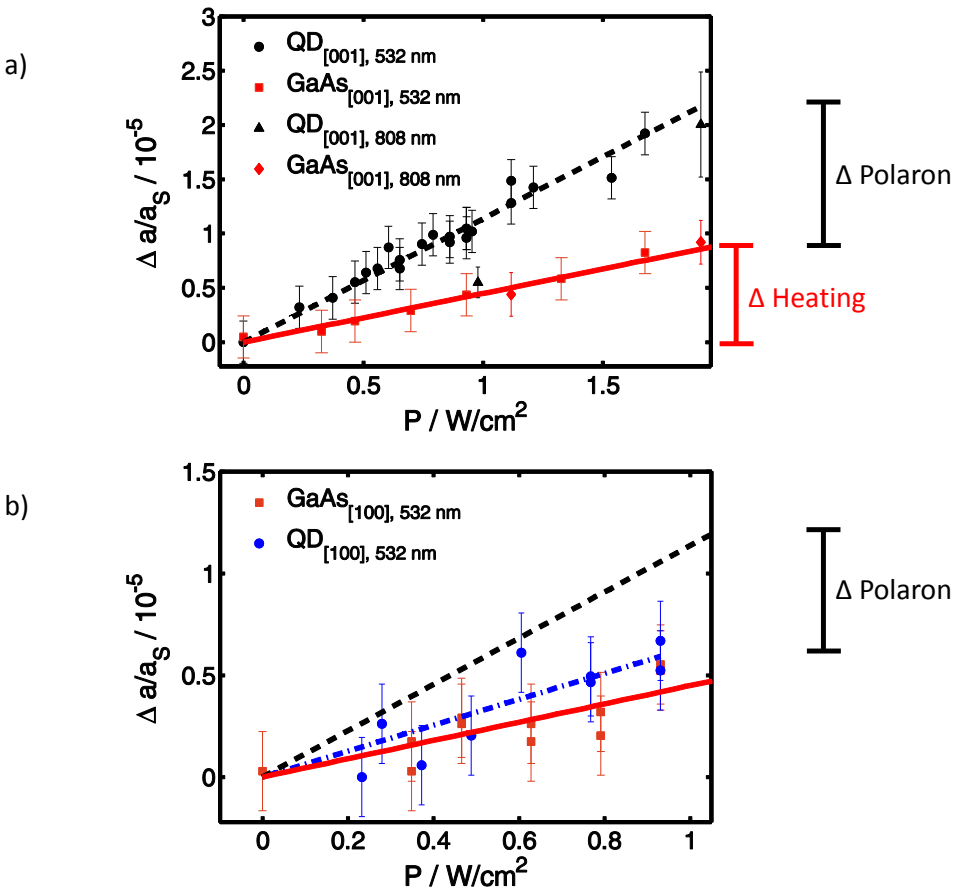

Figure 6.2: Relative lattice expansion of (In,Ga)As/GaAs quantum dots and a GaAs reference along the [001] a) and [100] b) GaAs crystal directions. The black and blue dashed lines correspond to linear fits to the QD data for the [001] a) and [100] b) direction, respectively, while the red solid lines visualize a linear fit to both directions in the case of the GaAs reference. Δ Polaron and Δ Heating indicate the effect on the lattice constant due to the formation of polarons and laser-induced heating, respectively. The [001] direction was investigated with two lasers of different excitation wavelength. This figure was reproduced and modified with permission by IOP Publishing from [Tiemeyer16]. All rights reserved.

The top layer is again capped with 50 nm GaAs. High resolution XRD experiments were conducted to investigate the polaron-induced lattice distortion by excited carriers. A diode-pumped, frequency doubled Nd:YAG laser and a laser diode were used to optically excite the carriers within the dots with wavelengths of 532 nm and 808 nm, respectively. A laser shutter was utilized to facilitate measuring each data point of the diffraction patterns with and without optical illumination. The experiments were conducted at beamlines BL9 at DELTA and P08 at PETRA III [Seeck12] at a sample temperature of 100 K. The scattered x-ray intensity was detected utilizing Pilatus 100K and Mythen 1D detectors. Besides the QD sample a GaAs wafer was investigated to serve as a reference. The in-plane ([100]) and out-of-plane ([001]) response to the optical excitement Δa was normalized to the GaAs lattice constant $a_S = 5.6535$ [Blakemore82] at 300 K and is shown in dependence of the laser excitation power in figure 6.2. Linear fits to the [001] and [100] QD direction and both GaAs directions shown in black, blue, and red, respectively, revealed significant differences in slope. The slope for both GaAs directions concur within the error bars and is determined to $(4.53 \pm 1.02) \cdot 10^{-4}\,\mathrm{cm^2W^{-1}}$ indicating the expected isotropic lattice expansion due to thermal heating. While the [100] direction of the QD sample shows a similar slope of $(6.35 \pm 1.54) \cdot 10^{-4}\,\mathrm{cm^2W^{-1}}$ compared to GaAs, the slope of the [001] direction of $(11.37 \pm 0.64) \cdot 10^{-4}\,\mathrm{cm^2W^{-1}}$ differs significantly; strongly indicating a tetragonal distortion of the crystal lattice. However, the possibility remains that the observed distortion can be assigned to a pure thermal effect simply caused by the QD's presence, which gave rise to the investigation of the thermal effect presented in the next section.

6.2 The effect of thermal heating on the lattice expansion

To rule out a pure thermal effect as an explanation for the observed tetragonal distortion high resolution XRD experiments were performed on both samples with a photon energy of 15 keV at beamline BL9 at DELTA and the helium flow cryostat setup run on liquid nitrogen presented in chapter 4.4. In order to determine the thermal impact on the crystal lattice distortion the (002) and (004) Bragg reflections of both samples were detected in a temperature range between 100 K and 125 K. A typical 2θ - θ scan is depicted in figure 6.3 including the matching Gaussian fit in black. The change in lattice constant is obtained by analyzing the differences $\Delta 2\theta = 2\theta_{004} - 2\theta_{002}$ between the (002) and (004) Bragg reflections as a function of the temperature T. This differences are identified by fitting Gaussian functions to both reflections providing their positions. Then, the angular separation is used to calculate the corresponding lattice constants via

$$2\theta_{002} = 2 \cdot \mathrm{atan}\left(\frac{\sin(\Delta 2\theta/2)}{2 - \cos(\Delta 2\theta/2)}\right) \tag{6.1}$$

and

$$a = \frac{\lambda}{\sin(2\theta_{002}/2)}. \tag{6.2}$$

The measured averaged change of the perpendicular lattice constant $\Delta a/a_s$ is shown in figure 6.4 c). Parts a) and b) show the measured data before the averaging process for the GaAs and QD samples, respectively. The red and black lines correspond to linear fits to the averaged GaAs and QD data, respectively.

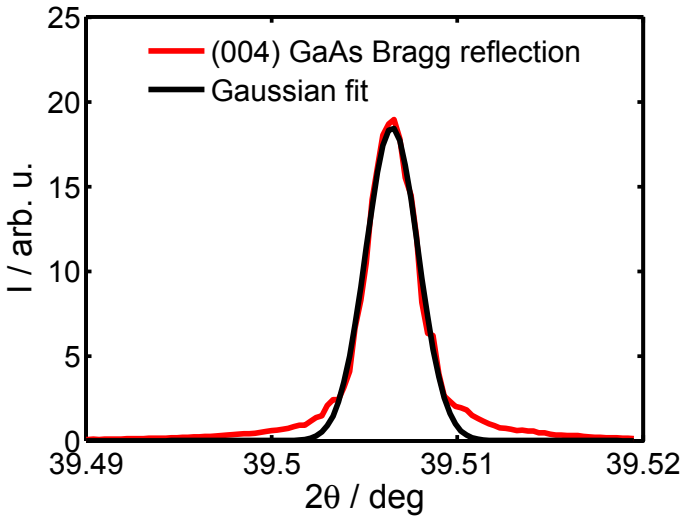

Figure 6.3: Measured (004) GaAs Bragg reflection at a temperature of 100 K in red and the corresponding Gaussian fit in black.

Every presented data point represents the change in lattice constant averaged over four consecutively performed scans of both Bragg reflections. The linear regression reveals slopes of $(1.26 \pm 1.4) \cdot 10^{-5}\,\mathrm{K}^{-1}$ and $(1.13 \pm 1.4) \cdot 10^{-5}\,\mathrm{K}^{-1}$ for the QDs and GaAs sample, respectively. This leads to the conclusion, that there is no significant contribution of the included QDs to the pure thermal lattice expansion within the accuracy of the experiment. The slopes allow for an estimation of the difference in relative lattice constants $\Delta a/a_s$ of both samples on the order of $1 \cdot 10^{-5}$ for a temperature range of $\Delta T = 10\,\mathrm{K}$. The overall change in lattice constant due to thermal heating however, lies on the order of $1 \cdot 10^{-4}$ in the same temperature range for both samples. Hence, both samples are assumed to show a similar thermal lattice expansion.

6.3 Comparison and conclusion

The goal of this investigation was to determine whether the tetragonal distortion could be assigned to a sole thermal effect introduced by the QDs. Comparing the relative change in lattice constant for the laser illuminated GaAs sample with maximum laser power of $1.9\,\mathrm{W/cm^2}$, which lies on the order of Δ Heating $= 0.5 \cdot 10^{-5}$, and the non-illuminated sample with thermal heating on the order of $1 \cdot 10^{-4}$ for $\Delta T = 10\,\mathrm{K}$ as discussed before leads to an estimation of a rise in temperature of $0.5\,\mathrm{K}$ due to laser irradiation. These findings lead to the conclusion that the tetragonal lattice distortion is

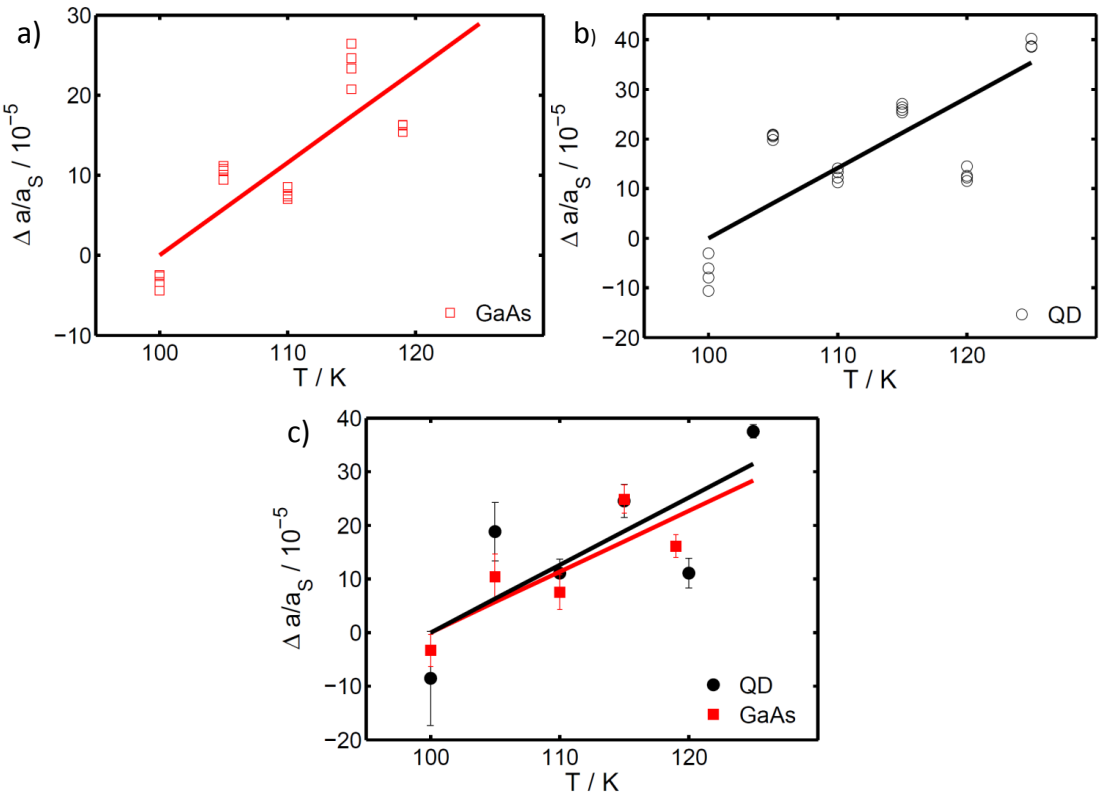

Figure 6.4: a) Acquired thermal expansion data for the GaAs reference sample. b) Thermal expansion data of the QD sample. c) Averaged thermal expansion of GaAs and the QD sample along the [001] direction. The temperature was varied between 100 K and 125 K. Linear fits in red and black correspond to the GaAs and QD sample, respectively. Part c) of this figure was reproduced with permission by IOP Publishing from [Tiemeyer16]. All rights reserved.

highly improbable to be caused by a pure thermal effect but can rather be assigned to the optically excitation of the confined carriers. This interpretation is further reinforced by the fact that the tetragonal distortion is observed for both laser excitation wavelengths as discussed in [Tiemeyer16]. Assuming, that the tetragonal distortion is homogeneous for all five QD layers, the overall distortion of the lattice constant along the [001] direction can be estimated to 6.4 fm per W/cm^2 utilizing the slope for the QD [001] direction. The lattice distortion due to thermal heating is estimated with the slope of the GaAs [001] direction to 2.5 fm, which corresponds to an amount of 40 % to the overall distortion. This implies, that the polaronic effect is the driving force behind the tetragonal distortion.

Chapter 7

Summary and outlook

In this thesis two different effects on the crystal lattices of semiconductors structures were investigated. First, the impact of magnetostriction occurring due to a second-order phase transition in GaMnAs thin film lattices was analyzed. The second effect is the thermal lattice expansion of self-assembled InAs/GaAs QDs and a GaAs sample in order to support the polaron induced tetragonal lattice distortion found in [Tiemeyer12].
In order to investigate the structural changes of both GaMnAs and self-assembled (In,Ga)As/GaAs QDs an XRD setup was developed at BL9 at DELTA, that allows the measuring of relative changes on lattice constants on the order of 10^{-5}. After the testing of several cryo systems with regard to a stable sample position and temperature as well as reproducible sample alignment the Optistat CF-2V of Oxford Instruments was selected. Utilizing a combination of ball bearings and a plate screwed to the diffractometer to stabilize the cryostat, reproducible sample positions and alignment were realized. The introduction of Pt-100 temperature sensors to the sample holder ensured a reliable sample temperature measurement. The developed setup allows the conduction of experiments on a temperature range of 80 K - 500 K with a precision of approximately 10^{-4} Å.
In the first part of this thesis, the focus lay on the effect of magnetostriction on GaMnAs thin films. Here, XRD experiments were performed at BL9 at DELTA and BM28 at the ESRF on two GaMnAs samples 90127A and 61212A with T_C of 110 K and 50 K, respectively. For both samples 50 nm-thin films of GaMnAs were grown by LT-MBE on GaAs substrates. The impact of spontaneous magnetostriction on the lattice was determined via the separation of both GaAs and GaMnAs (004) Bragg reflections on the q-scale $\Delta q(T) - \Delta q(120\,\mathrm{K})$ and by performed fits to the measured truncation rods yielding the GaMnAs lattice constant a_{GaMnAs}. The fact, that a linear combination of a linear function and a tanh-function invariably showed tanh-like behavior lead to the conclusion that the impact of magnetostriction on the lattice constant of sample 90127A lies on the order of $\Delta a^{\mathrm{pt}}(T_C) = (-1.6 \pm 0.6) \cdot 10^{-4}$ Å. It has to be noted, that this shift lies on the same order as the estimated errors and therefore, the experiments' resolution. The change in relative lattice constant of $\Delta a^{\mathrm{pt}}(T_C)/a = (-2.8 \pm 1.1) \cdot 10^{-5}$ is in good agreement with the determined magnetostriction constants on the order of 10^{-5} [Masmanidis05]. Compared to the thermal expansion of GaAs of approximately $1 \cdot 10^{-4}$

for $\Delta T = 10\,\mathrm{K}$ the effect of magnetostriction on the lattice structure is negligible. In the case of sample 61212A the temperature range below and in the vicinity of T_C needs to be investigated more carefully, making it impossible to draw conclusions at this point. In general, it is experimentally convenient to investigate samples with high magnetic transition temperatures, due to the accessibility of the temperature range below T_C.
The impact of thermal heating on the lattice constant of self-assembled InAs/GaAs QDs was also investigated using the developed XRD setup at BL9. The measurements revealed a difference in relative lattice constants $\Delta a/a_\mathrm{s}$ between a reference GaAs sample and the QD sample to lie on the order of $1 \cdot 10^{-5}$ for a temperature range of $\Delta T = 10\,\mathrm{K}$. Therefore, it is assumed, that the QDs do not influence the thermal lattice expansion of the sample. This conclusion yielded an estimation of the heating effect due to laser irradiation of 0.5 K, supporting a tetragonal lattice distortion of 6.4 fm per $\mathrm{W/cm^2}$ along the [001] direction of the QD sample. In conclusion, the polaron induced, tetragonal lattice distortion of optically excited (In,Ga)As/GaAs QDs has been measured directly for the first time.
Conclusively, an XRD setup was developed, that allows the investigation of optically or thermally induced structural changes in semiconductors on an order of $1 \cdot 10^{-4}$ Å. However, there is room for optimization of the experimental setup. In the following an outlook of possible upgrades and future sample systems is given.
The most potential for improvement of the experimental setup lies in the cooling process. For experiments utilizing liquid nitrogen as a cooling agent a new transfer tube was purchased. Since this tube cannot be operated with liquid helium, it does not need to be evacuated leading to much more mechanical flexibility. In order to use liquid helium as a refrigerant, a construction needs to be developed, that allows to raise the Dewar vessel in order to introduce the transfer tube into the Dewar vessel and Optistat simultaneously without colliding with the ceiling of the beamline hutch.
In order to confirm the results and interpretations found on sample 90127A it may be interesting to investigate another sample with T_C above 100 K in a future experiment. Additionally, it might be interesting to apply a magnetic field along another direction in order to increase the magnetization and therefore, maybe the impact of magnetostriction.
Another sample system that could be of interest is cadmium magnesium tellurium (CdMgTe) that can be used to increase the efficiency of large area solar modules [Kosyachenko14]. A formation of a telluride layer at the interface of CdMgTe layers and a gold grating, which was lithographed on top, due to optical illumination was observed in [Kreilkamp16]. The combination of semiconductor materials and plasmonic structures combine the excellent optical and electrical properties of semiconductors with the ability of plasmonic structures to increase the dynamical optical response of semiconductor nanostructures and therefore, reveal new processes that would be too weak to be observed otherwise. XRD and XRR experiments can reveal several information on the telluride layer like layer thickness, crystallinity or texture.

Bibliography

[Als-Nielsen11] Als-Nielsen, J. and McMorrow, D. Elements of Modern X-ray Physics, (John Wiley & Sons2011).

[Anderson50] Anderson, P. 'Antiferromagnetism. Theory of Superexchange Interaction.' *Phys. Rev.* **79**, 350–356 (1950).

[Andreev00] Andreev, A.V. and Lindbaum, A. 'Sponatneous magnetostriction of CeFe.' *J. Alloys Compd.* **297**, 43–45 (2000).

[ARS17] ARS. 'The DE 202G Closed Cylce Cryocooler from ARS' "`http://www.arscryo.com/DE-202.html`".' (2017).

[Bauer58] Bauer, E. 'Phänomenologische Theorie der Kristallabscheidung an Oberflächen. I.' *Zeitschrift für Kristallographie* **110**, 372–394 (1958).

[Benabbas99] Benabbas, T., Androussi, Y., and Lefebvre, A. 'A finite-element study of strain field in vertically aligned InAs islands in GaAs.' *J. Appl. Phys.* **86**, 1945–1950 (1999).

[Besombes01] Besombes, L., Kheng, K., Marsal, L., and Mariette, H. 'Acoustic phonon broadening mechanism in single quantum dot emission.' *Phys. Rev. B* **63**, 155.307 (2001).

[Blakemore82] Blakemore, J.S. 'Semiconducting and other Major Properties of Gallium-Arsenide.' *J. Appl. Phys.* **53**(10), R123–R181 (1982).

[Blinowski03] Blinowski, J. and Kacman, P. 'Spin interactions of interstitial Mn ions in ferromagnetic GaMnAs.' *Phys. Rev. B* **67**(12) (2003).

[Borri01] Borri, P., Langbein, W., Schneider, S., Woggon, U., Sellin, R.L., Ouyang, D., and Bimberg, D. 'Ultralong Dephasing Time in InGaAs Quantum Dots.' *Phys. Rev. Lett.* **87**, 157.401 (2001).

[Bowen98] Bowen, D.K. and Tanner, B.K. High Resolution X-Ray Diffractometry and Topogrphy, (Taylor & Francis: London1998).

[Bowen06] Bowen, D.K. and Tanner, B.K. X-Ray Metrology in Semiconductor Manufacturing, (CRC Press2006).

[Bragg13] Bragg, W.H. and Bragg, W.L. 'The Reflection of X-rays by Crystals.' *Proc. R. Soc. A* **88**, 428–438 (1913).

[Brown01] Brown, S.D., Bouchenoire, L., Bowyer, D., Kervin, J., Laundy, D., Longfield, M.J., Mannix, D., Paul, D.F., Stunault, A., Thompson, P., Cooper, M.J., Lucas, C.A., and Stirling, W.G. 'The XMaS beamline at ESRF: instrumental developments and high resolution diffraction studies.' *J. Synchrotron. Rad.* **8**, 1172–1181 (2001).

[Chen09] Chen, L., Yan, S., Xu, P.F., Lu, J., Wang, W.Z., Deng, J.J., Qian, X., Ji, Y., and Zhao, J.H. 'Low-temperature magnetotransport behaviors of heavily Mn-doped (Ga,Mn)As films with high ferromagnetic transition temperature.' *Appl. Phys. Lett.* **95**(18) (2009).

[Chikazumi64] Chikazumi, S. Physics of Magnetism, (John Wiley & Sons1964).

[Coey99] Coey, J.M.D., Viret, M., and Von Molnar, S. 'Mixed-valence manganites.' *Adv. Phys.* **48**, 167–293 (1999).

[Courts03] Courts, S.S. and Swinehart, P.R. 'Review of Cernox (Zirconium Oxy-Nitride) Thin Film Resistance Temperature Sensors.' *AIP Conf. Proc.* **684** (2003).

[CryoVac17] CryoVac. 'Konti-Cryostat-Mikro - Complete Guide '`http://www.cryovac.de/downloads/konti_mikro.pdf`'.' (2017).

[Daruka97] Daruka, I. and Barabasi, A.L. 'Dislocation-Free Isalnd Formation in Heteroepiatxial Growth: A Study at Equilibrium.' *Phys. Rev. Lett.* **79**, 3708–3711 (1997).

[Debye16] Debye, P. and Scherrer, P. 'Interferenzen an reglos orientierten Teilchen im Röntgenlicht.' *Nachrichten von der Gesellschaft der Wissenschaften zu Göttingen, Mathematisch-Physikalische Klasse* **1916**, 1–15 (1916).

[Dectris14] Dectris. 'Pilatus 100K Manual V. 1.8 "`https://www.dectris.com/technical_pilatus.html?file=tl_files/root/support/technical_notes/pilatus/Technical_Specification_PILATUS_100K-S_V1_8.pdf`".' (2014).

[Deppe00] Deppe, D.G. and Huffaker, D.L. 'Quantum dimensionality, entropy, and the modulation response of quantum dot lasers.' *Appl. Phys. Lett.* **77**, 3325–3327 (2000).

[Dietl00] Dietl, T., Ohno, H., Matsukura, F., Cibert, J., and Ferrand, D. 'Zener model description of ferromagnetism in zinc-blende magnetic semiconductors.' *Science* **287**(5455), 1019–1022 (2000).

[Dietl01] Dietl, T., Ohno, H., and Matsukura, F. 'Hole-mediated ferromagnetism in tetrahedrally coordinated semiconductors.' *Phys. Rev. B* **63**(19) (2001).

[Dietl02] Dietl, T. 'Ferromagnetic Semiconductors.' *Semicond. Sci. Technol.* **17**, 377–392 (2002).

[Dietl10] Dietl, T. 'A ten-year perspective on dilute magnetic semiconductors and oxides.' *Nat. Mater.* **9**(12), 965–974 (2010).

[Dirac26] Dirac, P.M. 'On the Theory of Quantum Mechanics.' *Proc. Roy. Soc.* **112A**, 661–677 (1926).

[Dzyaloshinsky58] Dzyaloshinsky, I. 'A Thermodynamic Theory of "Weak" Ferromagnetism of Antiferromagnetics.' *J. Phys. Chem. Solids* **4**, 241–255 (1958).

[Falta10] Falta, J. and Möller, T. Forschung mit Synchrotronstrahlung: Eine Einführung in die Grundlagen und Anwendungen, (Vieweg+ Teubner2010).

[Foner59] Foner, S. 'Versatile and Sensitive Vibrating-Sample-Magnometer.' *Rev. Sci. Instrum.* **30**, 548–557 (1959).

[Gallardo-Hernandez13] Gallardo-Hernandez, S., Martinez-Velis, I., Ramirez-Lopes, M., Kudriatsev, Y., Escobosa-Echavarria, A., Luiz Morelhao, S., and Lopez-Lopez, M. 'Self-assembly of compositionally modulated GaMnAs multilayers during molecular beam epitaxy.' *Appl. Phys. Lett.* **103**, 192.113 (2013).

[Glunk09] Glunk, M., Daeubler, J., Dreher, L., Schwaiger, S., Schoch, W., Sauer, R., Limmer, W., Brandlmaier, A., Goennenwein, S.T.B., Bihler, C., and Brandt, M.S. 'Magnetic anisotropy in (Ga,Mn)As: Influence of epitaxial strain and hole concentration.' *Phys. Rev. B* **79**(19), 195.206 (2009).

[Goldstein85] Goldstein, L., Glas, F., Marzin, J.Y., Charasse, M.N., and Le Roux, G. 'Growth by molecular beam epitaxy and characterization of InAs/GaAs strained-layer superlattices.' *Appl. Phys. Lett.* **47**, 1099–1101 (1985).

[Goodenough55] Goodenough, J.B. and Loeb, A.L. 'Theory of Ionic Ordering, Crystal Distortion, and Magnetic Exchange Due to Covalent Forces in Spinels.' *Phys. Rev.* **98**, 391–408 (1955).

[Graf02] Graf, T., Gjukic, M., Brandt, M.S., Stutzmann, M., and Ambacher, O. 'The Mn3+/2+ acceptor level in group III nitrides.' *Appl. Phys. Lett.* **81**, 5159–5161 (2002).

[Graf03] Graf, T., Goennenwein, S.T.B., and Brandt, M.S. 'Prospects for carrier-mediated ferromagnetism in GaN.' *phys. stat. sol. (b)* **239**, 277–290 (2003).

[Greilich09] Greilich, A., Economou, S.E., Spatzek, S., Yakovlev, D.R., Reuter, D., Wieck, A.D., Reinecke, T.L., and Bayer, M. 'Ultrafast optical rotations of electron spin in quantum dots.' *Nat. Phys.* **5**, 262–266 (2009).

[Grundmann95a] Grundmann, M., Christen, J., Ledentsov, N.N., Böhrer, J., Bimberg, D., Ruvimov, S.S., Werner, P., Richter, U., Gösele, U., Heydenreich, J., Ustinov, V.M., Egorov, A.Y., Zhukov, A.E., Ko'ev, P.S., and Alferov, Z.I. 'Ultranarrow Luminescence Lines from Single Quantum Dots.' *Phys. Rev. Lett.* **74**, 4043–4046 (1995).

[Grundmann95b] Grundmann, M., Stier, O., and Bimberg, D. 'InAs/GaAs pyramidal quantum dots: Strain distribution, optical phonon, and electronic structure.' *Phys. Rev. B* **52**, 11.969–11.981 (1995).

[Guffarth01] Guffarth, F., Heitz, R., Schliwa, A., Stier, O., Ledentsov, N.N., Kovsh, A.R., Ustinov, V.M., and Bimberg, D. 'Strain engineering of self-organized InAs quantum dots.' *Phys. Rev. B* **64**, 085.305 (2001).

[Heisenberg26] Heisenberg, W. 'Mehrkörperproblem und Resonanz in der Quantenmechanik.' *Z. Physik* **38**, 411–426 (1926).

[Henke93] Henke, B.L., Gullikson, E.M., and Davis, J.C. 'X-ray interactions: photoabsorption, scattering, transmission, and reflection at E=50-30000 eV, Z=1-92.' *At. Data Nucl. Data Tables* **54**, 181–342 (1993).

[Holy95] Holy, V., Darhuber, A.A., Bauer, G.G., Wang, P.D., Song, Y.P., Torres, C.M.S., and Holland, M.C. 'Elastic strains in GaAs/AlAs quantum dots studied by high-resolution x-ray diffraction.' *Phys. Rev. B* **52**(11), 8348–8357 (1995).

[Holy06] Holy, V., Matej, Z., Pacherova, O., Novak, V., Cukr, M., Olejnik, K., and Jungwirth, T. 'Mn incorporation in as-grown and annealed (Ga,Mn)As layers studied by x-ray diffraction and standing-wave fluoresence.' *Phys. Rev. B* **74**, 245.205 (2006).

[IOPScience02] IOPScience. 'Semiconductor Science and Technology, 17(4).' (2002).

[James98] James, R.D. and Wuttig, M. 'Magnetostriction of martensite.' *Philisophical Magazine A* **77**, 1273–1299 (1998).

[Joule47] Joule, J.P. 'XVII. On the effects of magnetism upon the dimensions of iron an steel bars.' *Philosophical Magazine Series 3* pp. 76–87 (1847).

[Jungwirth06] Jungwirth, T., Sinova, J., Masek, J., Kucera, J., and MacDonald, A.H. 'Theory of ferromagnetic (III,Mn)V semiconductors.' *Rev. Mod. Phys.* **78**(3), 809–864 (2006).

[Kanamori59] Kanamori, J. 'Superexchange Interaction and Symmetry Properties of Electron Orbitals.' *J. Phys. Chem. Solids* **10**, 87–98 (1959).

[Klokholm76] Klokholm, E. 'The Measurement of Magnetostriction in Ferromagnteic Thin-Films.' *IEEE Trans. Magn.* **12**(6), 819–821 (1976).

[Korotkov02] Korotkov, R.Y., Gregie, J.M., and Wessels, B.S. 'Optical properties of the deep Mn acceptor in GaN:Mn.' *Appl. Phys. Lett.* **80**, 1731–1733 (2002).

[Kosyachenko14] Kosyachenko, L.A., Mykytyuk, T.I., Fodchuk, I.M., Maslyanchuk, O.L., Martinez, O.S., Perez, E.R., and Mathew, X. 'Electrical characteristics of thin-film CdS/CdMgTe heterostructure for tandem solar cells.' *Solar Energy* **109**, 144–152 (2014).

[Kramers34] Kramers, H.A. 'L'Interaction entre les Atome Magnetogenes dans un Cristal Paramagnetique.' *Physica* **1**, 182–192 (1934).

[Kreilkamp16] Kreilkamp, L.E., Akimov, I.A., Belotelov, V.I., Glavin, B.A., Litvin, L., Rudzinski, A., Kahl, M., Jede, R., Wiater, M., Wojtowicz, T., Karczewski, G., Yakovlev, D.R., and Bayer, M. 'THz lattice vibrations for active plasmonics with light: Ultrafast optical response in gold/telluride hybrid plasmonic crystals.' *Phys. Rev. B* **93**, 125.404 (2016).

[Krstajic04] Krstajic, P.M., Peeters, F.M., Ivanov, V.A., Fleurov, V., and Kikoin, K. 'Double-exchange mechanism fo Mn-doped III-V ferromagnetic semiconductors.' *Phys. Rev. B* **70**, 195.215 (2004).

[Krywka06] Krywka, C., Paulus, M., Sternemann, C., Volmer, M., Remhof, A., Nowak, G., Nefedov, A., Pöter, B., Spiegel, M., and Tolan, M. 'The new diffractometer for surface X-ray diffraction at beamline BL9 of DELTA.' *J. Synchrotron. Rad.* **13**, 8–13 (2006).

[Kubena87] Kubena, R.L., Joyce, R.J., Ward, J.W., Garvin, H.L., Stratton, F.P., and Brault, R.G. 'Dot lithography for zero-dimensional quantum wells using focused ion beams.' *Appl. Phys. Lett.* **50**, 1589–1591 (1987).

[LakeShore09] LakeShore. 'User's Manual Model 340 Temperature Controller' "`http://www.lakeshore.com/ObsoleteAndResearchDocs/340_Manual.pdf`".' (2009).

[Lang05] Lang, R., Winter, A., Pascher, H., Krenn, H., Liu, X., and Furdyna, J.K. 'Polar kerr effect studies on GaMnAs epitaxial films.' *Phys. Rev. B* **72**, 024.430 (2005).

[Ledentsov98] Ledentsov, N.N., Ustinov, V.M., Shchukin, V.A., Kop'ev, P.S., Alferov, Z.I., and Bimberg, D. 'Quantum dot heterostructures: fabrication, properties, laser (Review).' *Semiconductors* **32**, 343–365 (1998).

[Leonard93] Leonard, D., Krishnamurthy, M., Reaves, C.M., Denbaars, S.P., and Petroff, P.M. 'Direct formation of quantum-sized dots from uniform coherent islands of InGaAs on GaAs surfaces.' *Appl. Phys. Lett.* **63**, 3203–3205 (1993).

[Leonard94] Leonard, D., Pond, K., and Petroff, P.M. 'Critical layer thickness for self-assembled InAs islands on GaAs.' *Phys. Rev. B* **50**, 11.687–11.692 (1994).

[Liu95] Liu, X., Prasad, A., Nishio, J., Weber, E.R., Liliental-Weber, Z., and Walukiewicz, W. 'Native point defects in low-temperature-grown GaAs.' *Appl. Phys. Lett.* **67**, 279–281 (1995).

[Liu03] Liu, X., Sasaki, Y., and Furdyna, J. 'Ferromagnetic resonance in GaMnAs: Effects of magnetic anisotropy.' *Phys. Rev. B* **67**(20) (2003).

[Liu06] Liu, X. and Furdyna, J.K. 'Ferromagnetic resonance in GaMnAs dilute magnetic semiconductors.' *J. Phys.: Condens. Matter* **18**, 245–279 (2006).

[Lundstrom99] Lundstrom, T., Schoenfeld, W., Lee, H., and Petroff, P.M. 'Exciton Storage in Semiconductor Self-Assembled Quantum Dots.' *Science* **286**, 2312–2314 (1999).

[Lèvy00] Lèvy, L.P. Magnetism and Superconductivity, (Springer2000).

[Maca02] Maca, F. and Masek, J. 'Electronic states in GaMnAs: Substitutional versus interstitail position of Mn.' *Phys. Rev. B* **65**, 235.209 (2002).

[MacDonald05] MacDonald, A.H., Schiffer, P., and Samarth, N. 'Ferromagnetic semiconductors: moving beyond (Ga,Mn)As.' *Nat. Mater.* **4**, 195–202 (2005).

[Maekawa06] Maekawa, S. Concepts in Spin Electronics, (OUP Oxford2006).

[Masek03] Masek, J., Kudrnovsky, J., and Maca, F. 'Lattice constant in diluted magnetic semiconductors (Ga,Mn)As.' *Phys. Rev. B* **67**(15) (2003).

[Masmanidis05] Masmanidis, S.C., Tang, H.X., Myers, E.B., Li, M., De Greve, K., Vermeulen, G., Van Roy, W., and Roukes, M.L. 'Nanomechanical measurement of magnetostriction and magnetic anisotropy in (Ga,Mn)As.' *Phys. Rev. Lett.* **95**(18), 187.206 (2005).

[Michler03] Michler, P. Single Quantum Dots - Fundamentals, Applications and New Concepts, (Springer-Verlag Berlin Heidelberg2003).

[Mollaev11] Mollaev, A.Y., Kamilov, I.K., Arslanov, R.K., Novotortsev, V.M., Marenkin, S.F., Trukhan, V.M., Arslanov, T.R., Zalibekov, U.Z., and Fedorchenko, I.V. 'High-Pressure Volume Magnteostriction in the Diluted Magnetic Semiconductor CdMnGeAs.' *Inorg. Mater.* **47**, 1171–1173 (2011).

[Moriya60] Moriya, I. 'Anisotropic Superexchange Interaction and Weak Ferromagnetism.' *Phys. Rev.* **120**, 91–98 (1960).

[Nazmul05] Nazmul, A.M., Amemiya, T., Shuto, Y., Sugahara, S., and Tanaka, M. 'High temperature ferromagnetism in GaAs-based heterostructures with Mn delta doping.' *Phys. Rev. Lett.* **95**(1), 017.201 (2005).

[Novikova61] Novikova, S.I. 'Investigation of Thermal Expansion of GaAs and ZnSe.' *Sov. Phys. Solid State* **3**(1), 129–130 (1961).

[Ohno96] Ohno, H., Shen, A., Matsukura, F., Oiwa, A., Endo, A., Katsumoto, S., and Iye, Y. '(Ga,Mn)As: A new diluted magnetic semiconductor based on GaAs.' *Appl. Phys. Lett.* **69**(3), 363–365 (1996).

[Ohno98] Ohno, H. 'Making Nonmagnetic Semiconductors Ferromagnetic.' *Science* **281**(5379), 951–956 (1998).

[Ohno99] Ohno, H. 'Properties of ferromagnetic III-V semiconductors.' *J. Magn. Magn. Mater.* **200**, 110–129 (1999).

[Oxford13a] Oxford. 'Operator's Handbook Oxford Instruments Omicron Nanoscience Optistat CF-V2.' (2013).

[Oxford13b] Oxford, I. 'Mercury Instrumentation - Intelligent control of cyrogenic and magnetic environments' "`https://www.oxford-instruments.com/OxfordInstruments/media/nanoscience/PDFs/Instrumentation/Mercury-Instrumentation-Product-Guide.pdf`".' (2013).

[Oxford13c] Oxford, I. 'The Optistat CF-2V from Oxford Instruments' "`https://www.oxford-instruments.com/products/cryogenic-environments/optical-cryostats-for-spectroscopy/liquid-helium-cryostats-(4k)/helium-cryostats-optistatcfv2`".' (2013).

[Oxford14] Oxford, C. '700 Series Cryostream Cooler - Operation & Instruction Guide 5.2' "`http://www.esrf.eu/files/live/users/providers/ldap/ac/cg/fh/thnguyen/files/Manuals/cryo_700_series_manual.pdf`".' (2014).

[Paul95] Paul, D.F., Cooper, M.J., and Stirling, W.G. 'Design of an x-ray beamline on a bending magnet at the ESRF for magnetic and high resolution diffraction.' *Rev. Sci. Instrum.* **66**, 1741–1744 (1995).

[Pietsch04] Pietsch, U., Holy, V., and Baumbach, T. High-Resolution X-Ray Scattering: From Thin Films to Lateral Nanostructures, (Springer: Berlin2004).

[Qi10] Qi, J., Yan, J.A., Park, H., Steigerwald, A., Xu, Y., Gilbert, S.N., Liu, X., Furdyna, J.K., Pantelides, S.T., and Tolk, N. 'Mechanical and electronic properties of ferromagnetic GaMnAs using ultrafast coherent acoustic phonons.' *Phys. Rev. B* **81**, 115.208 (2010).

[Reithmaier04] Reithmaier, J.P., Sek, G., Löffler, A., Hofmann, C., Kuhn, S., Reitzenstein, S., Kledysh, L.V., Kulakovskii, V.D., Reinecke, T.L., and Forchel, A. 'Strong coupling in a single quantum dot-semiconductor microcavity system.' *Nature* **432**, 197–200 (2004).

[Robinson86] Robinson, I.K. 'Crystal truncation rods and surface roughness.' *Phys. Rev. B* **33**(6), 3830–3836 (1986).

[Sadowski00] Sadowski, J., Domagala, J.Z., Bak-Misiuk, J., Kolesnik, S., Swiatek, K., Kanski, J., and Ilver, L. 'Structural properties of MBE grown GaMnAs layers.' *Thin Solid Films* **367**(1-2), 165–167 (2000). 3rd International Conference on Molecular Beam Epitaxy-Growth Physics and Technology (MBE-GPT 99), WARSAW, POLAND, MAY 23-28, 1999.

[Sadowski01] Sadowski, J., Mathieu, R., Svedlindh, P., Domagala, J.Z., Bak-Misiuk, J., Swiatek, K., Karlsteen, M., Kanski, J., Ilver, L., Asklund, H., and Sodervall, U. 'Structural and magnetic properties of GaMnAs layers with high Mn-content grown by migration-enhanced epitaxy on GaAs(100) substrates.' *Appl. Phys. Lett.* **78**(21), 3271–3273 (2001).

[Sawicki03] Sawicki, M., Matsukura, F., Dietl, T., Schott, G.M., Ruester, C., Schmidt, G., Molenkamp, L.W., and Karczewski, G. 'Temperature Peculiarities of Magnetic Anisotropy in GaMnAs: The Role of Hole Concentration.' *J. Supercond.* **16**, 7–10 (2003).

[Sawicki05] Sawicki, M., Wang, K.Y., Edmonds, K.W., Campion, R.P., Staddon, C.R., Farley, N.R.S., Foxon, C.T., Papis, E., Kaminska, E., Piotrowska, A., Dietl, T., and Gallagher, B.L. 'In-plane uniaxial anisotropy rotations in (Ga,Mn)As thin films.' *Phys. Rev. B* **71**(12) (2005).

[Schlipf13] Schlipf, M., Betzinger, M., Lezaic, M., Friedrich, C., and Blügel, S. 'Structural, electronic, and magnetic properties of the europium chalcogenides: A hybrid-functional DFT study.' *Phys. Rev. B* **88**, 094.433 (2013).

[Schott01] Schott, G.M., Faschinger, W., and Molenkamp, L.W. 'Lattice constant variation and complex formation in zincblende gallium manganese arsenide.' *Appl. Phys. Lett.* **79**, 1807–1809 (2001).

[Schott03] Schott, G.M., Schmidt, G., Karczewski, G., Molenkamp, L.W., Jakiela, R., Barcz, A., and Karczewski, G. 'Influence of growth conditions on the lattice constant and composition of GaMnAs.' *Appl. Phys. Lett.* **82**, 4678 (2003).

[Seeck12] Seeck, O.H., Deiter, C., Pflaum, K., Bertam, F., Beerlink, A., Franz, H., Horbach, J., Schulte-Schrepping, H., Murphy, B.M., Greve, M., and Magnusson, O. 'The high-resolution diffraction beamline P08 at Petra III.' *J. Synchrotron. Rad.* **19**, 30–38 (2012).

[Seravalli07] Seravalli, L., Minelli, M., Frigeri, P., and Franchi, S. 'Quantum dot strain engineering of InAs / InGaAs nanostructures.' *J. Appl. Phys.* **101**, 024.313 (2007).

[Sotomayor Torres94] Sotomayor Torres, C.M., Smart, A.P., Watt, M., Foad, M.A., Tsutsui, K., and Wilkinson, C.D.W. 'Nanometer Fabrication Techniques for Wide-Gap II-VI Semiconductors and Their Optical Characterization.' *J. Electron. Mater.* **23**, 289–298 (1994).

[Sparks67] Sparks, P.W. and A., S.C. 'Thermal Exapnsion from 2 to 40 K of Ge, Si, and Four III-V Compounds.' *Phys. Rev.* **163**, 779–790 (1967).

[Stangl04] Stangl, J., Holy, V., and Bauer, G. 'Structural properties of self-organized semiconductor nanostructures.' *Rev. Mod. Phys.* **76**, 725–783 (2004).

[Stiff-Roberts02] Stiff-Roberts, A.D., Chakrabarti, S., Pradhan, S., Kochman, B., and Bhattacharya, P. 'Raster-scan imaging with normal-incidence, mininfrared InAs/GaAs quantum dots infrared photodetectors.' *Appl. Phys. Lett.* **80**, 3265–3267 (2002).

[Tam88] Tam, A.C. and Schroeder, H. 'Precise measurements of a magnetostriction coefficient of a thin soft-magnetic film deposited on a substrate.' *J. Appl. Phys.* **64**(10, 2), 5422–5424 (1988).

[Tanaka05] Tanaka, M. 'Spintronics: recent progress and tomorrow's challanges.' *J. Cryst. Growth* **278**, 25–37 (2005).

[Tiemeyer12] Tiemeyer, S. 'Lattice expansion in optically excited InAs/GaAs quantum dots.' Ph.D. thesis, Technische Universität Dortmund (2012).

[Tiemeyer16] Tiemeyer, S., Bombeck, M., Göhring, H., Paulus, M., Sternemann, C., Nase, J., Wirkert, F., Möller, J., Büning, T., Seeck, O., Reuter, D., Wieck, A., Bayer, M., and Tolan, M. 'Polaron-induced lattice distortion of (In,Ga) As/GaAs quantum dots by optically excited carriers.' *Nanotechnology* **27**, 425.702 (2016).

[Tolan94] Tolan, M., Press, W., Brinkop, F., and Kotthaus, J.P. 'Xray diffraction from laterally structured surfaces: Crystal truncation rods.' *J. Appl. Phys.* **75**(12), 7761–7769 (1994).

[Tolan99] Tolan, M. X-Ray Scattering from Soft-Matter Thin Films: Materials Science and Basic Research, volume 148, (Springer-Verlag: Berlin1999).

[Vagov02] Vagov, A., Axt, V.M., and Kuhn, T. 'Electron-phonon dynamics in optically excited quantum dots: Exact solution for multiple ultrashort laser pulses.' *Phys. Rev. B* **66**(16) (2002).

[Vegard21] Vegard, L. 'Die Konstitution der Mischkristalle und die Raumfüllung der Atome.' *Zeitschrift für Physik* **5**, 17 (1921).

[Verzelen02] Verzelen, O., Ferreira, R., and Bastard, G. 'Exciton Polarons in Semiconductor Quantum Dots.' *Phys. Rev. Lett.* **88**, 146.803 (2002).

[vonMolnar91] von Molnar, S., Munekata, H., Ohno, H., and Chang, L.L. 'New diluted magnetic semiconductor based on III-V compounds.' *J. Magn. Magn. Mater.* **93**, 356–364 (1991).

[Wang93] Wang, J., Sagar, R.P., Schmider, H., and Smith Jr., V.H. 'X-Ray Elastic and Inelastic Scattering Factors for Neutral Atoms Z = 2-92.' *At. Data Nucl. Data Tables* **53**, 233–269 (1993).

[Wang04] Wang, K.Y.Y., Edmonds, K.W., Campion, R.P., Gallagher, B.L., Farley, N.R.S., Foxon, C.T., Sawicki, M., Boguslawski, P., and Dietl, T. 'Influence of the Mn interstitial on the magnetic and transport properties of GaMnAs.' *J. Appl. Phys.* **95**, 6512–6514 (2004).

[Warren90] Warren, B.E. X-Ray Diffraction, (Dover Publications Inc.1990).

[Welp03] Welp, U., Vlasko-Vlasov, V.K., Liu, X., Furdyna, J.K., and Wojtowicz, T. 'Magnetic Domain Structure and Magnetic Anisotropy in GaMnAs.' *Phys. Rev. Lett.* **90**, 167.206 (2003).

[Welp04] Welp, U., Vlasko-Vlasov, V.K., Menzel, A., You, H.D., Liu, X., Furdyna, J.K., and Wojtowicz, T. 'Uniaxial in-plane magnetic anisotropy of GaMnAs.' *Appl. Phys. Lett.* **85**(2), 260–262 (2004).

[Wie89] Wie, C.R., Chen, J.C., Kim, H.M., Liu, P.L., Choi, Y.W., and Hwang, M. 'X-ray interference measurement of ultrathin semiconductor layers.' *Appl. Phys. Lett.* **55**, 1774–1776 (1989).

[Wilson64] Wilson, R.H. and Kasper, J.S. 'The Crystal Structure of MnAs above 40 °C.' *Acta Crystallogr.* **17**, 95–101 (1964).

[Yu02] Yu, K.M., Walukiewicz, W., Wojtowicz, T., Kuryliszyn, I., Liu, X., Sasaki, Y., and Furdyna, J.K. 'Effect of the location of Mn sites in ferromagnetic GaMnAs on its Curie temperature.' *Phys. Rev. B* **65**, 201.303(R) (2002).

Acknowledgements

First, I would like to thank Prof. Dr. Metin Tolan and Prof. Dr. Manfred Bayer for enabling me to accomplish this thesis as well as Prof. Dr. Kevin Kröninger and Dr. Bärbel Siegmann for completing the examination board.
I am very grateful to Dr. Michael Paulus and Dr. Christian Sternemann for the excellent support throughout the entire time working on this thesis. You always found the right, motivating words for whatever setbacks occurred along the way. Thank you for lots of discussions and advice. Additionally, I would like to thank Dr. Thomas Büning, Susanne Dogan, and Simon Wulle for the relaxed and pleasant atmosphere in the office. From Gangsta Rap Monday to Death Metal Friday everything was possible. Furthermore, I am thankful to the whole chair E1a, who pushed me to my limits at extracurricular activities like soccer, bowling and our very own interpretation of "Piano Man". Here, I am especially thankful to Dr. Thomas Büning, Dr. Steffen Bieder, Karin Esch, Stefanie Roese, Mirko Elbers, Hendrik Rahmann, Julian Schulze, Dr. Paul Salmen, Simon Wulle, Jennifer Bolle, and everyone else I might have forgotten for their help during various beamtimes. On that note I acknowledge the support of the local contacts Dr. Michael Paulus and Dr. Christian Sternemann at DELTA and Dr. Didier Wermeille at ESRF and of course DELTA and the ESRF for providing synchrotron radiation desperately needed for the conducted experiments. Furthermore, I thank Susanne Kralemann and the mechanical workshop at the physics department in Dortmund for constructing various adapter plates together with Klaus Rudloff and the design office for realizing the ball bearing setup.
Thank you to Dr. Ilya Akimov, Dr. Lars Kreilkamp, and Dr. Alexey Scherbakov for the help with any questions regarding magnetism and related matters. The providing of the samples investigated in this thesis by the group of Prof. Dr. Jacek Furdyna is appreciated. Thanks to Dr. Ulf Wiedwald of the group of Prof. Dr. Michael Farle for measuring T_C of both samples on such short notice.
The financial support of the DFG and BMBF through SFB TRR 160 and 05K13PE1, respectively is gratefully acknowledged.
For proofreading this thesis I thank Dr. Christian Sternemann, Julia Färber and Keith, Nathalie Göhring, and Dr. Thomas Büning.
I want to thank Dr. Erik Schumacher, Dr. Thomas Büning, Jan Verwohlt and Simon Wulle. Without all of you there is no way I would have finished my studies. Thank you for lots of fun while working on the exercises for several lectures and the one or another beer. And for the DAP attestations, definitely the DAP attestations. Fortunately, my

programming skills evolved.
Last but not least I want to thank my parents and Hans Künne. Thank you for your unconditional support throughout my entire life. Special thanks to my wonderful wife Nathalie Göhring. Thank you for all the motivation and necessary pressure along the way and for taking my mind of work every now and then.